Colloids with perception-dependent motility: Dynamics and structure of rotating aggregates and directed swarms

INAUGURAL DISSERTATION

zur
Erlangung des Doktorgrades
der Mathematisch-Naturwissenschaftlichen Fakultät
der Universität zu Köln

vorgelegt von

Rodrigo Saavedra
aus Mexicali, Mexiko

Jülich 2023

Berichterstatter: Dr. habil. Marisol Ripoll
Prof. Dr. Johannes Berg

Tag der letzten mündlichen Prüfung: 10.11.2023

Contents

1 Introduction and theoretical concepts

1.1 Self-organization of active matter

To understand systems in thermodynamic equilibrium, a theoretical framework was successfully developed during the twentieth century, namely equilibrium statistical mechanics. This discipline provided principles explaining the properties of macroscopic systems, e.g. solid and liquid phases, in terms of their microscopic constituents, e.g. phonons, magnetic spins, and gas molecules [1, 2]. Nonetheless, systems out of thermodynamic equilibrium have still a large number of open questions [3–5]. *Active matter* refers to systems of agents in such non-equilibrium due to local consumption of energy, allowing agents to perform directed motion [6]. Systems of interacting active agents have been found to self-organize leading to spectacular collective behavior [7–10]. This has been observed at the macroscopic level in animals, e.g. in schools of fish [11], flocks of birds [12], herds of sheep [13], and swarms of insects [14]. Moreover, they are also observed at the microscopic level in living organisms like bacteria [15], active biopolymers [16], and spermatozoa [17]. The possibility to control systems of active agents has led to a growing interest in artificially engineered systems with activated constituents, e.g. light-activated colloidal suspensions [18–20], driven magnetic colloids [21–24], and swarms of micro-robots [25–30]. Some of the most common types of collective behavior include flocking, vortex formation, and turbulent flows. See Fig. 1.1. All in all, active matter is a multidisciplinary research field, and it lies in the intersection of physics, chemistry, and biology [33, 34].

Biological agents perform actions according to information processing of signals they exchange among each other or perceive from the environment. They can make decisions and adjust their behaviors in order to achieve a specific goal. For this, biological agents require of sensing mechanism, allowing interactions that go beyond pair physical forces exerted between the agents. For example, cells can

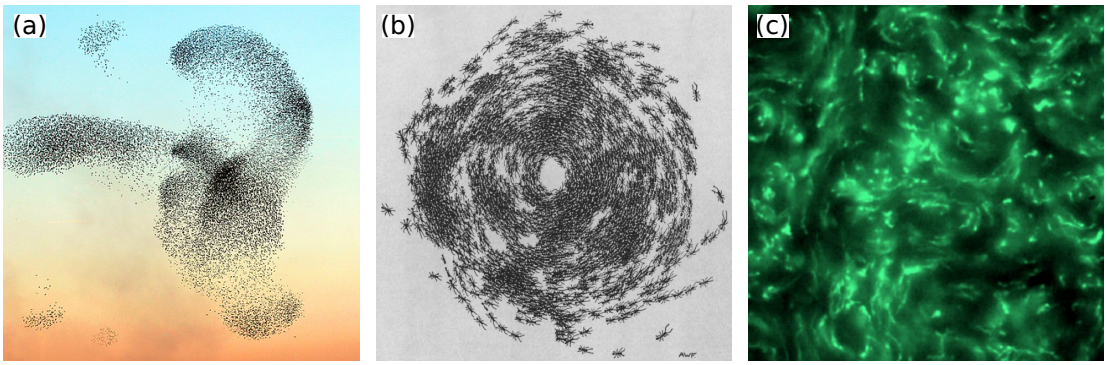

Figure 1.1: *Examples of collective behavior in active matter.* (a) Starling murmuration displaying flocking behavior. Taken from [31]. (b) Illustration of an ant "death spiral", an example of vortex formation. Taken from [32]. (c) Visualization of turbulent fluid flow in the suspension of swimming bacteria *Bacillus subtilis* by fluorescent tracer particles (false-color). Taken from [15].

regulate gene expressions based on input chemicals received from their surroundings, and animals can decide either to continue foraging or escape from threats based on auditive and visual stimuli. Such *biological information processing* has been found to play an essential role in the emergence of collective states, e.g. in herds of sheep [13], and schools of fish [35]. In recent years, an effort has been made to mimic systems of active agents that include internal degrees of freedom to account for a type of information processing, propagating signals from the individual parts to the collective whole [36, 37]. This has led to the development of *programmable active matter* [38], which aims to develop systems of active automatons with adaptable collective states. One task of this novel research subject is to design self-organization strategies of model systems with local sensing and actuation rules.

One interesting strategy is when an agent perceives the system's local density and switches its motility after a given density threshold is surpassed. This strategy has been termed *quorum sensing*, as it models the behavior observed in certain populations of bacteria like *Aliivibrio fischerei* [39], which are capable of sensing surrounding chemical concentration and fluoresce altogether after a chemical threshold is surpassed, as if they have reached some kind of quorum decision [40]. Systems with quorum sensing have been found to aggregate into a circular droplet, which can be either compact or dilute depending on the chemical threshold. This has been experimentally verified in externally controlled colloidal suspensions, where a narrow laser beam locally activates colloids according to a computer assisted feedback mechanism accounting for the local density perception [41]. See Fig. 1.2a-b. Another interesting type of perception, is when

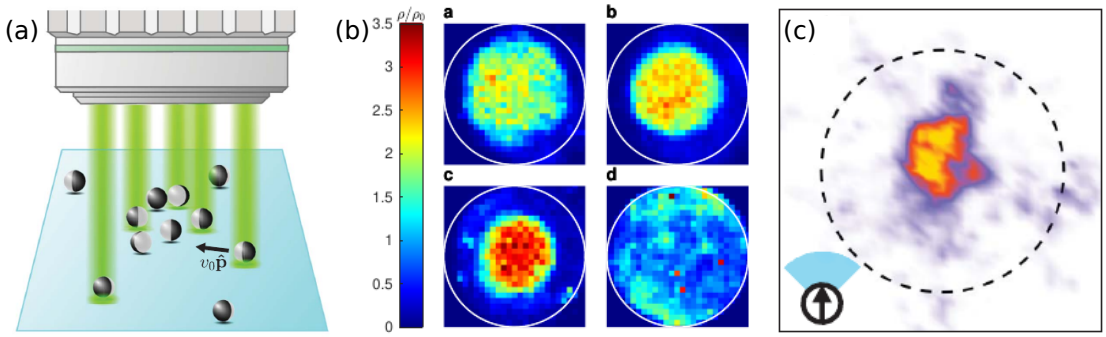

Figure 1.2: *Modes of perception in experiments of laser activated colloids.* (a) Illustration of an experimental setup of individually activated Janus colloids self-propelling with speed v_0 and direction $\hat{\boldsymbol{p}}$. Clustering formation in experiments mimicking (b) quorum sensing, and (c) visual perception. Panels in (b) correspond to systems with different chemical concentration threshold. Figures taken from Refs. [41, 45].

agents sense their environment within a restricted cone of vision. Visual perception differs fundamentally from quorum sensing where the perception of agents is isotropic. The reason is that here the interactions are non-reciprocal, i.e. a particle A might sense a particle B, however particle B might not sense particles A, in other words the action-reaction principle is broken. See Fig. 1.2b. This has been found to lead to a zoo of collective behaviors, which would not be possible if interactions were reciprocal. For example, active particles with visual perception aligning their orientation based on the position of other neighbouring particles, have shown to aggregate into clusters, polar filaments, and nematic bands [42, 43], as has been demonstrated in particle-based numerical simulations. In experiments, visual perception has been employed to generate vortical structures when imposing a local torque to light-activated colloids [44].

In this chapter we describe some of the most important state-of-the-art concepts in active matter and non-equilibrium statistical mechanics [1, 2, 46–48]. We start introducing Brownian motion, which govern the dynamics of micrometer-sized colloids studied throughout this thesis. Then we explain a few paradigmatic examples of collective behavior, including those that have been developed in recent years, accounting for different modes of perception in active agents. Finally, we show the coarse-graining procedure of the equations of motion for active particles via the Smoluchowski equation. This is a useful method, which we later employ to derive analytic expressions explaining the overall behavior we observe in our microscopic models. We finish the chapter giving an outline of this thesis.

1.2 Brownian dynamics

The random motion of a small particle immerse in a fluid is called *Brownian motion*. This phenomenon was first observed by Robert Brown in 1827 when he was investigating pollen grains under the microscope [49]. He concluded these random moving particles should be a type of “microscopic living particles". The problem on Brownian motion captured the attention of physicist in 1905, when Albert Einstein and Marian Smoluchowski gave a physical explanation to this phenomena. They associated the random motion of the particles to microscopic physical forces related to the temperature of the fluid [50, 51]. In 1908, their formulation of Brownian motion was verified by the experimental work of Jean Baptiste Perrin [52, 53]. On the same year, Paul Langevin described the microscopic dynamics of a single particle subject to collisions with the molecules of the fluid, by proposing an stochastic differential equation for the velocity of the particle [54].

1.2.1 Langevin equation

The Langevin equation describes the dynamics of a Brownian particle immersed in a surrounding medium, it contains the information of both frictional and fluctuating forces [48], namely

$$m\dot{\boldsymbol{v}} = -\zeta\boldsymbol{v} + \boldsymbol{\xi}, \tag{1.1}$$

where m is the particle's mass, $\boldsymbol{v}$ its velocity, and $\dot{\boldsymbol{v}}$ acceleration. The frictional force or *damping term* given by $-\zeta\boldsymbol{v}$ is directly proportional to the velocity $\boldsymbol{v}$ of the particle and to ζ the friction coefficient provided by the surrounding fluid. The fluctuating force or *noise term* given by $\boldsymbol{\xi}$ is an additional term accounting for the interactions with the surrounding medium or *heat bath*. Additional external forces exerted on the Brownian particle can be included as extra terms on the right hand side of the equation. For now we focus on the simple case without additional forces, extra terms accounting for intrinsic forces are described next in Sec. 1.2.3, and interaction forces in Sec. 1.3.

To fully characterize the motion of the particle, a more precise definition of the noise term is required. The most common interpretation of $\boldsymbol{\xi}$ is that it is a force coming from subsequent collisions between the particle under consideration and the molecules of the surrounding medium. As the collision forces are isotropic on the particle, we assume that the average noise term vanishes, therefore we take

$$\langle\boldsymbol{\xi}(t)\rangle = 0, \tag{1.2}$$

where $\langle\ldots\rangle$ is an average over time. Furthermore, the force magnitude is supposed to vary rapidly during an observation time, which is taken to be infinitesimally

small. Therefore the correlation between subsequent noise terms is given by

$$\langle \boldsymbol{\xi}(t)\boldsymbol{\xi}(t')\rangle = 2B\delta(t-t'), \tag{1.3}$$

where B is a measure of the fluctuating force strength. The delta term indicates that subsequent impacts are decorrelated from time t to time t', which is an infinitesimal interval of time. The probability distribution satisfying the moments of the noise term, Eq. (1.2) and Eq. (1.3), is a Gaussian probability distribution. For this reason, the noise term should be sampled from

$$\mathcal{P}[\boldsymbol{\xi}(t)] = \frac{1}{\sqrt{4\pi B}} \exp\left[-\int_0^t d\tau \frac{\boldsymbol{\xi}(\tau)^2}{4B}\right]. \tag{1.4}$$

Fluctuation-dissipation theorem

Integrating Eq. (1.1) over time and plugging Eq. (1.2) and Eq. (1.3) we obtain the solution for the velocity

$$v(t) = e^{-\zeta t/m} v(0) + \frac{1}{m}\int_0^t dt' e^{-\zeta(t-t')/m}\xi(t'), \tag{1.5}$$

where the first term is a damping of the initial velocity, and the second term comes from noise. Since $\xi(t)$ is not a smooth function, but rather an *stochastic* term, it is not possible to analytically solve the integral in this equation. However, one is interested in understanding averaged quantities. For example, the mean squared velocity can be obtained by taking the square of Eq. (1.5) and integrating over time, then to solve the integral over the noise we consider the correlation defined in Eq. (1.3). We obtain

$$\langle v(t)^2\rangle = e^{-2\zeta t/m} v(0)^2 + \frac{B}{\zeta m}(1 - e^{-2\zeta t/m}). \tag{1.6}$$

In the long time limit, the terms with exponentials vanish, and the mean squared velocity approaches the value

$$\lim_{t\to\infty} \langle v(t)^2\rangle = \frac{B}{\zeta m}, \tag{1.7}$$

i.e. stronger fluctuations or smaller friction coefficients lead to larger deviations of the velocity from the mean.

The most interesting result here, comes from connecting Eq. (1.7) with the energy equipartition theorem, which tell us that a particle immersed in a surrounding medium of temperature T has a kinetic energy proportional to $dk_BT/2$,

where k_B is the Boltzmann constant and d is the dimension of the system. In other words, each spatial degree of freedom adds an extra $k_BT/2$ to the total energy. Then, in two dimensions the theorem tell us that the mean squared velocity in equilibrium is

$$\lim_{t\to\infty}\langle v(t)^2\rangle = \frac{k_BT}{m} \tag{1.8}$$

Therefore, comparing Eq. (1.7) and Eq. (1.8) we find that the fluctuating force strength B and the thermal energy energy k_BT follow the relation

$$B = \zeta k_BT, \tag{1.9}$$

which is called *fluctuation-dissipation theorem* [55, 56]. The theorem expresses the balance between the frictional and fluctuating forces. While the friction tends to lead the system to rest, the random force keeps the system in motion. This balance occurs in thermal equilibrium at long times.

Mean squared displacement

Another important quantity to compute from the general solution of the Langevin equation Eq. (1.5) is the mean squared displacement (MSD) of a Brownian particle. In order to obtain the MSD, first we consider the particle displacement $\Delta\boldsymbol{r} \equiv \boldsymbol{r}(t) - \boldsymbol{r}(0)$, which we can obtain from the velocity as

$$\Delta\boldsymbol{r}(t) = \int_0^t dt'\boldsymbol{v}(t'). \tag{1.10}$$

Note that this equation averages to zero, i.e. a Brownian particle does not persistently displaces over time, but rather describes the trajectory of a random walk. Now we square Eq. (1.10), average over the noise and plug the noise average Eq. (1.3). We obtain the mean squared displacement

$$\langle\Delta r^2\rangle = 2\frac{k_BT}{\zeta}\left[t - \frac{m}{\zeta} + \frac{m}{\zeta}e^{-\zeta t/m}\right]. \tag{1.11}$$

At short times the constant and linear terms cancel out with the expansion of the exponential, and the MSD approximates to first order to

$$\lim_{t\to 0}\langle\Delta r^2\rangle \approx 2\frac{k_BT}{m}t^2. \tag{1.12}$$

At longer times, the exponential term vanishes, and the linear term dominates, leading to

$$\lim_{t\to\infty}\langle\Delta r^2\rangle \approx 2\frac{k_BT}{\zeta}t. \tag{1.13}$$

Einstein diffusion

Consider the one-dimensional diffusion equation for the local particle concentration (i.e. the number of particles within an infinitesimally small length $x + dx$) at time t,

$$\partial_t C(x,t) = D\partial_x^2 C(x,t). \tag{1.14}$$

Suppose that the test particle starts at $x = 0$. Then the concentration will change from an initial delta function in x to a spread-out Gaussian function of x. Due to symmetry, the mean displacement in this case is $\langle x \rangle = 0$. The mean squared displacement at time t is obtained by multiplying Eq. (1.14) by x^2 and integrating over x, one obtains

$$\partial_t \langle x^2 \rangle = 2D. \tag{1.15}$$

Integrating this equation over time, one arrives to the well-known Einstein formula for diffusion in one dimension

$$\langle x^2 \rangle = 2Dt. \tag{1.16}$$

This coefficient is a quantitative measure of molecular diffusion, it defines the length $l \sim \sqrt{Dt}$, which is the average distance a particle can travel during a time t.

We can rewrite the fluctuation-dissipation theorem Eq. (1.9) in terms of the diffusion coefficient,

$$D = \frac{k_B T}{\zeta}. \tag{1.17}$$

For a Brownian particle in a homogeneous and diluted three dimensional system, the diffusion coefficient can be obtained in terms of the temperature T, the viscosity of the fluid η, and the particle radius r,

$$D = \frac{k_B T}{6\pi\eta r}, \tag{1.18}$$

which is called the Stokes-Einstein equation [57].

1.2.2 Overdamped limit

The motion of an incompressible Newtonian fluid is governed by the Navier-Stokes equation [58]

$$\rho[\partial_t \boldsymbol{v} + (\boldsymbol{v} \cdot \nabla)\boldsymbol{v}] = -\nabla p + \mu \nabla^2 \boldsymbol{v} + \boldsymbol{f}, \tag{1.19}$$

where $\boldsymbol{v}$ is the fluid's velocity field, μ the dynamic viscosity, ρ density, p pressure, and $\boldsymbol{f}$ corresponds to external forces. The condition of incompressibility is given by $\nabla \cdot \boldsymbol{v} = 0$, which needs to be solved together with Eq. (1.19) to fully determine

the velocity field $\boldsymbol{v}$. The term on the left-hand side of the Navier-Stokes equation is a material derivative of the velocity field, defined as $d\boldsymbol{v}/dt \equiv \partial_t \boldsymbol{v} + (\boldsymbol{v} \cdot \nabla)\boldsymbol{v}$, describing the rate of change of flow field $\boldsymbol{v}$ for a material element (i.e. an infinitesimal volume of fluid) moving with velocity $\boldsymbol{v}$. The first term on the right-hand side accounts for the forces induced by pressure gradients, and the second term for diffusion of momentum. To non-dimensionalize the Navier-Stokes equation, we choose a characteristic length scale l and velocity u, from which the characteristic time scale follows $\tau = l/u$. Choosing the non-dimensional variables $\tilde{v} = v/u$, $\tilde{t} = t/\tau$, $\tilde{p} = \tau p/\mu$, $\tilde{f} = l^2 f/\mu u$ and $\tilde{\nabla} = l\nabla$, we obtain

$$\frac{\rho u l}{\mu} D_t \tilde{\boldsymbol{v}} = -\tilde{\nabla}\tilde{p} + \tilde{\nabla}^2 \tilde{v} + \tilde{\boldsymbol{f}}. \tag{1.20}$$

The prefactor in this equation defines the Reynolds number

$$\mathrm{R_e} = \frac{\rho u l}{\mu}. \tag{1.21}$$

The numerator $\rho u l$ is associated to inertial forces. When particles are suspended at high Reynolds number, $R_\mathrm{e} \gg 1$, the inertial forces acting on them are very large compared to the viscous forces. The resulting fluid flow in this limit tends to form eddy currents that lead to the formation of turbulent flows. In the opposite limit, when $R_\mathrm{e} \ll 1$, the left hand side of Eq. (1.20) vanishes, and the Navier-Stokes equation reduces to the Stokes equation, i.e. a diffusion equation for the fluid flow.

A colloid of length scale $l = 1\mathrm{nm}$ suspended in a fluid with relaxation time scale $\tau = 10^{-14}\mathrm{s}$, whereas the time scale of the colloidal motion is of $10^{-9}\mathrm{s}$. In this case the Reynolds number is also very small, and therefore the inertial forces acting on the colloid are negligible. In the context of the Langevin equation this is called the *overdamped limit*, which is effectively given by taking the left hand side of Eq. (1.1) to be zero, then it reduces to the overdamped Langevin equation

$$\dot{\boldsymbol{r}} = \frac{1}{\zeta}\boldsymbol{\xi}, \tag{1.22}$$

where $\dot{\boldsymbol{r}} = \boldsymbol{v}$. Note that in this limit time-reversibility holds, i.e. the system exhibits the same dynamics if $t \to -t$. For this reason, swimming at low Reynolds number requires of a specific mechanisms that is irreversible in time in order to achieve net displacement [59]. The *scallop theorem* states that a swimmer that performs reciprocal motion at low Reynolds number will only move back and forth, retracing its trajectory without net displacement [60].

1.2.3 Active Brownian particles

As we have shown above, a Brownian particle does not display directed motion. However, when the particle is driven by an active force $\boldsymbol{F}$, it can lead to a non-vanishing average displacement. Such driving force could be produced by the particle itself, in which case we say the colloid is able to *self-propel*. As opposed to driven active matter where an external force is applied to particles to induce motion, self-propelled particles require a mechanism that allow to locally produce gradients (e.g. of temperature, or chemical) that translate it into self-driven motion. As introduced in Sec. 1.1, the Janus particle is a colloidal sphere with two different sides, it is able to self-propel due to a local (temperature or chemical) gradient generated from different materials on each side that react with the surroundings. Then, the local gradient generates a flow field around the colloid, resulting in its overall finite displacement.

We define an *active Brownian particle* (ABP) as a particle which follows Eq. (1.22) and additionally has an internal degree of freedom accounting for the self-propulsion v_0, and orientation vector $\boldsymbol{e}$ which is simultaneously subject to a random torque $\boldsymbol{\eta}$ [61, 62]. Realistic examples of ABP's are spherically symmetric, e.g. disks in two dimensions and spheres in three dimensions. In those cases the particles undergo free rotational diffusion with diffusion constant D_R, even when no external torques are acting on them. The equations of motion governing the dynamics of an ABP are

$$\begin{aligned} \dot{\boldsymbol{r}} &= v_0 \boldsymbol{e} + \frac{1}{\zeta}\boldsymbol{\xi}, \\ \dot{\phi} &= \eta, \end{aligned} \tag{1.23}$$

where $\boldsymbol{e} = (\cos\phi, \sin\phi)^T$ with ϕ the self-propulsion orientation angle, see Fig. 1.3a; v_0 is a constant self-propulsion velocity. Similar to the translation degrees of freedom, here the rotational noise has zero mean $\langle \eta(t) \rangle = 0$ and is delta correlated $\langle \eta(t)\eta(t') \rangle = 2D_R\delta(t-t')$ with rotational diffusion coefficient

$$D_R = \frac{k_B T}{8\pi\eta r^3}. \tag{1.24}$$

Some examples of trajectories for various v_0 are shown in Fig. 1.3b-e. As v_0 increases, we obtain active trajectories that are characterized by directed motion at short time scales. However, over long time scales the orientation and direction of motion of the particle are randomized by its rotational diffusion.

To emphasize the difference between passive and active Brownian motion, it is instructive to consider the average particle trajectory given by the initial position and orientation fixed at time $t = 0$. In the case of passive Brownian motion, this

Figure 1.3: *Active Brownian particles in two dimensions.*(a) An ABP displacing in two dimensions with self-propulsion velocity v and orientation angle ϕ. The particle still undergoes Brownian motion in both position and orientation. The resulting $t = 10$s trajectories are shown for different velocities, (b) $v = 0$ (Brownian particle), (c) $v = 1\mu\mathrm{m\,s^{-1}}$, (d) $v = 2\mu\mathrm{m\,s^{-1}}$, and (e) $v = 3\mu\mathrm{m\,s^{-1}}$. With increasing values of v, the active particles move over longer distances before their direction of motion is randomized. Figure was taken from Ref. [8].

average vanishes by symmetry $\langle \Delta r \rangle = 0$, see Eq. (1.10). For an ABP instead, the average at short times is [8]

$$\langle \Delta r \rangle = \frac{v_0}{D_R} \left[1 - e^{-D_R t} \right]. \tag{1.25}$$

The rotational diffusion allows to define a quantity related with the *persistence length*, which is the average distance that a particle travels before changing its orientation, namely

$$l_p = \lim_{t \to \infty} \langle \Delta r \rangle = \frac{v_0}{D_R}. \tag{1.26}$$

The relative importance of directed motion versus diffusion for an ABP can be characterized by its Péclet number

$$P_e = \frac{v_0}{\sigma D_R}. \tag{1.27}$$

If P_e is small, diffusion is important, while if P_e is large, directed motion prevails.

We can also calculate the mean squared displacement of an ABP, giving [8]

$$\langle \Delta r^2 \rangle = \left[4D_T + 2\frac{v_0^2}{D_R} \right] t + 2\frac{v_0^2}{D_R^2} \left[e^{-D_R t} - 1 \right] \tag{1.28}$$

It has a ballistic regime at short times

$$\lim_{t/\tau_R \to 0} \langle \Delta r^2 \rangle = 4D_T t + v_0^2 t^2, \tag{1.29}$$

and a diffusive regime at longer times

$$\lim_{t/\tau_R \to \infty} \langle \Delta r^2 \rangle = 4(D_T + \frac{1}{2} v_0^2 \tau_R) t \equiv 4 D_{\text{eff}} t, \tag{1.30}$$

which shows that ABPs display an effective diffusion with coefficient $D_{\text{eff}} > D_T$ larger than the passive case.

1.3 Modelling collective behavior

When several active particles are moving together, interactions play an important role. The aim of this section is to provide insight into the interplay between activity and particle interactions, and how this interplay can lead to emergent collective behavior. The examples presented are paradigmatic models of systems with very simple interaction rules, where the systems self-organize into unexpected ordered structures. The simplicity of these models allows to understand in detail the collective behavior observed in systems at various length scales, from microscopic bacteria and colloidal suspensions, to macroscopic flocks of birds and schools of fish. A system exhibiting collective motion is made of units that are rather similar, moving with a nearly constant absolute velocity and are capable of changing their direction. Furthermore, they interact within a specific interaction range, e.g. by changing their direction of motion. The systems considered follow overdamped Langevin dynamics, and are subject to delta correlated noise with a given magnitude.

1.3.1 Motility-induced phase separation

We include short range steric interactions on the right hand side of Eq. (1.23), where the force $\boldsymbol{F}_i = -\nabla_i U(\{\boldsymbol{r}_i\})$ is obtained from a pair interaction potential

$$U(\{\boldsymbol{r}_i\}) = \sum_{j \neq i} u(|\boldsymbol{r}_j - \boldsymbol{r}_i|). \tag{1.31}$$

Volume exclusion can be modeled by different potential forces. The study of this effects on the emergent macroscopic phenomena dates back to the work by van der Waals [63], where short range interactions were considered to have both an attractive and a repulsive part, like the Lennard-Jones potential, resulting in liquid-vapor phase separation of the system [64].

In colloidal systems of Janus particles, no attractive interactions are involved, but only soft or hard-core *steric* repulsions are present. Such steric repulsions together with activity leads to the emergence of the so-called motility induced

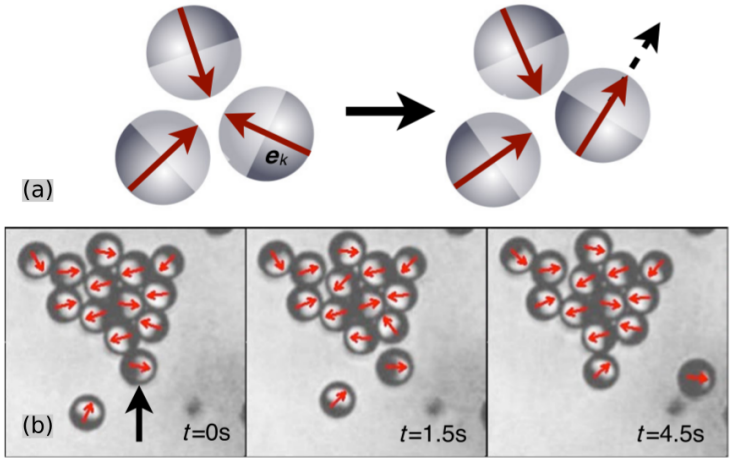

Figure 1.4: *Self-trapping mechanism.* (a) Sketch of the self-trapping mechanism: for colloidal particles to become free, they have to wait for their orientations to change due to rotational diffusion and point outwards. (b) Clustering process. The snapshots show how the indicated particle towards the bottom (left) leaves the cluster (center) and is replaced by another particle (right). Figure taken from Ref. [66].

phase separation (MIPS). This phenomena has been heavily studied in the field of active matter, as it is a generic behavior occurring for particles with activity and volume exclusion [65–79]. Here ABPs serve as one particular example where the system undergoes phase separation at intermediary packing fractions and sufficiently large propulsion strengths. At first, phase separation in this case might sound counter-intuitive, as there are no attractive interactions between particles that could drive aggregation and lead the system to phase separate in a similar way as a gas-liquid phase separation. However, the self-propulsion of the particles acting together with the steric forces result in a mechanism of *self-trapping*. Here, the active motion of the particles is directed on time scales of the rotational diffusion $\tau_R = 1/D_R$. If two particles collide head on, they block each other due to the volume exclusion. While this time is typically very short for the collision of only two particles, the situation is different for three of them, as shown in Fig. 1.4a. These particles can only move freely again when their orientation has changed sufficiently via rotational diffusion. As these collisional time scales are rather long compared to τ_R, other particles can in the meantime reach the building cluster and thus further obstruct the motion of the already trapped particles. This feedback-loop mechanism will lead to more and more particles to aggregate in the cluster, see Fig. 1.4b, such that a fluctuation of density will lead to the local density to further increase. In fact the effective speed of the particles

in this case is $v(\rho)$, depending on whether particles are in a crowded region or not [68, 80].

MIPS is strikingly similar to the vapor-liquid spinodal decomposition observed in many equilibrium systems [81, 82]. Thus, MIPS is a generic feature of systems that are driven out of equilibrium by a persistent local energy input that breaks detailed balance. Interestingly, hydrodynamic interactions between active colloids have been shown to have major effects on their rotational dynamics, and the local field inducing the particle's propelling forces (pushers versus pullers) plays a central role in MIPS [83, 84], e.g. either enhancing or diminishing clustering.

1.3.2 Vicsek model

The notion of flocking is used as a synonym of any kind of coherent motion of individual units [85, 86]. Coherent or ordered motion is assumed to be a counterpart of disordered, random motion. In the various models of flocking it emerges through a transition (from disorder to order) as a function of the relevant parameters of the models. Such type of transition was described for the first time by Tamás Vicsek in 1995 [87] in a system of particles with velocity alignment. Other flocking models were first proposed to mimic the behavior in schools of fish, then in 1986 Craig Reynolds proposed the Boids model [88]. The Vicsek model is also very similar to the Kuramoto model for synchronized oscillators [89–92], or the XY model for the 2D Ising paramagnet [93]. However, the difference here is that the particles are not fixed in space but rather they are free to move.

The Vicsek model is given by the equations

$$\begin{aligned} \dot{\boldsymbol{r}} &= v_0 \boldsymbol{e}, \\ \dot{\phi} &= \langle \phi \rangle_{r_{\mathrm{cut}}} + \eta, \end{aligned} \tag{1.32}$$

where the average $\langle \cdot \rangle_{r_{\mathrm{cut}}}$ represents the average direction of neighbouring particles of i, which are located within a cutoff range r_{cut}. Here η is a random number chosen with a uniform probability from the interval $(-\xi/2, \xi/2)$. There are three parameters for a given system size: the noise η, number density $\rho = N/L^2$, and velocity magnitude v_0. By varying these parameters, one can observe the transition between a gas-like motion, small moving groups, correlated random motion, and coherent collective motion, see Fig. 1.5. This model exhibits a non-equilibrium phase transitions leading to long-range order at sufficiently low noise and high particle density.

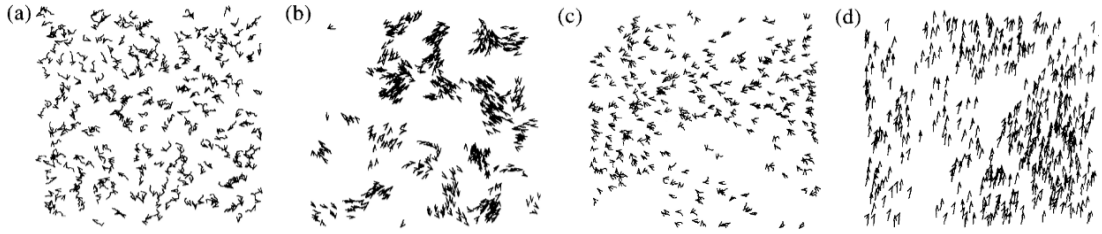

Figure 1.5: *Flocking transition.* Velocities of the particles are displayed for varying values of the density and noise. The actual velocity of a particle is indicated by a small arrow, while their trajectory for the last 20 time steps is shown by a short continuous curve. The number of particles is $N = 300$ in each case. (a) $L = 7$, $\eta = 2$. (b) For small densities and noise the particles tend to form groups moving coherently in random directions, here $L = 25$, $\eta = 0.1$. (c) After some time at higher densities and noise, $L = 7$ and $\eta = 2$, the particles move randomly with some correlation. (d) For higher density and small noise, $L = 5$ and $\eta = 0.2$, the motion becomes ordered. Figure taken from Ref. [7].

1.3.3 Quorum sensing

Coordinated motion in biological systems is often a consequence of complex communication pathways among their individual units. Some bacterial colonies produce extracellular enzymes called auto-inducers, which regulate their gene expression and act as a means of communication among cells. For instance, *Aliivibrio fischeri* produces luminescence after their local population surpasses a threshold density [94]. The communication among the bacterial cells triggered by the variation in local population density is called *quorum-sensing* [95–97]. This mechanism plays a vital role in the regulation of various physiological processes like manoeuvring local population density, regulation of gene expression, communication among cells, and motility.

For active particles, density-dependent velocity has been modeled as a discontinuous motility rule depending on the chemical concentration produced by the particles [40, 41, 98–101]. The model equations are

$$\begin{aligned} \dot{\boldsymbol{r}} &= v(c)\boldsymbol{e} + \boldsymbol{\xi}, \\ \dot{\phi} &= \eta, \end{aligned} \tag{1.33}$$

where the chemical concentration c is

$$c(\boldsymbol{r}) = \frac{\gamma}{4\pi D_c} \int d^2\boldsymbol{r}' \rho(\boldsymbol{r} - \boldsymbol{r}') \frac{e^{-r'/\lambda}}{r'}, \tag{1.34}$$

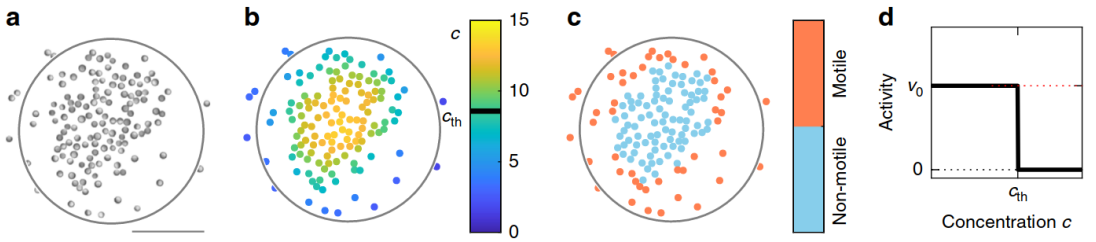

Figure 1.6: *Collective behavior of active particles with Quorum sensing.* (a) Snapshot of a two-dimensional suspension of carbon-coated particles with size $\sigma = 4.4\mu m$. Upon laser illumination, particles self-propel as a result of a local demixing process in the binary solvent. (b) The colour code corresponds to the chemical concentration c which is attributed to each particle. (c) Corresponding particle activity obtained by the concentration-dependent motility rule. (d) Concentration-dependent particle motility with self-propulsion velocity v_0 below the threshold c_{th} and Brownian diffusion above. Figure taken from Ref. [41].

which follows from the solution of the reaction-diffusion equation considering the chemical concentration relaxation time is instantaneous [102]. This has been found to lead to an phase separation of loose passive aggregates surrounded by a diluted active gas, which unlike MIPS is still possible at low particle density, see Fig. 1.6. Such behavior has been confirmed both by particle-based numerical simulations [99], as well as in experiments of light-activated colloids [41].

1.4 Mean-field theory

Langevin equations allow to directly obtain expectation values, for example for the velocity Eq. (1.6) and displacement Eq. (1.11), which can be analytically obtained even when activity is included, see Eq. (1.28). However, when interactions are taken into account, expectation values become much more difficult to obtain, and in general the model becomes difficult to be analytically studied. A better approach in this case, is to consider the probability density ψ of the system of particles. Then, the differential equation accounting for the dynamics of this distribution function is the Smoluchowski equation [47, 103], defined as

$$\partial_t \psi(\boldsymbol{X}, t) = \left[-\nabla D_{\mathrm{drift}}(\boldsymbol{X}, t) + \nabla^2 D_{\mathrm{diff}}(\boldsymbol{X}, t)\right] \psi(\boldsymbol{X}, t), \tag{1.35}$$

where $\psi = \psi(\boldsymbol{X}, t)$ is the joint probability distribution of finding the system in a state $\boldsymbol{X}$ at time t, and the coefficients D_{drift} and D_{diff} are the drift and diffusion terms, respectively. Note that the state $\boldsymbol{X}$ can consist of an arbitrary

number of degrees of freedom. For example, for a system of N particles where each particle i has position $\boldsymbol{r}_i$ and velocity $\boldsymbol{v}_i$, the state vector would include $\boldsymbol{X} = (\boldsymbol{r}_1, \dots \boldsymbol{r}_N; \boldsymbol{v}_1 \dots \boldsymbol{v}_N)$. In the following we identify the drift and diffusion terms for a system of active Brownian particles in Sec. 1.4.1, then we take the moment expansion in order to identify formulas for the continuum number density and polarization, Sec. 1.4.2.

1.4.1 Smoluchowski equation

Here we show the general coarse-graining procedure to go from a set of n differential equations describing the time-evolution of system variables defined by a vector $\boldsymbol{X}$, to a single differential equation describing the time-evolution of a probability distribution ψ. We consider Itô stochastic differential equations [47] defined by

$$d\boldsymbol{X}(t) = \boldsymbol{A}(\boldsymbol{X}, t)dt + \boldsymbol{B}(\boldsymbol{X}, t)d\boldsymbol{W}(t), \tag{1.36}$$

where $\boldsymbol{A}$ is a drift term, $\boldsymbol{B}$ a diffusion term, and $\boldsymbol{W}$ a random Wiener process. Then, the corresponding Fokker-Planck equation is given by

$$\partial_t \psi(\boldsymbol{X}, t) = -\sum_{i=1}^{n} \partial_i \Big\{ A_i(\boldsymbol{X}, t)\psi \Big\} + \frac{1}{2} \sum_{j=1}^{n} \sum_{i=1}^{n} \partial_i \partial_j \Big\{ \Big[\boldsymbol{B}(\boldsymbol{X}, t) \cdot \boldsymbol{B}(\boldsymbol{X}, t) \Big]_{ij} \psi \Big\} \tag{1.37}$$

Here, the main quantity of interest is the one-body probability distribution, which is obtained from integrating the join probability distribution over the other $(N-1)$ degrees of freedom

$$\psi_1(\boldsymbol{X}_1, t) = N \int d\boldsymbol{X}_2 \dots d\boldsymbol{X}_N \psi(\{\boldsymbol{X}\}, t), \tag{1.38}$$

where $\psi_1(\boldsymbol{X}_1, t)d\boldsymbol{X}_1$ is the probability to find one particle inside the phase space volume $d\boldsymbol{X}_1$. In order to obtain the Fokker-Planck equation for Eq. (1.38), we should integrate Eq. (1.37) over the degrees of freedom $(\boldsymbol{X}_2, \dots, \boldsymbol{X}_N)$. In more physical terms, the one-body state vector $\boldsymbol{X}_1$ corresponds to generalized coordinate and conjugate momenta of a given particle $\boldsymbol{X}_1 = (\boldsymbol{q}_1, \boldsymbol{p}_1)$. For the system of active Brownian particles described by Eq. (1.23), it corresponds to the Cartesian coordinates and the orientation vector of a given ABP, i.e. $\boldsymbol{X}_1 = (\boldsymbol{r}_1, \boldsymbol{e}_1)$.

The N-body Smoluchowski equation for a system of ABPs is given by

$$\partial_t \psi = \sum_{k=1}^{N} \{ -\nabla_i \cdot [(v_0 \boldsymbol{e}_i - \frac{D}{k_B T} \boldsymbol{F}_i)\psi] + D_T \nabla_i^2 \psi + D_R \partial_\phi^2 \psi \}. \tag{1.39}$$

Integrating over $N-1$ degrees of freedom this reduces to the 1-body equation

$$\partial_t \psi_1 = -\nabla \cdot [(\frac{D_T}{k_B T} \boldsymbol{F} + v_0 \boldsymbol{e} - D_T \nabla)\psi_1] + D_R \partial_\phi^2 \psi_1, \tag{1.40}$$

where

$$\boldsymbol{F}(\boldsymbol{r},\phi,t) = \int d\boldsymbol{r}'[-\nabla u(|\boldsymbol{r}'-\boldsymbol{r}|)]\rho(\boldsymbol{r}',t)g(\boldsymbol{r},\boldsymbol{r}',\phi,t), \tag{1.41}$$

with $g(\boldsymbol{r},\boldsymbol{r}',\phi,t)$ a pair correlation function; the product $\rho(\boldsymbol{r}',t)g(\boldsymbol{r},\boldsymbol{r}',\phi,t)$ is the conditional probability density to find a particle at position $\boldsymbol{r}'$ given that there is another particle at $\boldsymbol{r}$ with orientation ϕ at time t.

1.4.2 Moment expansion

Since $\psi_1(\boldsymbol{r},\phi,t)$ is a periodic function in ϕ, it can be expanded into a Fourier series

$$\psi_1(\boldsymbol{r},\phi,t) = \frac{1}{2\pi}\hat{\psi}_0 + \frac{1}{\pi}\sum_{n=1}^{\infty}\hat{\psi}_n(\boldsymbol{r},t)\cos(n\phi) + \frac{1}{\pi}\sum_{m=1}^{\infty}\hat{\varphi}_m(\boldsymbol{r},t)\sin(m,\phi), \tag{1.42}$$

where the Fourier coefficients or *moments* of expansion are

$$\hat{\psi}_0(\boldsymbol{r},t) = \int_0^{2\pi} d\phi\psi_1(\boldsymbol{r},\phi,t), \tag{1.43a}$$

$$\hat{\psi}_n(\boldsymbol{r},t) = \int_0^{2\pi} d\phi\psi_1(\boldsymbol{r},\phi,t)\cos(n\phi), \tag{1.43b}$$

$$\hat{\varphi}_m(\boldsymbol{r},t) = \int_0^{2\pi} d\phi\psi_1(\boldsymbol{r},\phi,t)\sin(m\phi). \tag{1.43c}$$

The moments can be identified as familiar physical quantities. The local density is simply given by

$$\rho(\boldsymbol{r},t) \equiv \hat{\psi}_0(\boldsymbol{r},t). \tag{1.44}$$

The polarization vector components can be identified as $p_x(\boldsymbol{r},t) \equiv \hat{\psi}_1(\boldsymbol{r},t)$ and $p_y(\boldsymbol{r},t) \equiv \hat{\varphi}_1(\boldsymbol{r},t)$, or in vectorial form

$$\boldsymbol{p}(\boldsymbol{r},t) = \int_{-\pi}^{\pi} d\phi\boldsymbol{e}(\boldsymbol{r},\phi,t)\psi_1(\boldsymbol{r},\phi,t). \tag{1.45}$$

The nematic tensor components are $Q_{xx} = -Q_{yy} = \hat{\psi}_2/2$ and $Q_{xy} = Q_{xy} = \hat{\varphi}_2$, or in tensor form

$$\boldsymbol{Q}(\boldsymbol{r},t) = \int_0^{2\pi} d\phi(\boldsymbol{e}\otimes\boldsymbol{e} - \frac{1}{2}\mathbb{1})\psi_1(\boldsymbol{r},\phi,t). \tag{1.46}$$

Higher order moments of expansion are associated to higher order vector multipoles similar to those in electrodynamics [104]. In order to obtain dynamic equations for the continuum quantities Eq. (1.44), (1.45), (1.46), moments should be taken over the 1-body Smoluchowski equation Eq. (1.40). With this procedure, the dynamic equation for a given moment shows to depend on other higher order

moments, leading to an infinite hierarchy of coupled differential equations. In order to truncate the hierarchy one needs to give a closure relation. In systems of active Brownian particles it is reasonable to close the equations to first order, as this type of active matter is polar and does not display nematic order, as can be the case in, e.g. for self-propelled repulsive disks [80, 105, 106].

1.5 Abstract of this thesis

In this thesis we focus on two-dimensional systems of colloids governed by Brownian dynamics that are able to sense their neighbors via a visual-type of perception, then they can switch their motility between passive and active depending on a given perception parameter. Our setup corresponds to experiments performed in Bechinger's lab in Konstanz University, where they have considered cases of quorum-sensing (isotropic perception) [41, 44] and visual-type of perception (anisotropic perception) [45, 107]. Here we study the case when the perception is both anisotropic and also *misaligned* with respect to the self-propulsion orientation vector. The purpose of this thesis is to characterize the emergence of collective behaviors in this model, as well as the dynamics and structural changes of the system. We provide novel strategies where the interplay between perception and motility of the agents allows them to self-organize into rotating aggregates and directed swarms. Our study sheds light in the understanding of active automatons with adaptable collective states, and can be implemented for example in macroscopic swarms of robots, or microscopic colloids activated by light.

In Ch. 2 we introduce the ingredients necessary to perform particle-based numerical simulations, like the integration method, interaction forces, boundary conditions, and optimization techniques. We also briefly comment on the organization and design of the Brownian dynamics code we developed to obtain results shown in this thesis.

In Ch. 3, we consider systems of colloids with discontinuous motility and *misaligned* visual perception. We explain how this type of interaction generically leads to aggregation and rotation of cohesive structures. Then, we characterize the resulting dynamics for different system parameters. In Ch. 4 we characterize different types of circular structures that emerge in this model, as a function of the perception threshold and misalignment angle. We also derive analytical expressions from conservation equations corresponding to a solid-body rotation of a continuum aggregate driven by activity at the interface. We find an agreement between theory and numerical results for the density, size, and angular velocity of the aggregates as a function of the system parameters.

In Ch. 5 we consider a binary mixture of particles with different misalign-

ment angle. Under given conditions, we find the striking case where the system aggregates, self-sorts into species subdomains which counter-rotate leading to a self-propulsion of the overall system. We characterize this process by means of dynamic parameters and their averages in steady state. We find cases where the directed swarms can either dilute or remain robust, or where the aggregate is species homogeneous and its center of mass describes random motion. We also study the swarms shape and how it can change for varying misalignment angle. In Ch. 6 we study cases when the mixture is non-equimolar. In this case the system self-organizes into swarms describing helical trajectories. We also show an example of an externally guided system, where we dynamically change the misalignment angle of the particles, leading to a swarm performing run-and-turn motion. We conclude the thesis with a summary and outlook.

2 Simulation methods

Computer simulations have already largely shown to be a powerful tool to study physical phenomena, from the microscopic details of a system to the macroscopic properties of experimental interest. It can be difficult (if not impossible) to carry out experiments under extreme conditions for the temperature and pressure, while a computer simulation of the material in, say a high-temperature plasma or the core of the earth, would be perfectly feasible. Furthermore, while the precise monitoring of the speed of molecular events is itself an experimental difficulty, it is straightforward to record in computer simulations. Performing efficient large-scale particle-based numerical simulations can be a technically laborious task. This difficulty has led to a combined effort of the community of computer scientist to build powerful collaborative software, which can be later employed with ease by other scientist in more specialized research areas. In the context of particle-based numerical simulations, some the largest collaborative projects that are still active are the Large-scale Atomic/Molecular Massively Parallel Simulator (LAMMPS) [108, 109], and GROMACS [1] [110]. While these can be powerful tools that require minimum understanding of the underlying algorithms and programming design of the code, they still demand a good knowledge of the physics behind different modules, in order to correctly implement them in a physically reasonable numerical simulation.

In this chapter we want to review the main ingredients of a Brownian dynamics simulation code. In Sec. 2.1 we review an integration method employed to solve the equations of motion of active Brownian particles. In Sec. 2.2 we show in detail the force term we employ to account for soft- or hard-core steric repulsions preventing particle overlap. In Sec. 2.3 we present the standard method to account for periodic boundary conditions. In Sec. 2.4 we introduce neighbour lists, i.e. useful data structures to avoid unnecessary calculations thus significantly enhancing simulation performance. Finally, in Sec. 2.5 we comment on the software developed to obtain numerical data in this thesis, as well as other software we employed for the data analysis.

[1] Its name originally derived from GROningen MAchine for Chemical Simulations, although currently GROMACS is not an abbreviation for anything, as little active development has taken place in Groningen in recent decades.

2.1 Numerical integration

Numerical integration comprises a broad family of algorithms that calculate the numerical value of a definite integral. In other words, they help to find numerical solutions of differential equations. For example, a Brownian dynamics (BD) simulation for a system of N interacting particles consists of solving the Langevin equations of motion (1.1) iteratively [111, 112]. There are well known integration algorithms that prescribe how to evolve the equations of motion of deterministic molecular dynamics (MD). Some of the most commonly employed methods are the Euler method, velocity Verlet, and the Runge-Kutta method [112]. However for Brownian dynamics one has to take into account a noise term coming from thermal fluctuations, which is not considered in the formal derivation of the deterministic numerical integration methods. Itô calculus has provided a useful mathematical framework to develop algorithms that solve stochastic differential equations (SDE) [113, 114]. The method we employ throughout this thesis is the Euler-Maruyama method, which is an extension of the Euler method for ordinary differential equations that also includes a noise term as found in stochastic differential equations [115]. This is an approximate method of solution of an SDE, which should include an advective and a diffusive term, see Eq. (1.36).

To obtain the Euler-Maruyama method corresponding to active Brownian particles, we identify the convective and diffusion terms in the equation of motion for an ABP, see Eq. (1.23). We include those terms in the Itô version of the equation of the form given by Eq. (1.36). Moreover, here we also include a conservative force term $\boldsymbol{F}_i = -\nabla_i U$ from an arbitrary potential U. Here we are interested in including volume exclusion, thus we consider the force term from an steric repulsion pair potential, as defined in Eq. (1.31). In this case, we obtain that each particle i follows the SDE

$$\begin{aligned} d\boldsymbol{r}_i &= \left[v_0 \boldsymbol{e}_i - \frac{D_T}{k_B T}\nabla_i U\right]\Delta t + \sqrt{2D_T \Delta t}\boldsymbol{W}_i^T, \\ d\phi_i &= \sqrt{2D_R \Delta t} W_i^R \end{aligned} \tag{2.1}$$

where v_0 is the self-propulsion velocity magnitude, $\boldsymbol{e}_i = (\cos\phi_i, \sin\phi_i)^T$ is the self-propulsion orientation vector; $\boldsymbol{W}_i^T$ and W_i^R are translational and rotational Wiener processes, i.e. random numbers sampled from a Gaussian distribution, with zero mean and unit variance; D_T and D_R are translational and rotational diffusion coefficients, respectively. Then, the corresponding Euler-Maruyama in-

tegration scheme is given by

$$\begin{aligned} \boldsymbol{r}_i(t+\Delta t) &= \boldsymbol{r}_i(t) + v_0 \boldsymbol{e}_i \Delta t - \frac{D_T}{k_B T}\nabla_i U + \sqrt{2D_T \Delta t}\boldsymbol{W}_T(t), \\ \theta_i(t+\Delta t) &= \theta_i(t) + \sqrt{2D_R \Delta t} W_R(t), \end{aligned} \tag{2.2}$$

The numerical precision of the algorithm is given by the time step Δt, which can be chosen to be as small as possible to achieve an arbitrary degree of precision. However, choosing too small Δt might also slow down the simulation, as the evolver will require too many time steps to finish the simulation until a desired final time t_f. For this reason, it is necessary to choose an intermediate value that allows to finish the simulation in a reasonable amount of time, while keeping good numerical precision.

In computer simulations, it is common to express quantities in reduced units. This simplifies equations significantly, and also allows to choose a unit system where most quantities have near-unit values, which are better handled by most computer architectures. For example, in Brownian dynamics simulations that model microscopic sized colloids, measuring length scales in meters could lead to numbers smaller than 10^{-9}, which are not easy to handle by computer due to numerical precision rounding errors. Choosing a unit system avoids this and also facilitates comparisons with experiment results presented in different units. We choose the unit of length to be the particle diameter $l = \sigma$, and the unit of time to be the translational diffusion timescale σ^2/D_T. In order to non-dimensionalize Eq. (2.2) we replace the terms $\tilde{\boldsymbol{r}} = \boldsymbol{r}/\sigma$, $\tilde{t} = D_T t/\sigma^2$, $\Delta\tilde{t} = D_T \Delta t/\sigma^2$, $\tilde{\nabla} = \nabla/\sigma$, and $\tilde{U} = U/k_B T$. We obtain

$$\begin{aligned} \tilde{\boldsymbol{r}}_i(\tilde{t}+\Delta\tilde{t}) &= \tilde{\boldsymbol{r}}_i(\tilde{t}) + \mathrm{P_e}\boldsymbol{e}_i\Delta\tilde{t} - \tilde{\nabla}_i U \Delta\tilde{t} + \sqrt{2\Delta t}\boldsymbol{W}_i^T, \\ \theta_i(\tilde{t}+\Delta\tilde{t}) &= \theta(\tilde{t}) + \sqrt{2\mathcal{D}\Delta\tilde{t}} W_i^R, \end{aligned} \tag{2.3}$$

where $\mathrm{P_e} = \sigma v_0/D_T$ is the translational Péclet number, and $\mathcal{D} = D_R\sigma^2/D_T$ is the ratio between rotational and translational diffusion timescales. In order to fully specify the dynamics, we still need to give the form of U in this equation. We can choose the form of this function, depending on the strength of excluded volume we desire to have, either with an attractive part or purely repulsive.

2.2 Volume exclusion

Volume exclusion forces prevent particles from overlapping in numerical simulations, i.e. they account for the actual physical size of the particles. Such forces

need to be included in order to model physical systems where short-range interactions are present. They are especially important in very dense systems (high packing fraction) when particles jam in a crystal-like structure, which is a prevalent effect in active matter [116–121]. In those cases particles are mostly static except in sites where disclinations and topological defects propagate [121–124]. To account for volume exclusion in Brownian dynamics, depending on the desired model, one should choose a pair interaction potential, which typically depends on parameters for the particle diameter σ, and an interaction energy ϵ.

Intermolecular interactions in nature are extremely complex. An N-body problem consists in understanding the interplay of interactions between N bodies at once that simultaneously influence one another. In molecular dynamics considering N-body interactions is computationally impossible, as we want to simulate systems with a large number of interacting particles. To solve this, we approximate N-body interactions to 2-body interactions, better known as *pair interactions*. The approximation consist in describing the non-bonded potential interactions by splitting the potential into a superposition of k-body terms, with k the number of particles involved in the interaction

$$U(\{\boldsymbol{r}\}) = \sum_{i=1}^{N} u(\boldsymbol{r}_i) + \frac{1}{2}\sum_{i=1}^{N}\sum_{j\neq i}^{N} u(|\boldsymbol{r}_i - \boldsymbol{r}_j|) + \mathcal{O}(3). \tag{2.4}$$

Here the first term corresponds to externally applied potential fields, which only depends of the position of a single particle i. The second term describes particle interactions given by the pair potential $u(|\boldsymbol{r}_i - \boldsymbol{r}_j|)$, which depends on the inter-particle distance $r_{ij} = |\boldsymbol{r}_i - \boldsymbol{r}_j|$.

Pair interaction potentials can consist of two or more contributions, given for example by a repulsive or attractive term, which typically are an inverse function of the inter-particle distance. The most general short-range pair potential is given by the Mie potential [125] defined as

$$u(r) = \frac{n}{n-m}\left(\frac{n}{m}\right)^{\frac{n}{n-m}} \epsilon\left[\left(\frac{\sigma}{r}\right)^{n} - \left(\frac{\sigma}{r}\right)^{m}\right], \tag{2.5}$$

where r is the inter-particle distance, n, m are positive integers, σ is the size of the particle, and ϵ is the depth of the potential well, which corresponds to the interaction strength. This potential is often called simply $n-m$ potential. The most extensively studied potential in literature is perhaps the Lennard-Jones potential, it is considered an archetype model for simple yet realistic intermolecular interactions, and has been extensively used to simulate phase transitions in liquids [126, 127]. The Lennard-Jones potential corresponds to Eq. (2.5) with

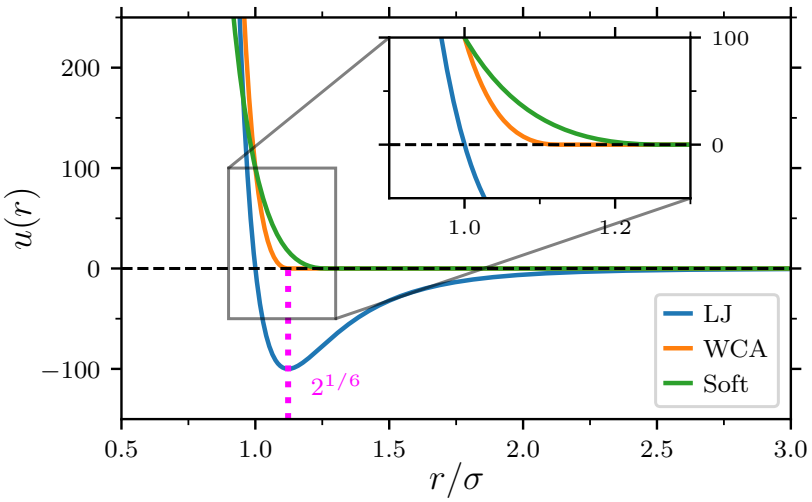

Figure 2.1: *Short-range interaction potentials.* Comparison between potentials: Lennard-Jones (LJ), hard-core repulsive Weeks-Chanlder-Anderson (WCA), and soft-core repulsion. Repulsive potentials are always positive, whereas LJ has a negative minimum at $r = 2^{1/6}\sigma$ corresponding to medium-range attractions.

$m = 12$ and $n = 6$,

$$u^{\mathrm{LJ}}(r) = 4\epsilon\left[\left(\frac{\sigma}{r}\right)^{12} - \left(\frac{\sigma}{r}\right)^{6}\right]. \tag{2.6}$$

This potential has a minimum at $r_{\min} = 2^{1/6}\sigma$, where $u(r_{\min}) = -\epsilon$, see Fig. 2.1. Negative values of u shown at intermediate radial distances correspond to attractions.

To model micrometer sized colloids, short-range repulsions need to be taken into account. We discard attractions by shifting the Lennard-Jones potential and truncate up to a cutoff radius of $r = 2^{1/6}\sigma$. This gives the repulsive Weeks-Chandler-Anderson potential [128] defined as

$$u^{\mathrm{WCA}} = \begin{cases} 4\epsilon\left[\left(\frac{\sigma}{r}\right)^{12} - \left(\frac{\sigma}{r}\right)^{6} + \frac{1}{4}\right] & r < 2^{1/6}\sigma \\ 0 & r > 2^{1/6}\sigma \end{cases}, \tag{2.7}$$

which is often taken with $\epsilon = 100k_BT$ in order to account for hard-core repulsions [65, 76, 99]. Since for the WCA potential the amount of possible particle overlap varies depending on the choice of ϵ, therefore neither σ nor the cutoff distance $2^{1/6}\sigma$ can be a reliable measure for the diameter. Nevertheless, an effective

diameter can be determined through a mapping of a soft-core potential (which allows the particle overlap) on hard disks via the Barker-Henderson diameter [129]. For the WCA potential, it can be calculated as

$$d_{\mathrm{BH}} = \int_0^{r_{\mathrm{cut}}} dr \left[1 - \exp\left(-\frac{u(r)}{k_B T}\right)\right], \tag{2.8}$$

giving $d_{\mathrm{BH}} \approx 1.10688\sigma$ for $\epsilon = 100 k_B T$. Self-propelled particles with higher speeds can, in principle, lead to larger particle overlaps. However, due to the strong repulsiveness of the WCA potential with $\epsilon = 100 k_B T$, we neglect corrections to d_{BH} arising from this.

Sometimes a much smaller interaction energy is chosen, for example $\epsilon = k_B T$ [79]. In those cases, a higher self-propulsion of the ABPs would distort the particle diameter drastically. To make comparisons varying v_0, it is therefore more convenient to stick with a higher value of $\epsilon = 100 k_B T$. In case a softer potential is still desired, then one can consider a 6-3 potential instead [130, 131], for example

$$u^{\mathrm{Soft}} = \begin{cases} 4\epsilon\left[\left(\frac{\sigma}{r}\right)^6 - \left(\frac{\sigma}{r}\right)^3 + \frac{1}{4}\right] & r < 2^{1/3}\sigma \\ 0 & r > 2^{1/3}\sigma \end{cases}, \tag{2.9}$$

which has a larger cutoff radius $r_{\mathrm{cut}} = 2^{1/3}\sigma$, and the effective Barker-Henderson diameter is $d_{\mathrm{BH}} \approx 0.22524\sigma$. A comparison between soft- and hard-core potentials is shown in Fig. 2.1.

2.3 Boundary conditions

In Brownian dynamics simulations boundary conditions are given in order to keep the system confined. In some cases boundary conditions are somewhat unimportant, for example if we are interested in the properties of a small droplet with cohesive forces between particles sufficient to hold the system together during the course of the simulation. We will study this type of situation in Ch. 3 and Ch. 4. Boundaries can be defined by an external wall potential, so particles can be confined, e.g. within a circular wall, within a box, or within a channel. However, if one is interested in studying only bulk properties, where effects due to wall interactions are not desirable, then it is useful to consider periodic boundary conditions (PBC). For example, to study finite-size transitions, it is necessary to include PBC to observe how the system percolates [132, 133]. Furthermore, PBC are also relevant in scenarios where the particles are able to self-propel

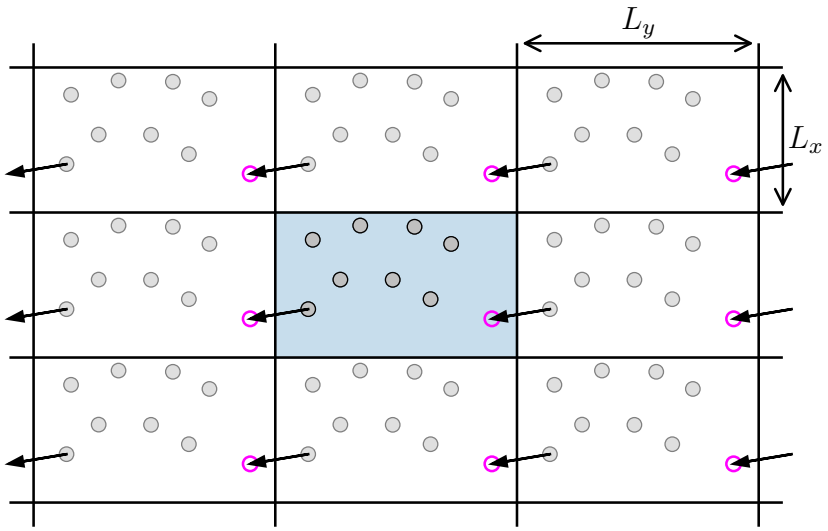

Figure 2.2: *Periodic boundary conditions.* A two-dimensional periodic system. Particles can enter and leave each box across each of the four edges.

with a large persistence length comparable to the box size, for example for a self-propelled droplet like we study in Ch. 5 and Ch. 6.

Periodic boundary conditions are implemented by considering a square box which is replicated throughout space to form an infinite lattice, see Fig. 2.2. It is sometimes useful to picture the basic simulation box as being rolled up to form the surface of a three-dimensional torus, where there is no need to consider an infinite number of replicas of the system, nor any image particles. For PBC, in the course of the simulation, the particles move in the original box, and their periodic image in each of the neighbouring boxes move in exactly the same way. Thus, as a particle leaves the central box, one of its images will enter through the opposite side. There are no walls at the boundary of the central and image boxes. The box simply forms a convenient frame of reference for measuring the positions of the N particles. Note that only for the particles in the central box need to be considered. When a particles leaves the box by crossing a boundary, attention is then switched to the image just entering. Therefore, the position of a particle i given in Cartesian coordinates $\boldsymbol{r}_i = (x_i, y_i)$ should be shifted when it leaves the box. For example, for the x coordinate

$$x_i(t+\Delta t) = \begin{cases} x_i(t+\Delta t) + L_x & \text{if} \quad x_i(t) < -L_x/2 \\ x_i(t+\Delta t) - L_x & \text{if} \quad x_i(t) > L_x/2 \end{cases}, \tag{2.10}$$

and similarly for the y coordinate. In principle, a particle in the central box

interacts with all particles from all boxes, which would be infinitely many contributions. However, for short ranged pair interactions (i.e. shorter than the box length), a particle i in the central box can only interact with the single closest realization of a particle j (either real or image). This is the so called minimum image convention, and in simulations it is typically applied for calculating inter-particle distances necessary to calculate pair interactions.

2.4 Neighbour lists

In Brownian dynamics simulations, we iterate over all particles at a given time step. On each iteration, the equations of motion of each particle i are solved [112, 134]. To calculate interaction forces acting on a particle i, we require to perform a second (nested) iteration over particles j, in order to calculate, for example, interparticle distances necessary to compute the interaction potential $U(\{\boldsymbol{r}_{ij}\})$. If the inter-particle separation is greater than the potential cutoff $r_{ij} > r_{\text{cut}}$, the program skips the expensive calculation of $U(\{\boldsymbol{r}\})$, as in that case that term is equally zero. In this procedure, the time to examine all particle pairs is proportional to N^2. Optimization methods allow us to integrate the equations of motion faster than that, by avoiding unnecessary calculations of vanishing terms. One simple yet useful tool is to maintain a list of nearest-neighbours of particle i. Such list is updated at regular intervals, but preferably after several iterations of the time loop. Between updates of the neighbour list, the program does not iterate through all j particles only to calculate the interactions with i, instead it iterates only over neighbours in the list. Therefore, the number of iterations over particle pairs is significantly reduced, saving computation time in computing minimum images, calculating r_{ij}, and checking against the cutoff radius. However, there is no change in the computation time spent calculating forces that arise from neighbours within the potential cutoff, i.e. neighbors satisfying $r_{ij} < r_{\text{cut}}$.

The most widely employed and easier method to implement a neighbour list is the so-called *Verlet list* [135, 136]. Here, the list includes all neighbours within a cutoff radius of the interaction force around a particle i. Furthermore, the list also include particles within a surrounding "skin", giving a larger disk of radius r_l, as shown in Fig. 2.3a. At the first step in a simulation, the list is constructed for all the neighbours of each particle, for which the pair separation is within r_l. Over the next few time steps, the list is used to evaluate interactions, discarding all other particles not in the list. After some time steps, the displacement of the particles is too large to ensure that all neighbours are properly accounted for, such that the neighbour list is reconstructed, and the procedure is repeated. The algorithm is successful when the layer around r_c is chosen to be thick enough

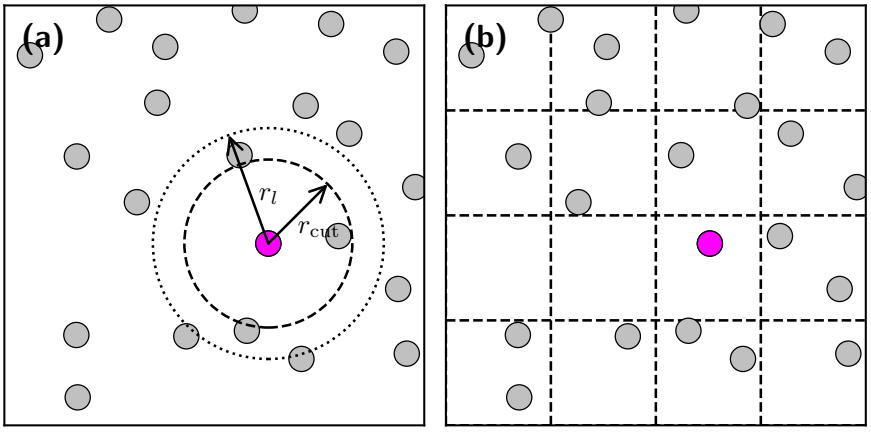

Figure 2.3: *Neighbour lists.* (a) Verlet list. (b) Cell list.

so that between reconstructions a particle j which is not on the list of i, cannot penetrate through the skin into the more important region below the cutoff radius r_{cut}. The particles in the skin can move in and out of the Verlet disk, but since they are on the list of particle i they are always considered regardless, until the list is next updated. The cutoff radius r_l is a parameter we are free to choose. As r_l is increased, the frequency of updates of the neighbour list will decrease. However, for a list too large, the efficiency of the non-update steps will decrease. Therefore, r_l should be finely tuned to find the optimal that minimizes the simulation time.

An alternative method for keeping track of neighbours in larger systems is the *cell-linked list* method [137]. The simulation box of size L is subdivided into smaller square cells of size l larger than the cutoff distance of the forces $r_{\text{cut}} < l < L$, see Fig. 2.3b. To construct linked lists, the first step is to sort all particles into their corresponding cells according to their positions. This is a rapid process since it scales with N, and is performed at every simulation time step. Two arrays are created during the sorting, the "head" and the "list" array. The head array is of the same size as the number of cells, thus contains a single element corresponding to one of the particles within each cell. The list array contains the index of the next particle in that cell and (in general) in the 8 neighbouring cells, see Fig. 2.3b. Then, a chain of particle indices is followed, starting from the head array, then iterating over the corresponding list array, which links particles until a zeroth element is reached corresponding to the end of the chain, i.e. there are no more particles to consider in the cell. The algorithm repeats for the next element in the head array, i.e. searching over neighbours in the next cell.

2.5 Software employed

To perform particle based numerical simulations, we developed a C++ code from scratch. We employed an object-oriented programming design of the code that allowed us to modularize subroutines, thus easing the development and extensibility of the code, see Fig. 2.4. Here, each particle is represented by an object of a template class with variables according to the particle's intrinsic properties like the position, self-propulsion, and perception. There is also a system class including a list of particles with each element being a particle object. The system class also includes definitions for the boundary conditions and the neighbour lists. Then, a system object serves as input for the evolver class, which sequentially computes the perception, forces, torques, and also performs integration subroutines. The evolver then updates the system after a simulation time step, and the process repeats for a desired number of simulation steps.

To ease the use of our simulation code, we employed some useful external libraries. The Boost++ library with `program_options` feature was included to provide an interface to read variables from command line and configuration files [138]. Most of the computing intensive simulations were performed in the JURECA dc partition provided by Forschungszentrum Jüelich [139]. To ease the compilation of our code in different computing architectures, we included a CMake configuration file, which autodetects the required compiler and libraries of the code [140]. In order to increase the simulation speed of our program, we included OpenMP

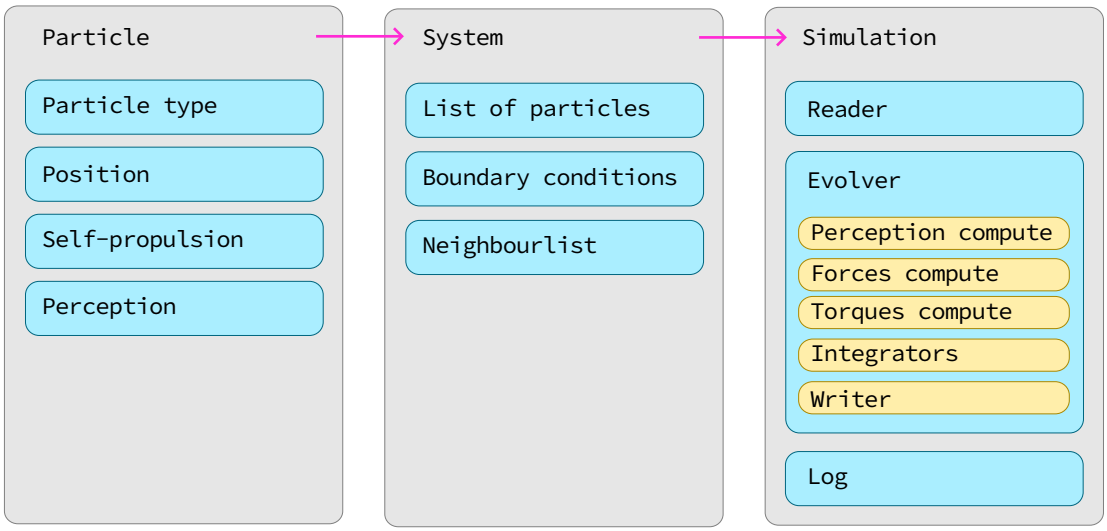

Figure 2.4: *Modules showing the object-oriented programming design of the Brownian dynamics simulation code.*

multithreading in several subroutines looping over particles [141]. This allowed us to make use of the full computing power of the dc partition nodes. We performed a large number of simulations to explore large regions of the phase space of the systems of interest. Finally, for the data analysis we developed several scripts in Python [142], which heavily relied on libraries like Ovito [143] and Numpy [144]. Figures were generated using Matplotlib [145].

Part I

Rotating aggregates induced by misaligned visual perception

3 Aggregate's cohesion and rotation mechanism

Adaptive behavior is an essential feature of biological systems. It refers to the capacity of agents to respond to stimulus sensed from their surroundings and adjust their actions accordingly. In many cases, adaptive processes require activity of the agents, e.g. in bacteria to navigate towards specific chemicals, or in animals to escape from dangerous predators. In systems of Janus colloids, an adaptive-type of mechanism has been recently implemented in experiments. This has been done by employing an external feedback loop where the colloid's positions are determined by particle tracking. Then, an externally controlled narrow laser beam switches the motility of the individual colloids depending on e.g. isotropic sensing of surrounding chemical concentration [41], or sensing of neighbouring particles within a restricted cone of vision [43–45, 107, 146]. These mechanisms successfully shown to achieve phase separation, and cohesion of colloidal aggregates.

Inspired on this type of systems, here we also consider particles with a visual-type of perception but in our case is misaligned with respect to the self-propulsion direction. We find that a discontinuous self-propulsion motility rule depending on the perception, is sufficient to induce formation of rotating cohesive aggregates. To study this, we perform particle-based numerical simulations and obtain perception radial profiles, showing that particles within the aggregate display orientation-dependent motility exerting an effective attractive force and a net torque on the system. Furthermore, we study the system dependence on the initial configuration of the system, which is adjusted to achieve metastable but robust crystal aggregates with an homogeneous activity distribution. Finally, we measure dynamical properties of the aggregates characterizing the size and rotational order of the system. We find the range of parameters for which the system reaches steady state during a characteristic collapse timescale. The mechanism studied here is generic and simplifies previous methods for which an additional aligning torque is required [42], demanding more control in experiments of light-activated colloids [44, 107]. Therefore, our model is expected to serve as a minimal strategy to be implemented in systems at different scales, including artificially engineered colloidal suspensions, and macroscopic swarms of robots.

3.1 Model

In this section we introduce the employed model, as well as the simulation parameters used, which corresponds to values similar to those employed in experiments of light-activated colloids [44, 45, 107]. Then, we describe how the system of particles self-organize from an homogeneously distributed diluted configuration into a rotating cohesive aggregate. Finally, we explain the mechanism of collapse and rotation by means of perception radial profiles, showing misaligned visual perception of the particles translate to orientation-dependent motility.

We consider a system of N particles, each particle i with position $\boldsymbol{r}_i$, self-propulsion speed v_i depending on the particle perception P_i, and orientation $\boldsymbol{e}_i \equiv (\cos\phi_i, \sin\phi_i)^T$, where ϕ_i is the angle enclosed between $\boldsymbol{e}_i$ and the x-axis, as illustrated in Fig. 3.1a. The dynamics of each particle i is governed by overdamped Langevin equations

$$\dot{\boldsymbol{r}}_i = v_i(P_i)\boldsymbol{e}_i - \nabla_i U + \sqrt{2D_t}\boldsymbol{\xi}_i, \tag{3.1a}$$

$$\dot{\phi}_i = \sqrt{2D_r}\eta_i, \tag{3.1b}$$

where, $\boldsymbol{\xi}_i$ and η_i correspond to translational and orientational zero-mean and delta correlated white noise; D_t and D_r to translational and rotational diffusion coefficients, respectively. The interaction potential U corresponds to short-range steric interactions, here given by the Weeks-Chandler-Anderson potential. This type of interactions prevent particles to overlap at short distances. Here we employ a potential strength of $\epsilon = 100k_BT$ modeling hard disks type of interactions with an effective diameter $\sigma_{\text{eff}} = 1.106\,88\sigma$, which has been found to serve as a good value to study for example phase separation in colloidal systems [65, 76, 99].

The *perception* of each particle i is given by

$$P_i = \sum_{j=1}^{N} \frac{1}{2\pi r_{ij}} \Theta(\hat{\boldsymbol{r}}_{ij} \cdot \boldsymbol{c}_i - \cos\alpha)\Theta(r_{\text{cut}} - r_{ij}), \tag{3.2}$$

where, $r_{ij} = |\boldsymbol{r}_j - \boldsymbol{r}_i|$ is the interparticle distance, $\hat{\boldsymbol{r}}_{ij} = (\boldsymbol{r}_j - \boldsymbol{r}_i)/|\boldsymbol{r}_j - \boldsymbol{r}_i|$ the normalized interparticle distance vector, and $\boldsymbol{c}_i \equiv [\cos(\phi_i + \gamma), \sin(\phi_i + \gamma)]^T$ the orientation vector of the vision cone axis of symmetry. The aperture angle of the cone is α, and the *misalignment angle* is γ, which is measured from the symmetry axis of the particle's orientation vector $\boldsymbol{e}_i$ to the symmetry axis of the vision cone, see Fig. 3.1a. $\Theta(\cdot)$ are Heaviside step functions, indicating that neighbouring particles are only perceived when they are located within a restricted cone of vision, i.e. when neighbouring particles are located at radial distances $r_{ij} < r_{\text{cut}}$ and also

within the circular sector described by the aperture angle α of a vision cone with orientation $\boldsymbol{c}_i$, the corresponding condition is $\hat{\boldsymbol{r}}_{ij} \cdot \boldsymbol{c}_i < \cos\alpha$. The perception P_i is maximum when several neighbouring particles fill the vision cone of particle i without leaving any empty gaps, i.e. in a close-packed configuration. On the other hand, P_i vanishes when particle i perceives no neighbours, e.g. when $\boldsymbol{c}_i$ is pointing into and empty region. Note that the perception corresponds to a long-range interaction $P_i \sim 1/r_{ij}$, as long as the cutoff radius is chosen large enough. Furthermore, it is an additive quantity, implying that the observer's perception due to a single neighbor at a distance r is equal to the perception of N neighbors at a distance Nr. This type of perception has been employed in previous studies of colloidal spheres and rods [45, 147]. An important aspect of a visual-type of perception is that it corresponds to an anisotropic interaction, given that $\alpha < \pi$. This means that interactions are *non-reciprocal*, i.e. a particle i might perceive another particle j, however particle j might not perceive particle i. See Fig. 3.1b. Non-reciprocal interactions are important in systems of active particles because they lead to novel and diverse collective behaviors not displayed by the most common pairwise reciprocal interactions [148].

To finish determining our model, we consider that the particle's motility switches between active and passive according to

$$v_i(P_i) = \begin{cases} 0 & P_i < P^* \\ v_0 & P_i > P^* \end{cases}, \tag{3.3}$$

which depends on the particle's perception value P_i and fixed threshold P^*; v_0

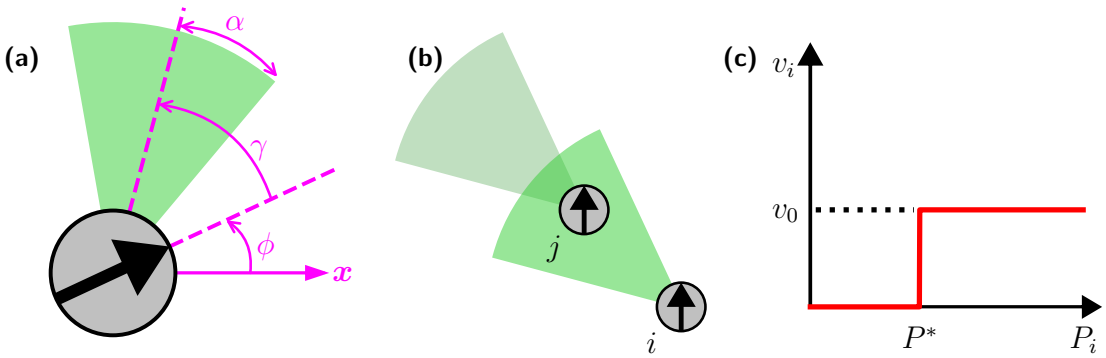

Figure 3.1: *Misaligned perception-dependent motility.* (a) A particle with self-propulsion orientation angle ϕ, vision cone aperture α, and misalignment angle γ. (b) Illustration of a non-reciprocal interaction. Particle i can perceive particle j, however particle j does not perceive particle i. (c) Particle's discontinuous motility v_i depending on the particle's perception P_i and predefined perception threshold P^*.

is a constant self-propulsion speed. See Fig. 3.1c. In the aligned case $\gamma = 0$, this motility rule can be understood as an effective attraction, as particles perceiving an accumulation of neighbours become active and therefore move towards them [45, 147]. In the misaligned case with $\gamma > 0$, the activated particles can also deviate their motion with respect to the neighbour accumulation, thus the effective attraction is diminished, as we will next show.

We consider a system of $N = 1000$ particles homogeneously distributed within circular region of radius $R_0 = 40\sigma$ at time $t = 0$. The corresponding initial number density is therefore $\rho_0 = N/(\pi R_0^2) \approx 0.19\,\sigma^{-2}$, and the area fraction $\phi_0 = N\sigma_{\text{eff}}^2/(4R_0^2) \approx 0.15\,\sigma^{-2}$. In experiments of light-activated colloids described in Ref. [45], the system parameters employed are: colloid's diameter $\sigma = 4.28\,\mu\text{m}$, self-propulsion velocity $v_0 = 0.2\,\mu\text{m}\,\text{s}^{-1}$, translational diffusion coefficient $D_t = 2.3 \times 10^{-2}\,\mu\text{m}^2/\text{s}$, and rotational diffusion coefficient $D_r = 9.3 \times 10^{-3}\,\text{s}^{-1}$. Other experiments of light-activated colloids also performed in Bechinger's lab employ similar parameters [41, 44, 107]. In our simulations, all quantities are expressed in dimensionless units. The unit of length we choose is the particle diameter $\ell = \sigma$ as defined in the Weeks-Chandler-Anderson potential Eq. (2.7), and the unit of time the translational diffusion timescale $\tau = \sigma^2/D_t$. Relevant dimensionless parameters corresponding to those in experiments in Ref. [45] approximate to: self-propulsion velocity $v_0 = 40$, and rotational diffusion coefficient $D_r = 8$. We summarize the correspondence of parameters between experiments and simulations in Table 3.1.

	Experiments	Simulations
D_r	$9.3 \times 10^{-3}\,\text{s}^{-1}$	8
D_t	$2.3 \times 10^{-2}\,\mu\text{m}^2/\text{s}$	1
v_0	$0.2\,\mu\text{m}\,\text{s}^{-1}$	40
σ	$4.28\,\mu\text{m}$	1

Table 3.1: Correspondence between experimental parameters taken from Ref. [45], and the parameters employed in our particle-based numerical simulations.

We perform simulations by numerically integrating Eq. (3.1) using a time step of $\Delta t = 1 \times 10^{-5}\tau$. By default we choose a cone of vision with fixed aperture angle $\alpha = \pi/4$, and $r_{\text{cut}} \gg R_0$ such that all neighbouring particles j are perceived by a particle i, as long as they remain within the circular sector described by the vision cone of i. Following Ref. [45], the perception threshold is chosen to be the perception of a particle located at the center of the initial circular distribution,

$P^* = P_0$, as given by the formula

$$P_0 = \frac{\alpha}{\pi}\rho_0 R_0 = \frac{\alpha N}{\pi^2 R_0}. \tag{3.4}$$

This is a fixed quantity for a given number of particles N, aperture angle α, and initial radius R_0. The derivation of this formula can be found in Ref. [45].

3.1.1 Swirling and collapse

We consider particles with misalignment angle $\gamma = \pi/4$. Snapshots of the system at different times t/τ_B are shown in Fig. 3.2a. Here, $\tau_B = \sigma/v_0 \approx 2.5\times10^{-2}\tau$ is the ballistic timescale, i.e. the time it takes an active particle to travel the colloid's diameter σ. From Fig. 3.2a we observe that the initially diluted system collapses into a single aggregate for the chosen parameters. Furthermore, the resulting aggregate is found to be *cohesive*, i.e. all of the particles remain together over time without diffusing out of the aggregate. While there is translational diffusion due to the Brownian nature of the colloid's dynamics, the activity induced after surpassing the perception threshold leads to an effective attractive force which prevents the particles from diffusing radially out of the aggregate. Note that this is in clear contrast with clusters formed due to motility-induced phase separation in systems of active Brownian particles—there clusters can dynamically break and reform, and they only exist in coexistence with a surrounding gas [66, 70]. The system's collapse can also be seen from particle trajectories, which show an inwards spiraling motion towards the center of the configuration, see Fig. 3.2b. The motility of a particle i switches according to its self-propulsion orientation $\boldsymbol{e}_i$. It becomes active when $\boldsymbol{e}_i$ points into the system's center of mass, and changes to passive when $\boldsymbol{e}_i$ points out of the center, as observed by the example particles in the figure inset. We also note that the perception distribution changes over time, see Fig. 3.2c. The distribution at $t = 0$ shows a reasonable number of particles that surpass the perception threshold $P^* = P_0$, ensuring them to activate. The perception distribution at long enough times (here $t = 400\tau_B$) is broader, which tell us that in the final state even more particles are above the threshold $P_i > P_0$, and only a smaller fraction of particles remain passive with $P_i < P_0$. This behavior is also observed in snapshots in Fig. 3.2a, where we find most of the particles in the aggregate are active, with only a smaller number of passive particles in the outer layer.

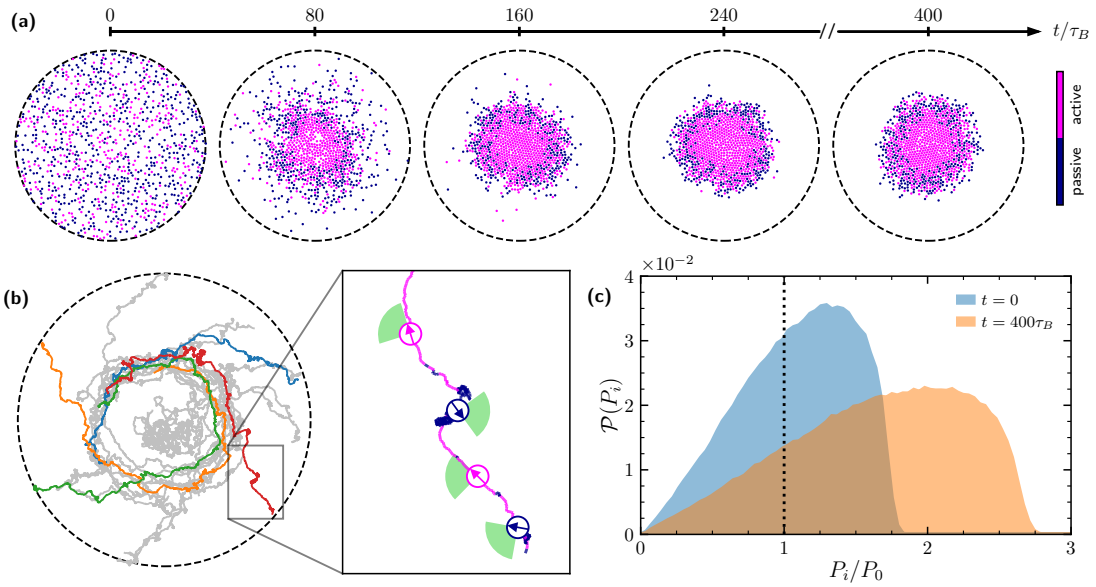

Figure 3.2: *Initial collapse, cohesion, and rotation of the aggregate.* (a) Time evolution snapshots at different times t/τ_B, where $\tau_B = \sigma/v_0$. Dashed lines indicate the circle of radius R_0 within which particles are homogeneously distributed at time $t = 0$. Color code indicates particle's motility. (b) Typical trajectories of the particles. Silver lines indicate 20 randomly selected trajectories. Four of the trajectories are colored to aid visualization. Zoom-in shows the motility switching, with example particle orientations shown by disks with arrows. (c) Probability of finding a particle with perception P_i, at $t = 0$ and at $t = 400\tau_B$. Vertical dotted line indicates the threshold $P^* = P_0$.

3.1.2 Orientation-dependent motility

Cohesion and swirling behavior of the particles can be explained by means of perception radial profiles. To calculate average perception profiles, we consider an initial configuration of homogeneously distributed particles within a circle of radius R_0, and a test particle located at $r = R_0$. The test particle is then considered to vary its orientation depending on the angle $\widetilde{\phi}$, which is defined as the angle between the particle unit vector $-\hat{\boldsymbol{r}}$ and its self-propulsion orientation $\boldsymbol{e}$. Note that both ϕ in Fig. 3.1a, and $\widetilde{\phi}$ defined here refer to the self-propulsion orientation angle; being ϕ given in Cartesian coordinates, and $\widetilde{\phi}$ relative to the center of mass position, see Fig. 3.3a. In other words

$$-\hat{\boldsymbol{r}} \cdot \boldsymbol{e} = \cos\widetilde{\phi}. \tag{3.5}$$

Here, $-\hat{\boldsymbol{r}} = -\boldsymbol{r}/r$ is simply a unit vector pointing from the test particle's center to the system's center of mass $\boldsymbol{r}_{\rm cm}$, which is set to be the origin $\boldsymbol{r}_{\rm cm} = 0$. In Fig. 3.3b, test particles with different orientations $\widetilde{\phi}$ are shown. In-(Out-)oriented particles have self-propulsion orientation $\boldsymbol{e}$ parallel(anti-parallel) to $-\hat{\boldsymbol{r}}$, thus in this case $\widetilde{\phi} = 0(\widetilde{\phi} = \pi)$. Co-oriented (Co) and anti-oriented (Ao) particles have $\boldsymbol{e}$ perpendicular to $-\hat{\boldsymbol{r}}$, with orientation angle $\widetilde{\phi} = -\pi/2(\widetilde{\phi} = \pi/2)$. For comparison, we also show here the cases with $\widetilde{\phi} = -\pi/4, \pi/4$. We numerically calculate the perception radial profiles $P(r)$ for each of the test particles considered, by computing Eq. (3.2) at several radial distances $0 < r < 2R_0$ while keeping fixed orientation angle $\widetilde{\phi}$. In this calculation the system does not evolve, but considers only to the initial configuration at $t = 0$. To improve statistics, we average over 60 independent initial configurations. The results are shown in Fig. 3.4. The obtained $P(r)$ show a non-monotonous dependence for In- and Co-oriented particles, as well as for test particles with $\widetilde{\phi} = -\pi/4$. In all those cases, $P(r)$ has a maximum at $r = R_0$ where test particles perceive the largest number of neighbors. Then, at $r > R_0$ the perception decays monotonously due to its $1/r_{ij}$ dependence, see Eq. (3.2). The test particle with $\widetilde{\phi} = -\pi/4$ shows the largest perception value possible $P_i \approx 1.8P_0$, as its cone of vision covers the largest area of the circular region, see Fig. 3.3b. For Out- and Anti-oriented particles, $P(r)$ shows a monotonous decrease and vanishes at $r \geq R_0$. The perception radial

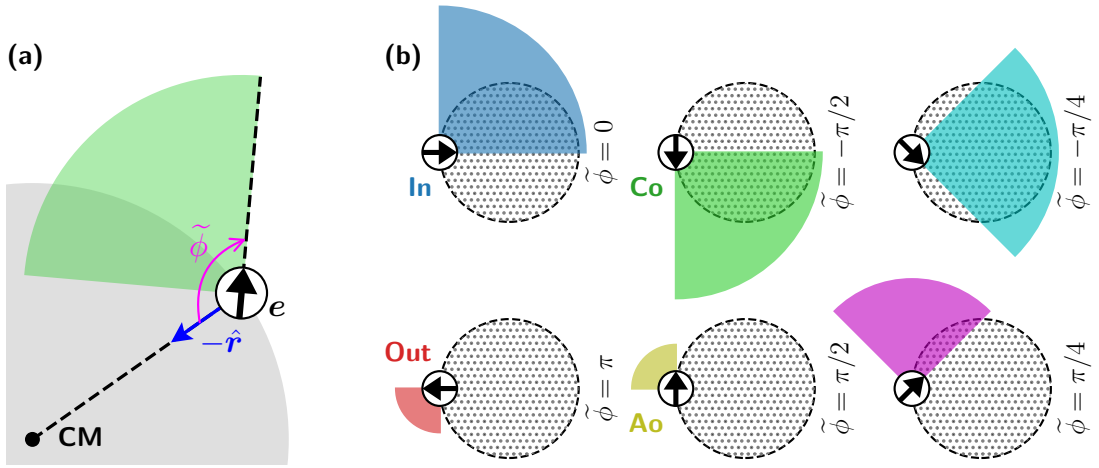

Figure 3.3: *Particle orientations.* (a) Sketch showing showing the self-propulsion orientation angle relative to the center of mass $\widetilde{\phi}$. (b) Test particles with different orientations located at $r = R_0$ with respect to the center of a circular region containing N particles. The vision cone cutoff range $r_{\rm cut}$ is shortened for better visualization.

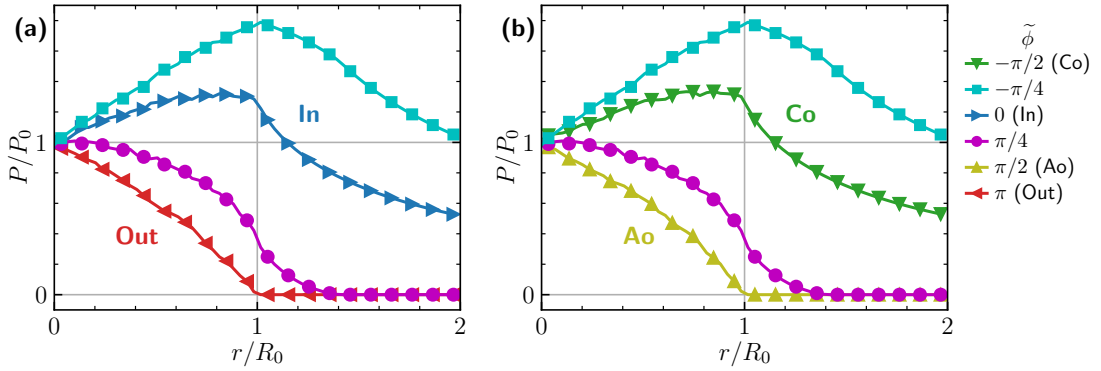

Figure 3.4: *Perception radial profiles* $P(r)$. $P(r)$ for test particles located at $r = R_0$ with orientations (a) $\widetilde{\phi} = -\pi/4, 0(\text{In}), \pi/4, \pi(\text{Out})$, and (b) $\widetilde{\phi} = -\pi/2(\text{Co}), -\pi/4, \pi/4, \pi/2(\text{Ao})$.

profile of the test particle with $\widetilde{\phi} = \pi/4$ also shows a monotonous decrease, with $P(r)$ slightly larger than the perception of Out- and Anti-oriented particles. In all those cases, at $r = R_0$ the vision cone is oriented out of the circular region, thus particles perceive no neighbors, see Fig. 3.3b. Note that $P(r)$ was calculated for $t = 0$, however its behavior at given $\widetilde{\phi}$ is expected to be the same at longer times $t > 0$, as long as the aggregate remains circular.

For all particle orientations considered above, the perception is exactly $P = P_0$ at the origin $r = 0$. Now, by choosing the perception threshold to be $P^* = P_0$, we guarantee that In-oriented particles become active at distances $r < R_0$, because there the perception threshold is surpassed $P > P^*$. On the other hand, Out-oriented particles remain passive at any radial distance, as there the perception radial profiles show that $P < P^*$ holds for $r > 0$. This ensures the collapse of the system into a smaller cohesive aggregate for the chosen system parameters. The only way particles might leave the aggregate is due to passive translational diffusion. For example, Out-oriented particles passively diffuse out of the aggregate, until they eventually reorient due to rotational diffusion and $\boldsymbol{e}$ points into the aggregate, then they actively rejoin with speed v_0. This is possible as here rotational diffusion is a much faster process than the translational diffusion, as seen from the timescale $\tau_r = 1/D_r \approx 0.1\tau$. Similarly, Co-oriented particles are ensured to become active, while Ao-particles remain passive. This imbalance induces the swirling motion of the particles, as Co-particles self-propel tangential to the circular distribution. The rotation is in the counter-clockwise direction for the chosen $\gamma = \pi/4$, see Fig. 3.2b. For negative misalignment angle $\gamma = -\pi/4$ the rotation would be in the clock-wise direction. In a nutshell, we can say that the effect of the vision cone misalignemnt is to select as active those particles that are In-

and Co-oriented, and as passive those that are Out- and Anti-oriented, such that particles display an orientation-dependent motility due to misaligned visual perception. This translates into an effective attractive force and a net torque acting on the system, ensuring the system's cohesion and rotation in steady state.

3.2 Metastable crystal aggregates

The perception of a particle i is in general a dynamical quantity, $P_i = P_i(t)$, which depends both on the particle orientation $\boldsymbol{e}_i$ and the system's configuration at time t. As the system collapses into a cohesive aggregate, the inter-particle distances r_{ij} become smaller, therefore the perception P_i is expected to increase in time, given that $P_i \sim 1/r_{ij}$ from definition Eq. (3.2). For the system's preparation, one needs to choose an initial radius R_0 within which the particles are homogeneously distributed. Following Ref. [45], the perception threshold value is set to $P^* = P_0$, i.e. the perception of a particle located at the center of the initial circular configuration, as defined in Eq. (3.4). Note that this value of the perception threshold is small for an initially large system, and large for a small system, given that $P_0 \sim R_0^{-1}$. Therefore, on collapse, a system started with a large initial radius R_0 is expected to have a larger fraction of active particles, as the threshold set to P_0 is small enough in that case. Such behavior is shown in Fig. 3.2a,c. Conversely, if the system is started with smaller R_0, the system is expected to have a smaller fraction of active particles, as P_0 is larger in that case. Moreover, the activity distribution can affect the aggregate's internal structure. For this reason, choosing the threshold to be $P^* = P_0$ is not completely adequate if we aim to achieve a given final configuration independent of the initial condition.

In this section, we characterize the aggregation mechanism by means of dynamic parameters accounting for the system's hexatic order, activity, and perception of the particles. Here we consider only the case $\gamma = 0$, as this parameter does not have a strong effect on the aggregate's activity distribution for a given perception threshold P^*, as we show in Sec. 3.3. We show the resulting aggregate structure and activity distribution strongly depends on the initial conditions when choosing $P^* = P_0$. Then we define a different perception threshold $P^* = P_c$ which is independent of the initial configuration, corresponding to the formation of a crystal aggregate with homogeneous activity distribution.

3.2.1 Dependence on the initial configuration

To illustrate this point, we performed simulations of $N = 1000$ particles with $\gamma = 0$ homogeneously distributed within a circle of radius R_0. Each simulation

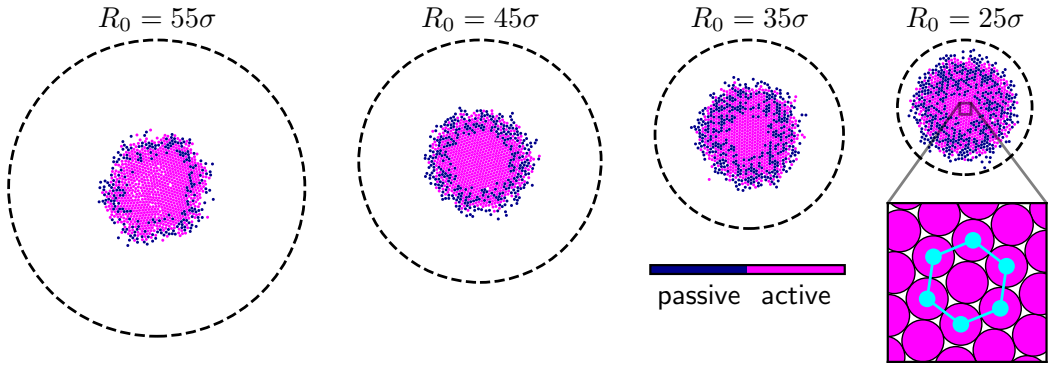

Figure 3.5: *Final configuration dependence on the initial circle radius* R_0. Snapshots of the final configuration in steady state at $t = 500\tau_B$ for various values of R_0. Dashed line indicates R_0. Zoom-in indicates hexagonal close packing.

was started with a different value of the initial radius, namely $R_0/\sigma = 25$–60, at fixed threshold $P^* = P_0$. In Fig. 3.5a we see snapshots of the final configurations at time $t = 400\tau_B$, which corresponds to the stationary state. As discussed in the previous section, choosing the threshold to be $P^* = P_0$ guarantees particles to become active when they are In-oriented and passive when they are Out-oriented. Therefore, in all cases the system collapses into a single cohesive aggregate. The collapse can be characterized by the radius of gyration

$$R_g^2(t) = \frac{1}{N}\sum_{i=1}^{N} |\boldsymbol{r}_i(t) - \boldsymbol{r}_{\rm cm}(t)|^2, \tag{3.6}$$

which accounts for the time dependent spread of the particles around the center of mass of the system $\boldsymbol{r}_{\rm cm}$. In Fig. 3.6a-b, we observe that systems started with larger R_0 take a longer time to reach the stationary state. However, in all cases tested here the system collapse into compact aggregates with $\overline{R_g} \approx 13\sigma$. [1].

The aggregates in steady state display an hexagonal close packing internal structure, as can be seen in the inset of Fig. 3.5a. To quantify this, we calculate the local hexatic order parameter

$$\psi_{6,i} = \frac{1}{n_i}\sum_{j=1}^{n_i} \exp(i6\theta_{ij}), \tag{3.7}$$

where the sum goes over the six nearest neighbors n_i of a particle i, and the angle θ_{ij} corresponds to the polar angle described by the inter-particle particle

[1] Note that the radius of gyration is not the unique quantity to characterize the physical size of the aggregate R_c, which can also be calculated from density radial profiles, as we introduce in Chapter 4.

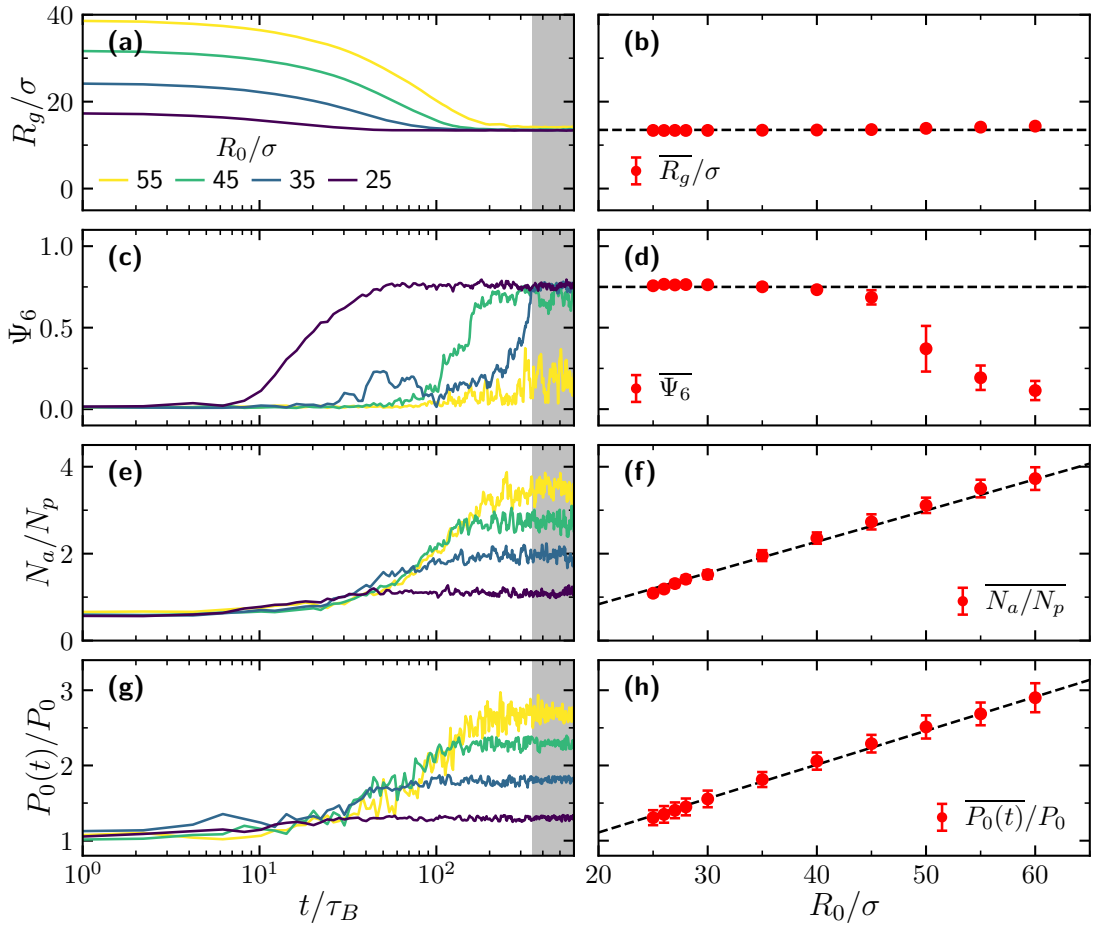

Figure 3.6: *Dynamic parameters dependence on the initial circle radius* R_0. Time evolution and average in steady state of the dynamical quantities: (a,b) radius of gyration R_g normalized by the particle diameter σ; (c,d) hexatic order parameter Ψ_6; (e,f) ratio between number of active particles N_a and number of passive particles N_p, and (g,h) perception function at the center of the particle configuration $P(t, r = 0)$, normalized by the perception at the center of the initial circle P_0. Shaded region in (a,c,e,g) indicate the stationary state time interval. Dashed lines in (b,d,f,h) correspond to a linear fit of the data points. In (d) the fit is taken only for data points $R_0 \leq 40\sigma$.

distance $\boldsymbol{r}_{ij}$. The local hexatic order is a complex number of modulus $|\psi_{6,i}| \leq 1$. The average hexatic order parameter is then

$$\Psi_6 = \left| \frac{1}{N} \sum_{i=1}^{N} \psi_{6,i} \right| . \tag{3.8}$$

This is a global quantity vanishing when the system is loose, and is maximum with $\Psi_6 = 1$ when the system display a perfect crystal structure with all particles placed at the nodes of a triangular lattice, each of them therefore with six-fold orientational order. For the system under study, Ψ_6 never reaches the upper bound, as there are particles in the outer layer, i.e. at the aggregate's interface, where the system is more fluid and particles are free to move. In Fig. 3.6c-d, we observe that $\Psi_6(t)$ saturates in steady state at a value of $\langle\Psi_6\rangle \approx 0.75$ for systems started at $R_0 \leq 45\sigma$, and for initially larger systems $\langle\Psi_6\rangle$ is found to become smaller. The reason of this decrease is that the aggregate's internal structure is strongly affected by the activity distribution. In the snapshots in Fig. 3.5a, we observe that for the initial configuration of radius $R_0 = 55\sigma$ the system is composed mainly by active particles, whereas for the smaller initial radius, $R_0 = 25\sigma$, the resulting aggregate only active particles in the center, and an active-passive mixture in the outer layer.

Changes in activity are quantified by the ratio N_a/N_p, where N_a is the number of active particles and N_p the number of passive particles at a given time t. The ratio increases as the system collapses, see Fig. 3.6e. The corresponding steady state values are shown in Fig. 3.6f, showing a linear growth with R_0. In Fig. 3.6g the time evolution of the perception at the aggregate's center $P_0(t) = P(r = 0, t)$ is shown, which is calculated from simulation data for the particle closest to $\boldsymbol{r}_{\mathrm{cm}}$ at a given time t. The steady state values in Fig. 3.6g show a linear growth of the normalized quantity $\overline{P_0(t)}/P_0$ with R_0. This dependence is evident as the denominator $P_0 \sim {R_0}^{-1}$ by definition, and therefore the numerator $\overline{P_0(t)}$ should be constant as R_0 increases. This behavior can be understood because in steady state the aggregate has reached a minimum size, thus the inter-particle distances r_{ij} remain constant (except for small fluctuations in the outer layer where particles can move freely), leading to a constant perception for a particle located at the center $r = 0$.

3.2.2 Perception at the center of a crystal aggregate

A better approach to normalize the perception function is to employ a normalization factor which does not depend on the initial condition. A suitable quantity for this is the perception of a particle at the center of a *crystal aggregate*, i.e. an aggregate of minimum size displaying hexagonal close packing, which we have found is the type of structure obtained in steady state. Crystal structures have been found to emerge in different systems of active particles due to various mechanisms, e.g. it has been found in diffusiophoretic colloids [149, 150], and light-manipulated colloids with delayed attractions [151], and swimming starfish embryo [152]. The area covered by disks of diameter σ in an hexagonal unit cell, like the one shown

in the inset of Fig. 3.5a, is exactly the area covered by three disks of area $\pi\sigma^2/4$ each, and the area of the hexagonal unit cell itself corresponds to the area of six equilateral triangles of side σ, i.e. six triangles of area $\sqrt{3}\sigma^2/4$ each. Therefore, the area fraction of a system in hexagonal close packing is

$$\phi_{\text{hex}} = \frac{3\pi\sigma^2/4}{6\sqrt{3}\sigma^2/4} = \frac{\pi}{2\sqrt{3}} \approx 0.9. \tag{3.9}$$

The area fraction of a crystal aggregate of size R_c with perfect hexagonal close packing is $\phi_{\text{hex}} = N\sigma^2/(4R_c^2)$, and the corresponding number density given by $\rho_c = 4\phi_{\text{hex}}/(\pi\sigma^2)$. Then we can calculate the perception of a particle located at the center of a compact aggregate from the formula

$$P_c = \frac{\alpha}{\pi}\rho_c R_c = \frac{2\alpha}{\pi^2\sigma}\sqrt{N\phi_{\text{hex}}}. \tag{3.10}$$

We evaluate this formula at $\alpha = \pi/4$, and for the disk diameter we need to employ the effective particle diameter $\sigma_{\text{eff}} \approx 1.10688\sigma$ accounting for the highly repulsive steric interactions in our simulations. The resulting threshold value is $P_c \approx 4.2\sigma^{-1}$.

In Fig. 3.7a, the final configuration of a system of particles with perception threshold set to $P^* = P_c$ is shown. The resulting aggregate in steady state shows an homogeneous activity distribution in the whole structure (both in the center and the outer layer). This distribution is different compared to the distribution in steady state obtained by setting $P^* = P_0$, see Fig. 3.5a, which is found to be homogeneous in activity only in the outer layer, while keeping a center of active particles. Furthermore, in Fig. 3.7b we observe the internal structure of the aggregate in steady state displays six-fold orientational order. In Fig. 3.7c are shown the time evolution of dynamical parameters. The hexatic order parameter increases and saturates at $\Psi_6 \approx 0.75$—whereas the internal structure displays six-fold orientational order, the more fluid outer layer diminishes Ψ_6. Similarly, the active-to-passive number ratio also saturates at $N_a/N_p \approx 0.75$. Note that while the activity distribution is homogeneous, it is non-equimolar with $N_a > N_p$. Furthermore, we verify the perception at the crystal aggregate center increases and saturates at $P_0(t) = P_c$. In Fig. 3.7d steady state quantities are shown, which present an abrupt drop to zero at $R_0 > 35\sigma$. The reason for this, is that in those cases the system does not aggregate at all, instead the system remain a passive gas with $\Psi_6 = 0$, $N_a = 0$ and $P_0(t) \approx 0.4P_c$. This is an indication of the metastability of the crystal aggregates. Particles in an initially dilute system with density ρ_0 require to perceive a large density fluctuation $\delta\rho$, i.e. a significant accumulation of particles, in order to activate and initiate the system's collapse

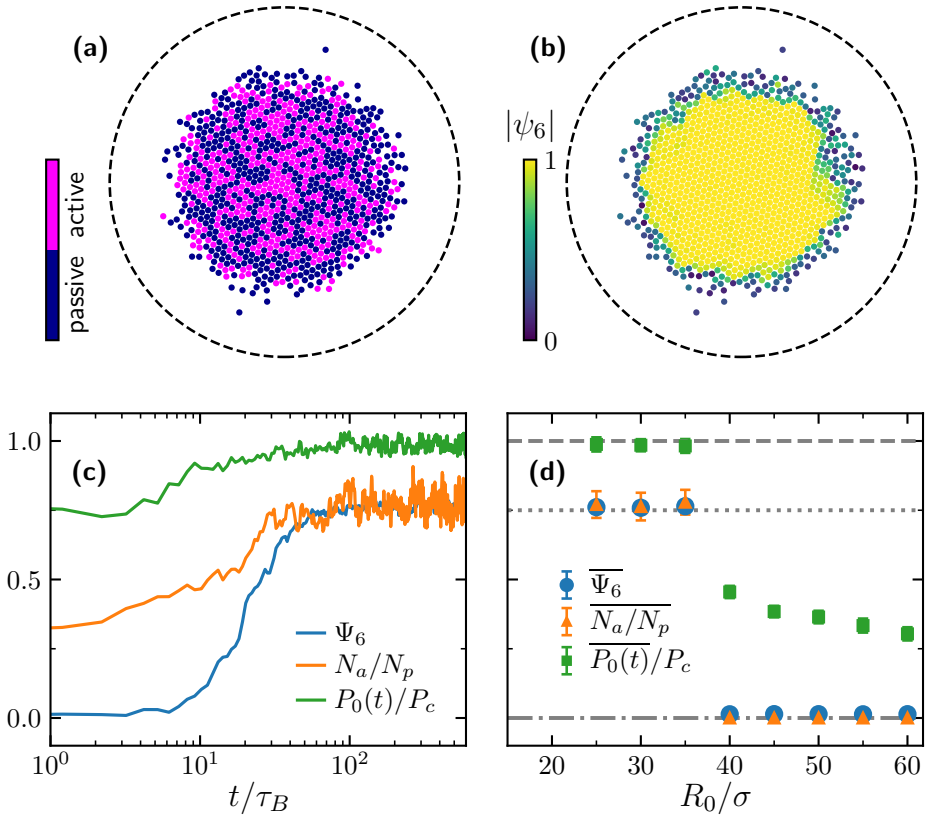

Figure 3.7: *Crystal aggregate at* $P^* = P_c$. Snapshot of a final configuration color coded by (a) motility, and (b) local hexatic order ψ_6. Dashed line indicates the initial radius $R_0 = 30\sigma$. (c) Time evolution of dynamic parameters, namely the average hexatic order Ψ_6, the active-passive number ratio N_a/N_p, and the perception at the aggregates' center, $P_0(t)$, normalized by the perception of an compact aggregate with hexagonal close packing P_c. (d) Average dynamical parameters in steady state for different values of the initial radius R_0. Horizontal lines are shown as a guide to the eye.

[2].Initially large systems are less likely to display a large $\delta\rho$ when $P^* = P_c$, as P_c is a threshold too high to surpass in that case, then particles there remain passive and do not accumulate but spread out due to thermal diffusion. On the other hand, initially small systems start perceiving neighbors at closer distances,

[2]An instability criterion was derived in Ref. [45] showing a density perturbation $\delta\rho$ increases if $\boldsymbol{e} \cdot \nabla\delta\rho/\delta\rho < 0$, meaning particles tend to accumulate where they are typically oriented opposite to density gradients, and aligned particles *always* move away from regions where the density perturbations decreases.

as $P_i \sim 1/r_{ij}$, $\delta\rho$ in that case does not need to be so large, perception threshold is likely to be surpassed, so particles activate and initiate the system's collapse. In other words, a system can be either diluted or a crystal aggregate, depending on the initial interparticle distances r_{ij}.

The previous discussion allow us to introduce a normalized perception threshold independent of the initial conditions,

$$q^* = \frac{P^*}{P_c}, \tag{3.11}$$

which is employed in the rest of the thesis, and we refer to it simply as *perception threshold*. A value of $q^* = 1$ corresponds to the perception of a particle in the center of an aggregate with an homogeneous activity distribution, besides it is non-equimolar with $N_a = 0.75N_p$, and displays hexagonal close packing with $\Psi_6 = 0.75$, see Fig. 3.7. As P_c is a fixed quantity, varying q^* corresponds to varying P^* only.

3.3 Dynamical properties

In Ref. [45] particles with *frontal* perception $\gamma = 0$ were considered, see Fig. 3.8a. They show that a group of particles initially distributed within a circle of radius R_0 collapses into a small aggregate of size $R < R_0$. Particles there perform directed motion towards the center of mass when they are active, and random Brownian motion when they are passive. So far, we have considered the case when visual perception is misaligned with $\gamma/\pi = 0.25$ (see Fig. 3.8b), showing in this case particles aggregate by performing swirling motion towards the center of mass until the system forms a single compact and rotating structure. Due to the swirling motion, particles with $\gamma \neq 0$ display longer trajectories during collapse, and we expect the time to reach steady state to increase with γ. In this section we investigate such dynamical collapse, as well as the rotation process for varying values of the misalignment angle $\gamma/\pi \in (0, 0.5)$, where the case $\gamma/\pi = 0.5$ corresponds to *lateral* visual perception, see Fig. 3.8c. We also investigate the characteristic collapse time, giving a measure of how long it takes for the system to reach stationary state.

3.3.1 Collapse process

To investigate the aggregation process at given γ, we obtain the radius of gyration R_g as defined in Eq. (3.6), for a system of $N = 1000$ started as an homogeneous density distribution within a circle of radius $R_0 = 30\sigma$. The perception

threshold is set to $q^* = 1$. Other simulation parameters are as those in Table 3.1. In Fig. 3.9a, we observe that for values of the misalignment angle $0 \leq \gamma/\pi \leq 0.46$, the radius of gyration $R_g(t)$ monotonically decreases from its initial value $R_g(0)$. At longer times $R_g(t)$ saturates, corresponding to the steady state where the system is an aggregate of size $R < R_0$ which depends on γ. For larger values of the misalignment angle $\gamma/\pi > 0.46$, $R_g(t)$ grows in time without saturating. In this case, particles do not aggregate but radially diffuse due to translational Brownian motion such that the system does not reach stationary state due to the lack of

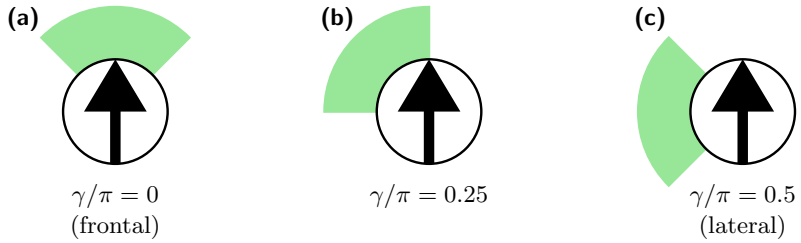

Figure 3.8: *Particles with different misalignment angles* γ. Sketches of particles with (a) frontal perception $\gamma = 0$, (b) misaligned perception $\gamma/\pi = 0.25$, and (c) lateral perception $\gamma/\pi = 0.25$.

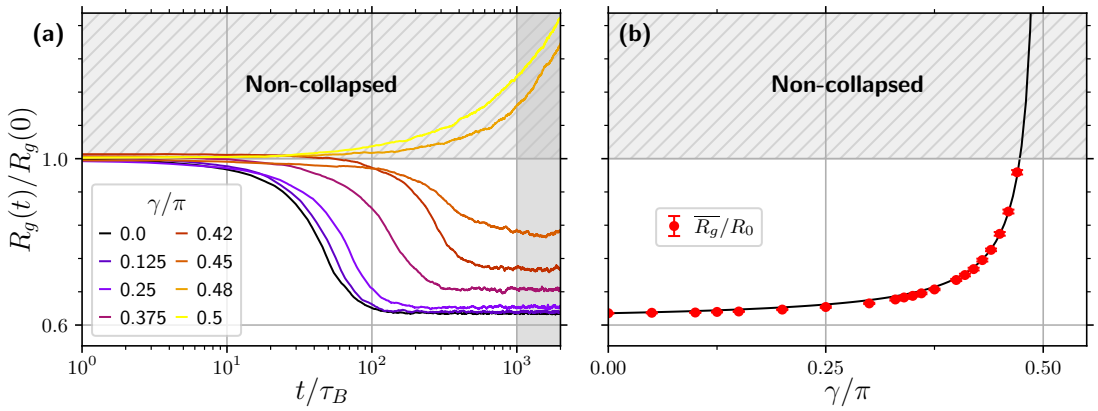

Figure 3.9: *Dynamics of the aggregate's collapse.* (a) Time evolution of the radius of gyration R_g. Shaded region $t/\tau_B > 1 \times 10^3$ corresponds to a time window where cohesive aggregates are in steady state, i.e. systems with $R_g(t) < R_g(0)$. Hashed region $R_g(t) > R_g(0)$ corresponds to non-collapsed systems. (b) Time-averaged radius of gyration $\overline{R_g}$ in steady state. Error bars indicate standard deviation. Solid line corresponds to a fit of the data points using Eq. (3.12).

boundaries in our setup.

We obtain the time-averaged radius of gyration $\overline{R_g}$ in the steady state, calculated by averaging over a time window of $\Delta t/\tau_B = 1\times10^3$–$2\times10^3$ when aggregates are in steady state. In Fig. 3.9b we observe that $\overline{R_g}$ remains reasonably constant for $0 < \gamma/\pi < 0.25$, with $\overline{R_g} \approx 0.62R_g(0)$. For $0.25 < \gamma/\pi \leq 0.45$, we observe $\overline{R_g}$ increases, with values still below $R_g(0)$, meaning the system is collapsed in those cases. We fit the obtained data with the phenomenological function

$$\overline{R_g}(\gamma) = R_g^{\min} + R_g(0)\left[\frac{1}{1-2\gamma/\pi} - 1\right] b, \tag{3.12}$$

where $R_g^{\min} \approx 0.62R_g(0)$ corresponds to the radius of gyration of a compact aggregate, and $b \approx 0.01$ is a fit parameter. The form of this formula satisfies the limits: (i) $\gamma = 0$, the term within brackets vanishes, giving $\overline{R_g} = R_g^{\min}$; (ii) $\gamma = \pi/2$, the term within brackets diverges.

Particles with near lateral perception $\gamma/\pi > 0.46$ have a vision cone which is almost perpendicular to the self-propulsion direction of motion. Thus, they activate only when oriented tangential to the system's center, with a co-oriented cone of vision so they perceive enough neighbors and surpass the threshold q^*. In this case there is no special preference for In- or Out-oriented particles to become active, and therefore there is no net attractive force to keep the system cohesive. The divergence at $\gamma = \pi/2$ corresponds to cases when the system is non-collapsed and does not reach steady state.

The radius of gyration needs a certain time to reach stationary state. This characteristic collapse timescale τ_c can be obtained from the middle point between the saturated $\overline{R_g}$ and initial value $R_g(0)$. We employ

$$R_g(\tau_c) = \frac{1}{2}\left[R_g(0) - \overline{R_g}\right], \tag{3.13}$$

which is positively defined for collapsed systems. Then the collapse time is obtained by inverting this equation as $\tau_c = \tau_c(R_g)$. In Fig. 3.9 we see a monotonous increase of τ_c with γ. For frontal perception $\gamma = 0$ the steady state is reached the fastest giving the minimum collapse time $\tau_c^{\min} \approx 40\tau_B$, whereas for near lateral perception $\gamma/\pi \approx 0.46$ the collapse takes much longer, approaching large values of $\tau_c \approx 1 \times 10^3\tau_B$. Our numerical data approximates the function

$$\tau_c(\gamma) = \tau_c^{\min} + \tau_c^{\min}\tan(\gamma), \tag{3.14}$$

which diverges at $\gamma = \pi/2$ and for frontal perception $\gamma_c(0) = \tau_c^{\min}$. We observe that for misalignment angles between $0 < \gamma/\pi < 0.375$, the steady state is reached sooner, so the collapse time is small with $\tau_c/\tau_B < 1 \times 10^2$ but larger than the

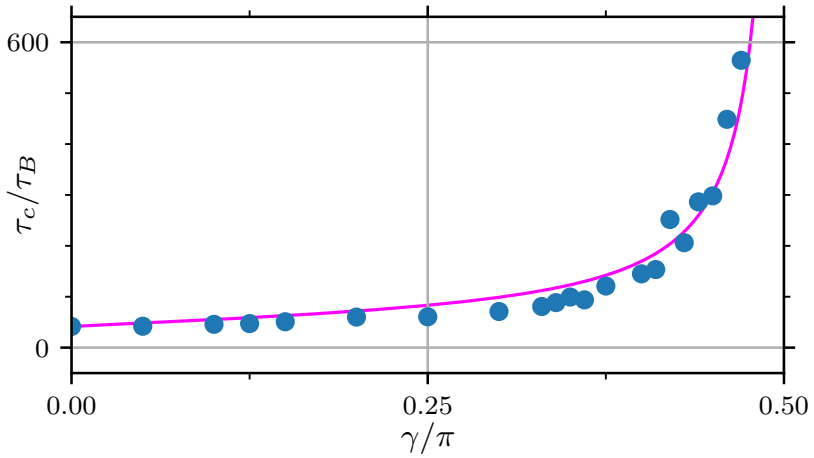

Figure 3.10: *Collapse timescale* τ_c. Dots correspond to data obtained using Eq. (3.13), and solid line corresponds to Eq. (3.14).

minimum value $\tau_c^{\min}$. For $0.375 < \gamma/\pi < 0.5$, reaching the steady state takes much longer, showing collapse times within the range $100 < \tau_c/\tau_B < 600$. We conclude that a system at $q^* = 1$ and given γ will be found in steady state at $t > 600\tau_B$ as long as the system collapses, which is the case for most values of γ.

3.3.2 Rotational order

Particles' trajectories display swirling motion when $\gamma \neq 0$. This is observed during the transient collapse, then in stationary state once the system has become a compact aggregate, trajectories show a circular motion as they do not displace much in the radial direction. We quantify this behavior by computing the rotational order parameter, defined as

$$O_R(t) = \frac{1}{N}\sum_{i=1}^{N} \hat{\boldsymbol{r}}_i \times \hat{\boldsymbol{v}}_i, \tag{3.15}$$

where the unit position vector $\hat{\boldsymbol{r}}_i$ is measured from the aggregate's center of mass $\boldsymbol{r}_{\mathrm{cm}}$, and $\hat{\boldsymbol{v}}_i = \boldsymbol{v}_i/|\boldsymbol{v}_i|$ is the normalized velocity vector. Here, velocity $\boldsymbol{v}_i = \Delta\boldsymbol{r}_i/\Delta t$ is computed for a displacement given by $\Delta\boldsymbol{r}_i = \boldsymbol{r}(t+\Delta t) - \boldsymbol{r}(t)$ during a small time interval $\Delta t = 2\tau_B$. Note that typically $\boldsymbol{v}_i$ is different from the self-propulsion velocity $v_0\boldsymbol{e}_i$. In general, the orientation vector field $\boldsymbol{e}$ is isotropic, as the dynamics of the rotational degree of freedom ϕ is governed only by rotational diffusion, see Eq. (3.1). Conversely, the normalized velocity vector field $\hat{\boldsymbol{v}}$ of a rotating compact aggregate shows a clear rotational order. See Fig. 3.11. The

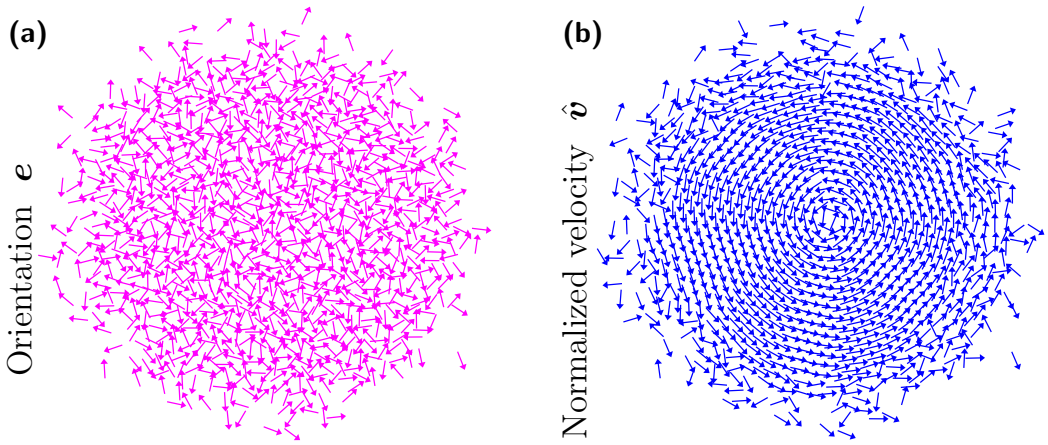

Figure 3.11: *Orientation $\boldsymbol{e}$ and normalized velocity $\hat{\boldsymbol{v}}$.* Vector field snapshots corresponding to a steady state compact aggregate at $q^* = 1$ and $\gamma/\pi = 0.25$. (a) Orientation vector field $\boldsymbol{e}$. (b) Normalized velocity vector field $\hat{\boldsymbol{v}}$.

order parameter O_R accounts for the overall rotation of the system. It vanishes when the system does not rotate, and $|O_R| = 1$ when all of the particles simultaneously rotate. O_R is positive for counter-clockwise rotations (which is the case for misalignment $\gamma > 0$), and negative for clockwise rotations. Intermediate values correspond to a fraction of the system rotating in a given direction. In Fig. 3.12a we observe the time evolution of O_R grows from an initial value $O_R \approx 0$, and saturates in steady state for collapsed cases with $0 < \gamma/\pi < 0.48$. The maximum value observed is $O_R \approx 0.8$. The upper bound $O_R = 1$ is never reached, as there exist a fraction of passive particles with isotropic velocity $\boldsymbol{v}_i$ at the outer layer of the aggregate, where particles are free to diffuse. In chapter 4 we discuss in more detail the activity distribution of the aggregate, and how this affects the overall rotation.

In Fig. 3.12b time-averages $\overline{O_R}$ in steady state for different values of γ are shown. Note that for the smaller misalignment angle values tested $\gamma/\pi = 0, 0.05$ the standard deviation of $\overline{O_R}$ is very large. There, the normalized tangential velocity $\hat{\boldsymbol{r}}_i \times \boldsymbol{v}_i/|\boldsymbol{v}_i|$ fluctuates strongly, as the motion of particles are on average directed towards the center of mass, without a strong bias to tangentially drive the system. We find our data fits the phenomenological function

$$O_R(\gamma) = O_R(\pi/4) - O_R(\pi/4)\left[1 - \frac{4}{\pi}\gamma\right]^4, \tag{3.16}$$

which is chosen to be symmetric around $\gamma = \pi/4$, and to vanish both at $\gamma = 0$ and $\gamma = \pi/2$. Thus, $\overline{O_R}$ displays a non-monotonous behavior, with maximum

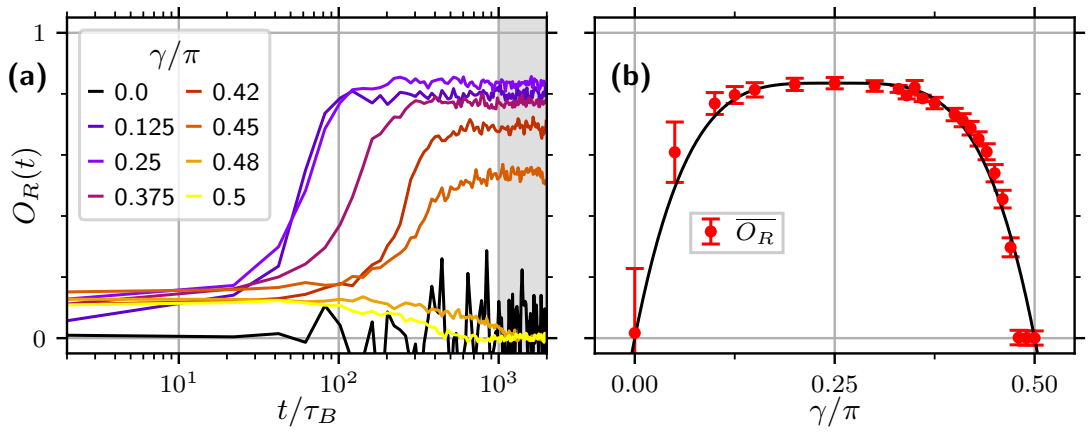

Figure 3.12: *Rotational order of the normalized velocity field* $\hat{\boldsymbol{v}}$. (a) Time evolution of the rotational order parameter O_R. (b) Time-averaged rotational order parameter $\overline{O_R}$ in steady state. Black solid line in (d) shows a fit of the data points using Eq. (3.16).

value at $\gamma = \pi/4$. Interestingly, the rotational order plateau over a wide range of values around the maximum, namely $0.125 < \gamma/\pi < 0.375$. This behavior is closely related to short-range steric interactions. As in those cases the system is compact, the particles within the aggregate will perform a coherent rotation. Even when the activity distribution is homogeneous there, passive particles are still dragged by active ones.

3.4 Summary

We described a model that generically leads a system of particles to self-organize into rotating cohesive aggregates. The cohesion and rotation mechanism was explained by means of perception radial profiles. We found misalignment has the effect of selecting as active those particles with a cone of vision that is either in- or co-oriented with the aggregate's center, where the largest particle accumulation is found. This effect translates into an effective attractive force keeping the particles together, as well as a net torque driving the system to rotate.

We found that choosing a perception threshold to be the perception of a particle at the center of a compact aggregate, i.e. a configuration in hexagonal close-packing, leads to the formation of compact aggregates with homogeneous activity distribution. Such configurations are only possible when the system is started as homogeneously distributed particles within a small circular radius R_0, close to the minimum aggregate size. The structures there correspond to rotating

crystal aggregates. The dynamics of the collapse and rotation of the aggregates were studied by means of the radius of gyration R_g as well as the rotational order parameter O_R. We found that the steady state values of R_g grow with γ, diverging for lateral perception $\gamma = \pi/2$ where cohesion of the aggregates is lost. The rotational order parameter O_R was found to be non-monotonous, showing maximum rotational order for intermediate values of γ.

4 Control of the aggregate's structural properties

In the previous chapter we have described a system of colloids interacting via steric repulsion and misaligned perception-dependent motility. We found that this system generically aggregates into a single structure that remains cohesive due to the anisotropic perception interaction, and furthermore the aggregates rotate due to the symmetry-breaking of the cone of vision orientation with respect to the self-propulsion direction. We also found that after collapse, the system reaches steady state, where the aggregates remain with a fixed size and rotational order, except for cases where the perception is near lateral with misalignment angle $\gamma = \pi/2$.

In this chapter, we systematically study the structural properties of such steady state aggregates by considering control parameters like the misalignment angle γ, the perception threshold q^*, or the Péclet number P_e. We find that tuning these parameters sets an interplay between perception, local activity, and steric interactions, resulting in aggregates of different activity distribution, size, density, interface width, and angular velocity. To quantify this, we fit radial profiles for the density and angular velocity, which allow us to extract size and bulk quantities of the aggregate. Furthermore, we derive analytic expressions for such quantities, obtained by considering an steady state continuum description of the aggregate together with conservation equations and boundary conditions for the perception. Predicted size and bulk properties show good agreement with our numerical results. Finally, we study the interface width of the aggregates, which we find grows with increasing γ and decreasing Péclet number P_e, while remaining unaffected by q^*. This study demonstrates that our model, besides being minimal and generic to obtain rotation of cohesive aggregates, it also serves as a flexible strategy to change the aggregate's structure.

4.1 Measurement of structural properties

To provide a quantitative characterization of the aggregates structure, we obtain steady-state radial profiles of the local number density ρ, the radial and tangential polarization components p_r and p_t, respectively, and the angular velocity ω. Radial profiles are calculated at time t by subdividing the space into n concentric rings with origin set to the system center of mass $\boldsymbol{r}_{\mathrm{cm}}$. Each concentric ring k is defined by a major radius r_k and minor radius r_{k-1}. Then we average within each ring as follows

$$\rho(r_k) = \left\langle \frac{1}{A_k} \sum_{j \in A_k} 1 \right\rangle, \tag{4.1a}$$

$$\omega(r_k) = \left\langle \frac{1}{A_k} \sum_{j \in A_k} \frac{1}{r_j} \hat{\boldsymbol{r}}_j \times \boldsymbol{v}_j \right\rangle, \tag{4.1b}$$

$$p_r(r_k) = \left\langle \frac{1}{A_k} \sum_{j \in A_k} \hat{\boldsymbol{r}}_j \cdot \boldsymbol{e}_j \right\rangle, \tag{4.1c}$$

$$p_t(r_k) = \left\langle \frac{1}{A_k} \sum_{j \in A_k} \hat{\boldsymbol{r}}_j \times \boldsymbol{e}_j \right\rangle, \tag{4.1d}$$

where $k = 1, \ldots, n$ identifies the k-th ring, $A_k = \pi(r_k^2 - r_{k-1}^2)$ is the concentric ring area, and $\langle \cdots \rangle$ denotes time average in steady state. The sum is performed over particles j located within each concentric ring area A_k. The velocity vector $\boldsymbol{v}_j$ in Eq. (4.1b) corresponds to the physical velocity, i.e. obtained from the particle displacement $\Delta \boldsymbol{r}$ computed over a small time interval $\Delta t = 2\tau_B = 0.05\tau$. Note that, in fact, the radial profiles for the polarization components $p_r(r)$ and $p_t(r)$, as well as for the angular velocity $\omega(r)$ are weighted by the local density, i.e. we sum over j particles within the k-th concentric ring and divide over its area A_k. This weighting diminishes fluctuations in bins where the number of particles is small. To gain better statistics, the average $\langle \cdots \rangle$ is taken over a steady state time window $\Delta t / \Delta \tau_B = 2 \times 10^3$–$3 \times 10^3$.

For the results shown in this section, we performed particle based numerical simulations of $N = 1000$ particles by numerically solving equations Eq. (3.1), employing parameters in Table 3.1. Particles were started within a circle of radius $R_0 = 25\sigma$. Furthermore, we decompose profiles by motility, i.e. we calculate profiles separately considering all particles, actives only, or passives only. For the sake of simplicity, in the following we drop the subscript k denoting the index of the concentric ring radius r_k, and we refer to it simply as the radial distance r. The normalization factors employed are: bulk density of a compact aggregate ρ_c, angular velocity of an active particle in the outside boundary of a crystal

aggregate $\omega_c = v_0/R_c$. Several of the radial profiles we show below behave like a step function with a smooth decay: they plateau within the aggregate (with a constant bulk value), then monotonously decay to zero outside of the aggregate where no particles are left. We say this type of radial profile displays a "step-like" behavior.

4.1.1 Density and rotation speed dependence on γ

First we consider the case with perception threshold set to $q^* = 1$, in order to identify the role of the misalignment angle γ. Snapshots of cohesive aggregates in steady state obtained for different values γ are shown in Fig. 4.1a. We observe that at smaller γ the aggregates are compact, while for larger values they become slightly diluted. This is quantified by the density radial profiles $\rho(r)$. In all three cases: considering all particles, actives only, or passives only; $\rho(r)$ displays a step-like behavior, see Fig. 4.1b. When considering all particles the bulk value is $\rho \approx \rho_c$, for actives only $\rho \lesssim 0.5\rho_c$, and for passives only $\rho \gtrsim 0.5\rho_c$. This shows that the system's activity distribution is homogeneous, while containing slightly less active particles than passive ones. Furthermore, from $\rho(r)$ we find that the aggregate's interface is centered at $r \approx R_c$, and its interface width broadens for larger values of γ.

The angular velocity profile $\omega(r)$ is zero for aligned visual perception $\gamma = 0$, and display a step-like behavior for non-vanishing values of γ, see Fig. 4.1c. The step-like behavior of $\omega(r)$ indicates a solid-body rotation of the aggregate. The bulk angular velocity for $\gamma/\pi = 0.25$ is $\omega \approx 0.2\omega_c$, and it increases for larger γ. For the larger misalignment angle shown here, $\gamma/\pi = 0.375$, we find that the profile's interface is very broad, and the maximum value of ω occurs at the center, approximately $\omega_b \approx 0.6\omega_c$. Active and passive contributions to $\omega(r)$ also show an increase with γ. The bulk values ω_b considering only actives or only passives are correlated to the corresponding bulk density values ρ_b, i.e. ω_b is larger for passives than for actives, as there is a larger number of passives than actives in the bulk. Increasing γ increases the average tangential orientation of the active particles $\boldsymbol{e}_t^a$, and consequently the overall angular velocity ω. We investigate the role of the particle orientations by means of polarization profiles, which correspond to local orientation averages, as defined in Eq. (4.1c), (4.1d). In Fig. 4.1d profiles $p_r(r)$ are shown to vanish when considering all particles. When only active particles are taken into account, we have $p_r < 0$, as on average In-oriented particles with $\hat{\boldsymbol{r}}_j \cdot \boldsymbol{e}_j^a < 0$ perceive a large number of neighbors, thus become active. On the other hand, for passives $p_r > 0$, as Out-oriented particles perceive less neighbors. For actives only, as well as for passives only, the magnitude $|p_r|$ in the bulk is larger for $\gamma = 0$, and becomes small for $\gamma > 0$. The reason of this, is that with

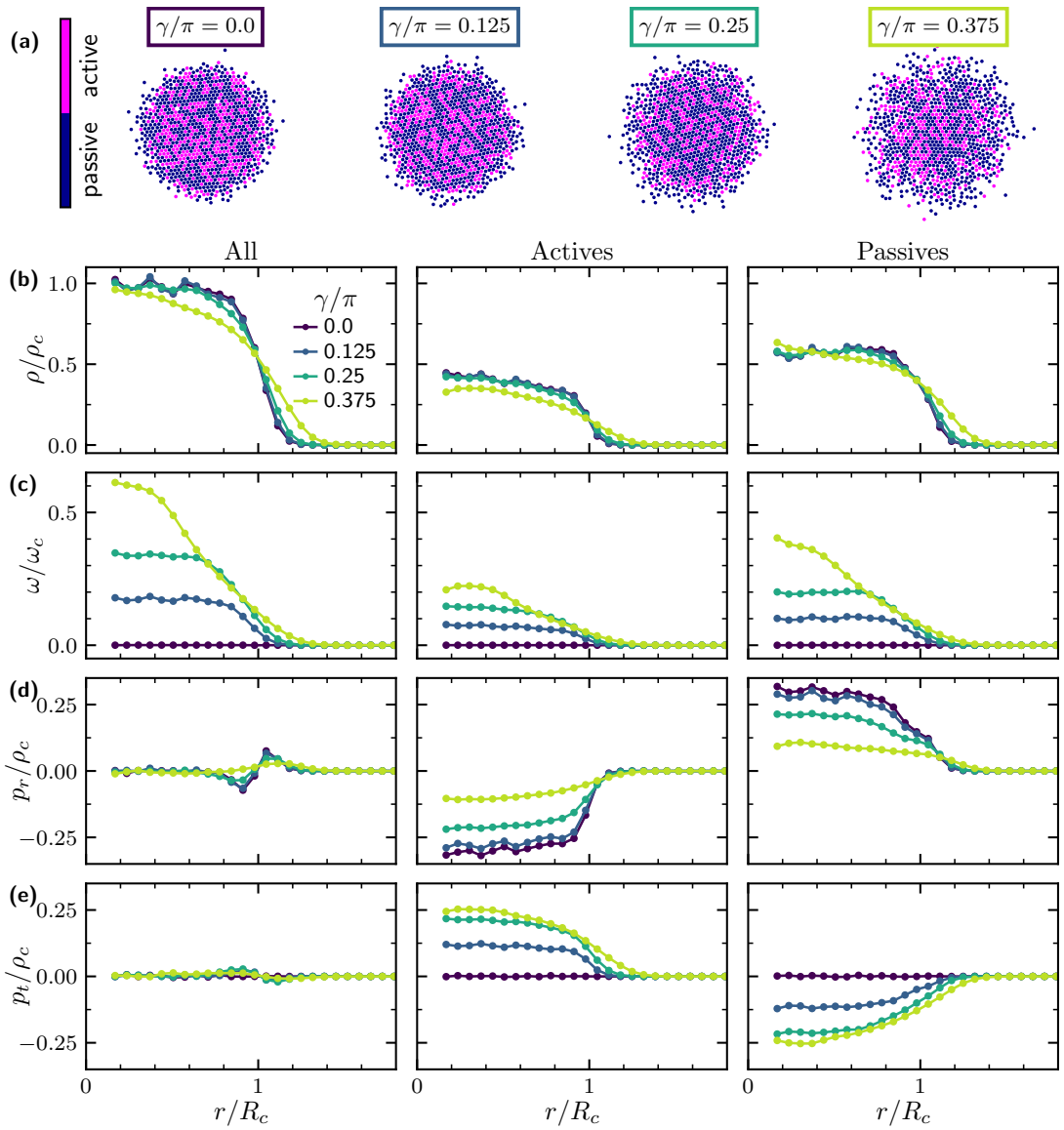

Figure 4.1: *Radial profiles of the aggregate's properties at perception threshold* $q^* = 1$. (a) Snapshots of the collapsed aggregate in steady state for different values of γ. Radial profiles for the aggregate's: (b) number density ρ, (c) angular velocity ω, (d) radial polarization p_r, and (e) tangential polarization p_t. Normalization factors correspond to the density ρ_c, size R_c.

positive misalignment, it is more likely that Co-oriented particles have a preference to become active, and anti-oriented ones to remain passive. However, a non-vanishing polarization of the active particles $|p_r^a|$ is required to ensure cohesion, as those are the ones that tend to compress the cluster. For this reason, the decrease of $|p_r^a|$ with γ is correlated to the increase of the interface width found in $\rho(r)$ and $\omega(r)$. Last but not least, in Fig. 4.1e the tangential polarization radial profiles $p_t(r)$ are shown, which vanish when considering all of the particles, but display a maximum(minimum) when considering only the actives(passives). This indicates that active particles tend to tangentially drive the system, giving rise to the aggregate's rotation, which is coupled to the observed increase in angular velocity. For the aligned case $\gamma = 0$, the component p_t remains zero.

4.1.2 Fast rotation of fluid aggregates near $\gamma = \pi/2$

By construction we know that aggregates become more dilute with increasing γ, and become non-cohesive for lateral visual perception $\gamma = \pi/2$. However, slightly below $\gamma = \pi/2$ it is still possible that aggregates are still non-cohesive, as we have found for $\gamma/\pi = 0.48$ in Sec. 3.3, although the structure of the aggregates is somewhat different for particles with almost lateral perception. In Fig. 4.2a we observe snapshots of aggregates in steady state for systems with $\gamma/\pi = 0.40625, 0.44, 0.45$. To verify that the aggregates are indeed in steady state, we obtain the radius of gyration $R_g(t)$ and check this quantity remains constant at longer times $t > 1 \times 10^3\, \tau_{\mathrm{B}}$, see Fig. 4.2b. We find steady state is reached for $\gamma/\pi \leq 0.45$, conversely for larger values R_g grows in time and therefore systems are non-cohesive. From density radial profiles $\rho(r)$, see Fig. 4.2c, we observe that the system is diluted with values below the compact case, $\rho < \rho_c$, and with an interface as large as the aggregate's size. The angular velocity $\omega(r)$ in Fig. 4.2 shows the interface is very large in all cases, for $\gamma/\pi = 0.40625$ the profile monotonously decreases from a maximum at the center; whereas for $\gamma/\pi = 0.44, 0.45$ the profile shows a non-monotonous dependence with a slower center. This is coupled to the activity distribution, as it is found to be mostly homogeneous, except for the center which is found to be passive for $\gamma/\pi = 0.44, 0.45$. For aggregates of size $R > R_c$ the interparticle distances are larger, and therefore the perception of particles near the center become smaller than $q^* = 1$ (recall that $q_i \sim 1/r_{ij}$). We have found the aggregate of particles with $\gamma/\pi \approx 0.4$ shows the fastest rotation at the center. Particles there rotate even faster than the case with $\gamma/\pi = 0.375$ shown in Fig. 4.1c. The reason for such an increase in angular velocity is that for looser aggregates the velocity of the active particles is much less diminished by steric interactions with neighbouring particles, contrary to the case when the system is compact, where particles movement is limited by close-packing.

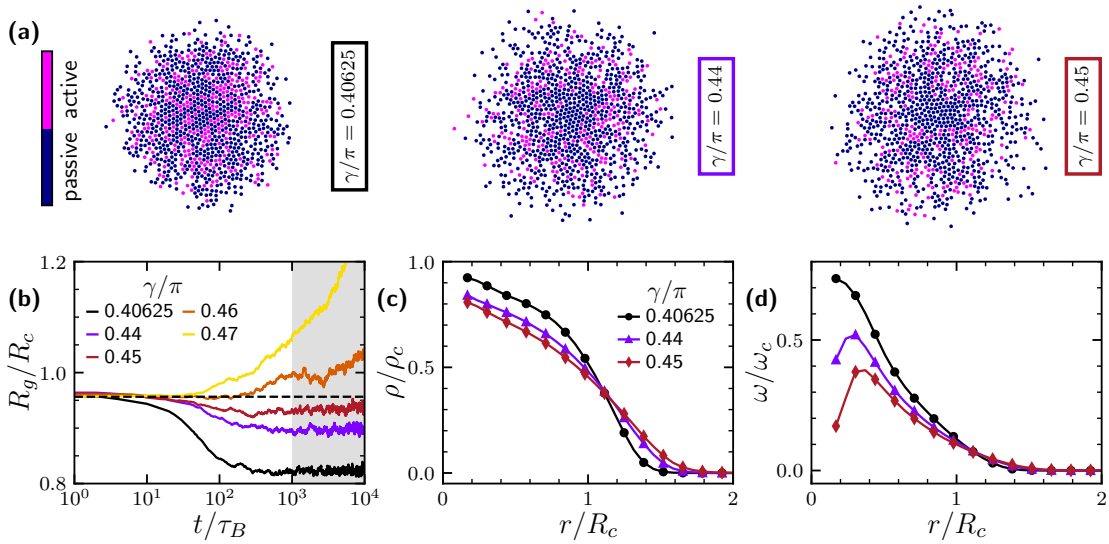

Figure 4.2: *Aggregates with near lateral perception* $\gamma \lesssim \pi/2$. (a) Configuration snapshots for systems in steady state with for $\gamma/\pi = 0.40625, 0.44, 0.45$. (b) Time evolution of the radius of gyration R_g. Shaded region $t/\tau_B > 1 \times 10^3$ corresponds to the steady state for the collapse cases. (c) Density radial profiles. (d) Angular velocity radial profiles.

4.1.3 Activity distribution dependence on perception threshold q^*

Now we describe behaviors obtained for different values of q^* at fixed misalignment angle $\gamma = \pi/4$. Snapshots of collapsed aggregates in steady state are shown in Fig. 4.3a. We observe that the activity distribution changes significantly with q^*. Such behaviors are quantified by density radial profiles, see Fig. 4.3b. For $q^* = 0.3$ the system is less compact and composed mainly of active particles with passives only in the outer layer. Here, $\rho(r)$ shows step-like behavior with a bulk density of $\rho \approx 1.5\rho_0$, which drops at the interface starting from $r = 15\sigma$ and vanishing at $r = 25\sigma$. When considering only the distribution of active particles, $\rho(r)$ is also step-like, and for the passives it is non-monotonous with a maximum around $r \approx 17\sigma$ and vanishing both at $r = 0$ and $r > 25\sigma$. For $q^* = 0.7$, the activity distribution is similar as for $q^* = 0.3$, however in this case the aggregate is compact instead of dilute, with bulk density near $\rho \approx 2\rho_0$. For $q^* = 1$ we observe the aggregate is compact with an homogeneous activity distribution, as already discussed for $\gamma = \pi/4$ in Fig. 4.1a-b; for comparison, same data is shown again in Fig. 4.3. For $q^* = 1.2$, the aggregate is also compact, but the activity distribution is inhomogeneous, mainly composed by passive particles with actives only

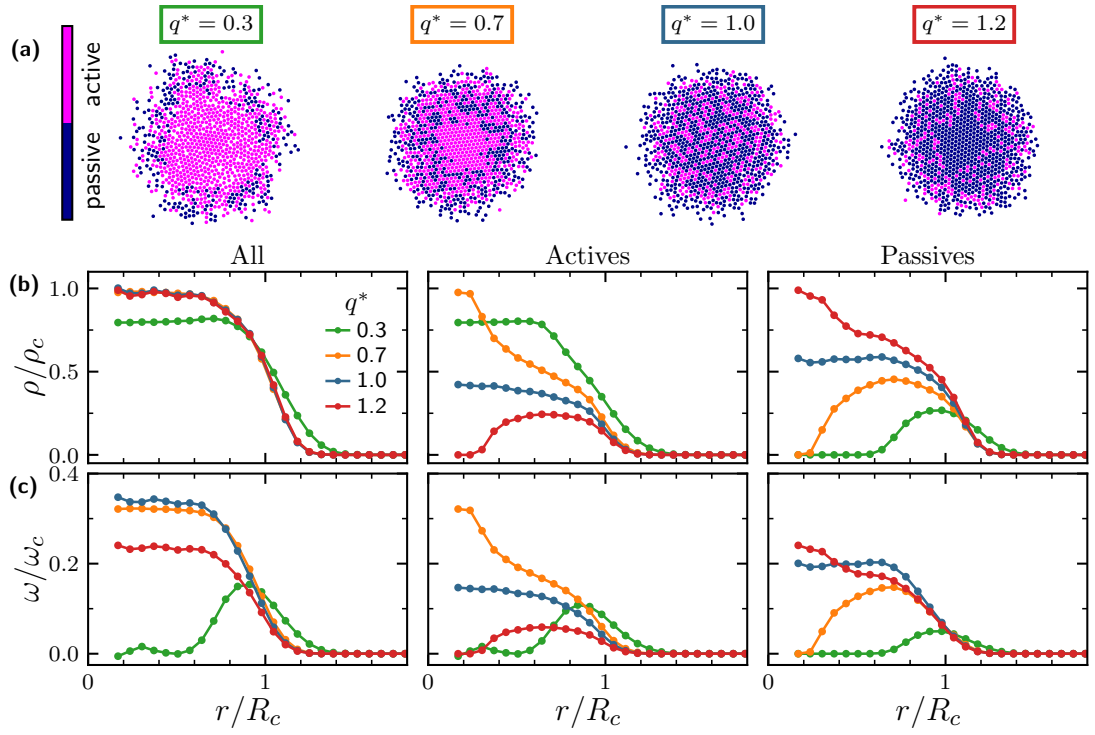

Figure 4.3: *Radial profiles of the aggregate's properties with misalignment angle* $\gamma = \pi/4$. (a) Snapshots aggregates in steady state for different values of q^*. (b-e) Radial profiles for the aggregate's properties.

in the outer layer. Again, this is reflected in the form of $\rho(r)$, which is step-like with bulk density $\rho \approx 2\rho_0$ when considering all particles, it is non-monotonous for active particles, and decreasing for passives.

Furthermore, we find that the motility distribution, as modified via the perception threshold, has a significant impact on the aggregate's angular velocity, as observed in Fig. 4.3c. We observe that the form of $\omega(r)$ depends on the perception threshold q^*. The diluted aggregate found at $q^* = 0.3$ display rotations only in the outer layer at $r = 15\sigma$ with $\omega \approx 0.3\omega_c$. The center of this aggregate does not rotate, as there particles are all active and move isotropically. In the center, at any orientation $\boldsymbol{e}_i$ a particle i perceives enough neighbours to become active, such that misalignment does not play a role and no-average motion is induced. This can be seen from perception radial profiles $q(r) = P(r)/P_c$ (see Eq. (3.2) and Sec. 3.10) for particles within an aggregate of size R_c, see Fig. 4.4a. We observe that for all orientations $\widetilde{\phi} = -\pi/2, -\pi/4, \pi/4, \pi/2$ particles at $r/R_c < 0.8$ surpass $q^* = 0.3$ and thus they are active. At $r/R_c > 0.8$ Anti-oriented particles, with $\widetilde{\phi} = \pi/2$, have perception $q < 0.3$ and thus are passive. Therefore, there is an imbalance of

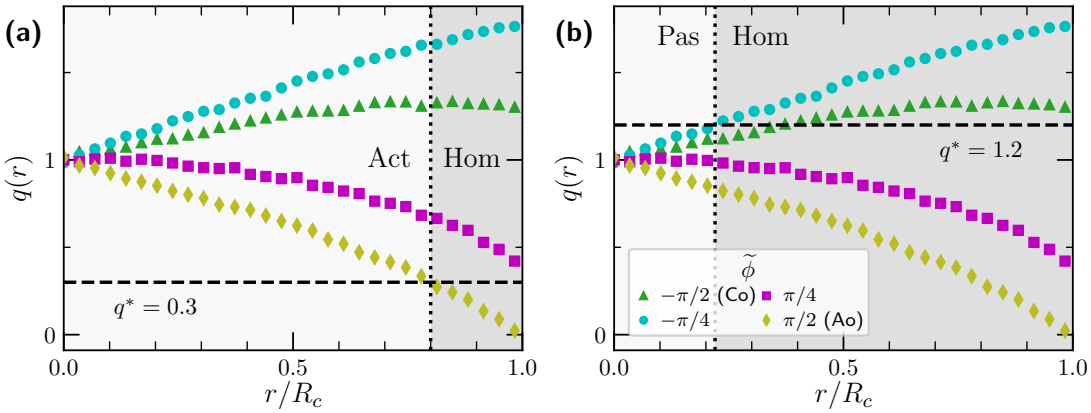

Figure 4.4: *Activity distribution according to perception.* Perception radial profiles of a steady state cohesive aggregate of size R_c with shaded regions indicating active (Act), passive (Pas), and homogeneous (Hom) motility distributions. Perception threshold is set to (a) $q^* = 0.3$, and (b) $q^* = 1.2$.

passive anti-oriented particles, against active Co-oriented ones rotating around in the outer layer. Considering all particles for larger values $q^* \geq 0.7$, $\omega(r)$ shows that rotations occur homogeneously in the whole cluster, i.e. the cluster displays a rigid-body rotation. The form of $\omega(r)$ for actives and passives is coupled to the behaviors of $\rho(r)$, e.g. for $q^* = 0.7, 1.2$ profiles $\omega(r)$ are non-monotonous, only because $\rho(r)$ is also non-monotonous. For the larger perception threshold value $q^* = 1.2$ the cluster displays a rigid-body rotation with a significant angular velocity value in the bulk, $\omega \approx 0.6\omega_c$, despite the smaller amount of actives driving the cluster in the outer layer. See Fig. 4.4b. The observed rigid-body rotation is a consequence of steric interactions, since in close-packing the active particles in the outer layer are able to drag the passive ones to move along with them, resulting in a constant angular velocity in the bulk of the aggregate, decaying towards the boundary. The effect of the misalignment angle of selecting In- and Co-oriented particles as actives, and Out- and Anti-oriented ones as passives is still present when we change the threshold q^*. This behavior is reflected in radial profiles for the polarization components similar to those in Fig. 4.1d-e.

4.1.4 Aggregate properties with varying Péclet number P_e

Now we study the effect in the aggregate's structural properties when changing the rotational Péclet number

$$P_e = \frac{v_0}{\sigma D_r}, \tag{4.2}$$

where v_0 is the self-propulsion velocity and D_r the rotational diffusion coefficient. For this purpose, we keep fixed $q^* = 1$, $\gamma = \pi/4$ and $v_0 = 40\sigma^2/D_t$, and vary the rotational diffusion coefficient. The rotational Péclet number is an important quantity, as the motility of particles is highly dependent on the self-propulsion orientation $\boldsymbol{e}$, which also change the orientation of the vision cone. Therefore, we expect the dynamics to be different with changing rotational diffusion D_r. We find that in steady state, the aggregates are more compact for smaller Péclet numbers P_e, whereas they are more dilute for larger P_e , see Fig. 4.5a-b. This behavior is due to the longer persistence length of active particles with higher P_e. As observed in Fig. 4.5c-d, particles at low P_e display a more activity intermittent trajectory, constantly switching motility between active and passive. On the other hand, particles with high P_e display trajectories which remain more time as either passive or active. When they are passive they have more time to diffuse out, and when they are active they can deviate their direction away from the accumulation of particles, as long as they still perceive enough neighbors.

This behavior is quantified by radial profiles for the density $\rho(r)$, see Fig. 4.6a-b. Here we observe that systems at lower P_e show an aggregate with a sharper interface, compared to the broader one shown in systems at higher P_e. In all cases the activity distribution remains homogeneous, and the number of passives slightly increases with higher P_e. In the center the density reaches values of $\rho \approx 2\rho_0$. The increase of the interface size with higher P_e is somewhat unexpected if one compares with motility-induced phase separation, which is known to display more clustering with increasing values of the Péclet number. Instead, here we have

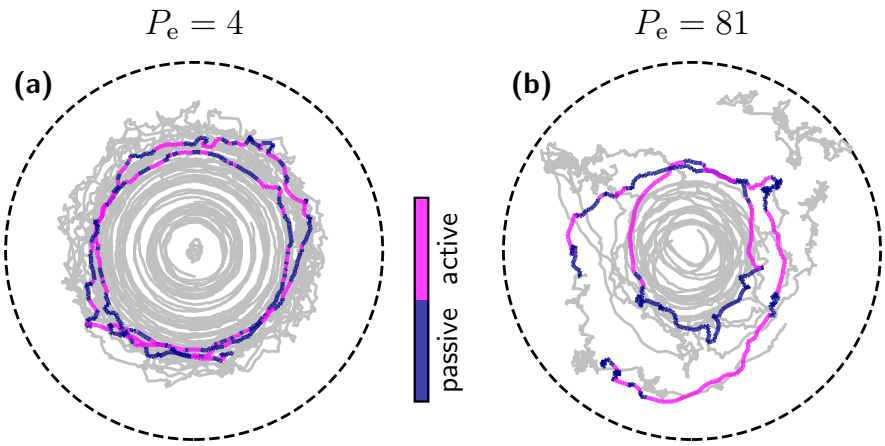

Figure 4.5: *Systems at low and high Péclet numbers* P_e. Typical trajectories of particles at (a) $P_\mathrm{e} = 4$, and (b) $P_\mathrm{e} = 81$. Silver lines show 20 randomly selected trajectories. Color coded trajectories indicate motility.

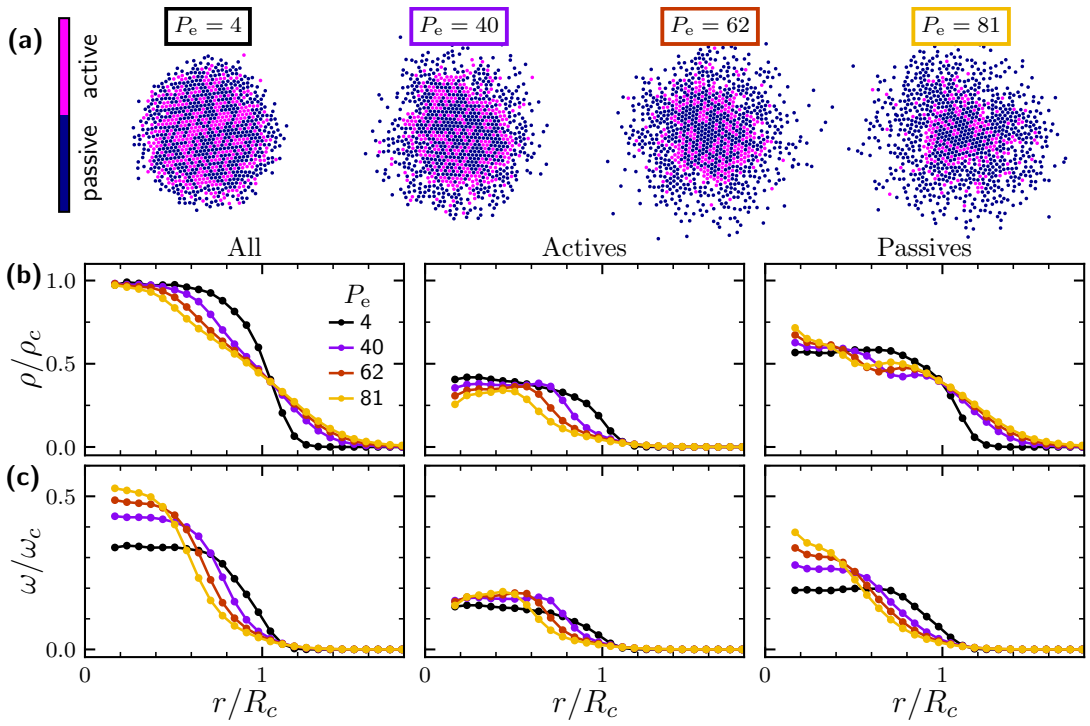

Figure 4.6: *Cohesion enhanced by decreasing Péclet number.* A system of particles with low $P_e = 1$ (a), and high $P_e = 160$ (b). Density profiles $\rho(r)$ for various values of P_e. The corresponding angular velocity profiles $\omega(r)$ are shown as dashed lines with values given by the right-axis.

that a more compact cluster is obtained for smaller values of P_e. Furthermore, we also obtain angular velocity radial profiles $\omega(r)$. We observe that in the bulk, the angular velocity increases with P_e, see Fig. 4.6c. Furthermore, the interface of $\omega(r)$ also increases with P_e. A rigid body rotation is only observed near the center where the system remains in close-packing.

4.2 Continuum description of steady state rotating aggregates

In this section we consider a continuum description of the system and employ conservation equations to derive analytical expressions for the aggregate's properties in steady-state, like the bulk density ρ_b, radius R, and polarization $\boldsymbol{p}$. We consider coarsed-grained spatial coordinates, i.e. the system is subdivided into small finite square cells of length l larger than the particle size but much smaller

than the box length, $\sigma < l \ll L$, then coordinates $\boldsymbol{r}_k$ in this case refer to the position of the center of the k-th cell, which in general can contain none or several particles. For example, we can define a local number density $\rho_M(\boldsymbol{r}_k, t) = M/l^2$, where $M \leq N$ refers to the number of particles found within the k-th cell at position $\boldsymbol{r}_k$ at time t. The continuum limit then corresponds to the case where the coarsed-grained cells and particles are infinitesimally small, i.e. $l/L \to 0$ and $\sigma/l \to 0$.

As already introduced in Sec. 3.1, self-propelled particles have two degrees of freedom, the position $\boldsymbol{r}$ and the angle ϕ parametrizing the orientation vector as $\boldsymbol{e}(\phi) = (\cos\phi, \sin\phi)^T$, see Fig. 4.7a. We define the 1-body probability density $\psi(\phi, \boldsymbol{r}, t)$ as the probability of finding one particle within the parameter space volume element $d\boldsymbol{r}d\phi$ at time t. The local number density can be obtained from $\psi(\phi, \boldsymbol{r}, t)$ by integrating over ϕ, i.e. averaging over particle orientations located at position $\boldsymbol{r}$ at time t

$$\rho(\boldsymbol{r}, t) = \int_{-\pi}^{\pi} d\phi \psi(\phi, \boldsymbol{r}, t). \tag{4.3}$$

Local polarization is given by the average orientation field, $\boldsymbol{p}(\boldsymbol{r}, t) = \langle \boldsymbol{e}(\boldsymbol{r}, t) \rangle$, where the average $\langle \cdots \rangle$ corresponds to an integral over the angle ϕ, written explicitly

$$\boldsymbol{p}(\boldsymbol{r}, t) = \int_{-\pi}^{\pi} d\phi \boldsymbol{e}(\phi, \boldsymbol{r}, t) \psi(\phi, \boldsymbol{r}, t), \tag{4.4}$$

where $\boldsymbol{e}(\phi, \boldsymbol{r}, t) = \cos\phi \hat{\boldsymbol{x}} + \sin\phi \hat{\boldsymbol{y}}$ is the local orientation vector field. Knowing the probability density $\psi(\phi, \boldsymbol{r}, t)$ would give us the full dynamics of the continuum properties by plugging it in definitions Eq. (4.3) and Eq. (4.4) and performing the integrals. However, $\psi(\phi, \boldsymbol{r}, t)$ is not known, and in general it is a complicated expression for a system of interacting particles. Since we are interested in steady state properties, we can directly obtain expressions for $\rho(\boldsymbol{r})$ and $\boldsymbol{p}(\boldsymbol{r})$ by employing known steady state conservation equations together with adequate boundary conditions.

4.2.1 Polarization of the active particles

As we have found in particle-based numerical simulations, systems of Brownian particles with switching motility and misaligned visual perception aggregate into compact cohesive structures with well-defined bulk density ρ_b and radius R. Here the system is homogeneous within the bulk, and isotropic in orientations $\boldsymbol{e}$ (dynamics of ϕ is given only by rotational diffusion with coefficient D_r). In this case, from integral Eq. (4.3) we have that the steady state probability density for $r < R$ is constant

$$\psi(\phi, \boldsymbol{r}, t) = \frac{\rho_b}{2\pi} \Theta\left(1 - \frac{r}{R}\right), \tag{4.5}$$

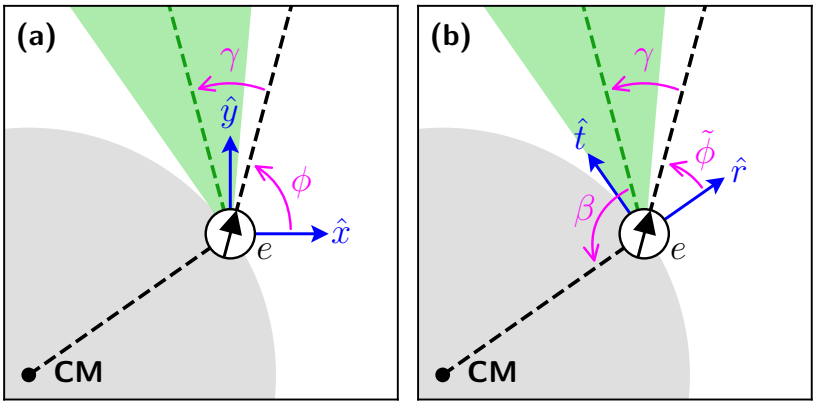

Figure 4.7: *Transformation of the orientation angle ϕ.* Particle with self-propulsion orientation $\boldsymbol{e}$ and vision cone misalignment angle γ located at $r = R$. The orientation vector $\boldsymbol{e}$ is parametrized by: (a) angle ϕ between vectors $\hat{\boldsymbol{x}}$ and $\boldsymbol{e}$, and (b) angle $\widetilde{\phi}$ between vectors $\hat{\boldsymbol{r}}$ and $\boldsymbol{e}$. The vision cone angle $\beta = \gamma + \widetilde{\phi} - \pi$ corresponds to the angle between $-\hat{\boldsymbol{r}}$ and the vision cone orientation $\boldsymbol{c} = [\cos(\widetilde{\phi} + \gamma), \sin(\widetilde{\phi} + \gamma)]^T$ which defines the vision cone axis of symmetry.

where $\Theta(\cdot)$ is the Heaviside step function. Furthermore, due to isotropic orientations $\boldsymbol{e}$, the integral in Eq. (4.4) vanishes and the polarization is $\boldsymbol{p} = 0$ everywhere. However, the quantity of interest is not the global polarization but how this is distributed between active and passive particles, both in the radial and tangential components of the polarization field, i.e. $p_r = \hat{\boldsymbol{r}} \cdot \boldsymbol{p}$ and $p_t = \hat{\boldsymbol{t}} \cdot \boldsymbol{p}$, where $\hat{\boldsymbol{r}}$ and $\hat{\boldsymbol{t}}$ refer to radial and tangential unitary vectors, see Fig. 4.7b. The polarization vector field can then be linearly decomposed as

$$\boldsymbol{p} = \boldsymbol{p}^a + \boldsymbol{p}^p = \left(p_r^a \hat{\boldsymbol{r}} + p_t^a \hat{\boldsymbol{t}}\right) + \left(p_r^p \hat{\boldsymbol{r}} + p_t^p \hat{\boldsymbol{t}}\right), \tag{4.6}$$

where the superscripts a and p refer to the active and passive contributions, respectively. At the interface $r = R$, the polarization components of the active particles can be calculated by plugging Eq. (4.5) in definition (4.4), giving

$$p_r^a|_{r=R} = -\int_{-\pi}^{\pi} d\phi \hat{\boldsymbol{r}} \cdot \hat{\boldsymbol{e}}^a(\phi) \frac{\rho_b}{2\pi}, \tag{4.7a}$$

$$p_t^a|_{r=R} = \int_{-\pi}^{\pi} d\phi \hat{\boldsymbol{t}} \cdot \hat{\boldsymbol{e}}^a(\phi) \frac{\rho_b}{2\pi}. \tag{4.7b}$$

The orientation field $\boldsymbol{e}^a$ as a function of the orientation angle ϕ is not known, therefore we cannot directly perform the integrals in Eqs. (4.7). To find a more suitable expression, first we change variables to parametrize $\boldsymbol{e}^a$ as a function of

the transformed angle $\tilde{\phi}$, defined earlier in Eq. (3.5) as the angle between $\boldsymbol{e}$ and the radial vector $\hat{\boldsymbol{r}}$, see Fig. 4.7b. We consider a second change of variables, from $\tilde{\phi}$ to an angle β defined as the angle between $-\hat{\boldsymbol{r}}$ and the vision cone orientation vector $\boldsymbol{c} = [\cos(\tilde{\phi}+\gamma), \sin(\tilde{\phi}+\gamma)]^T$, see Fig. 4.7b. Angle β is given by

$$\beta = \tilde{\phi} + \gamma - \pi. \tag{4.8}$$

In this representation we have that a particle is active when its orientation β is within range $-\beta^* < \beta < \beta^*$, see Fig. 4.8a. Conversely, a particle is passive when $\beta > \beta^*$ or $\beta < -\beta^*$, see Fig. 4.8b. The perception angular profile $q(\beta)$ is bell shaped, see Fig. 4.8c, ensuring that only particles with β within the range $(-\beta^*, \beta^*)$ perceive a larger number of neighbors, so the perception threshold q^* is surpassed. In other words, the angular threshold β^* is a monotonously decreasing function of the perception threshold $\beta^*(q^*)$. Therefore, a given threshold q^*

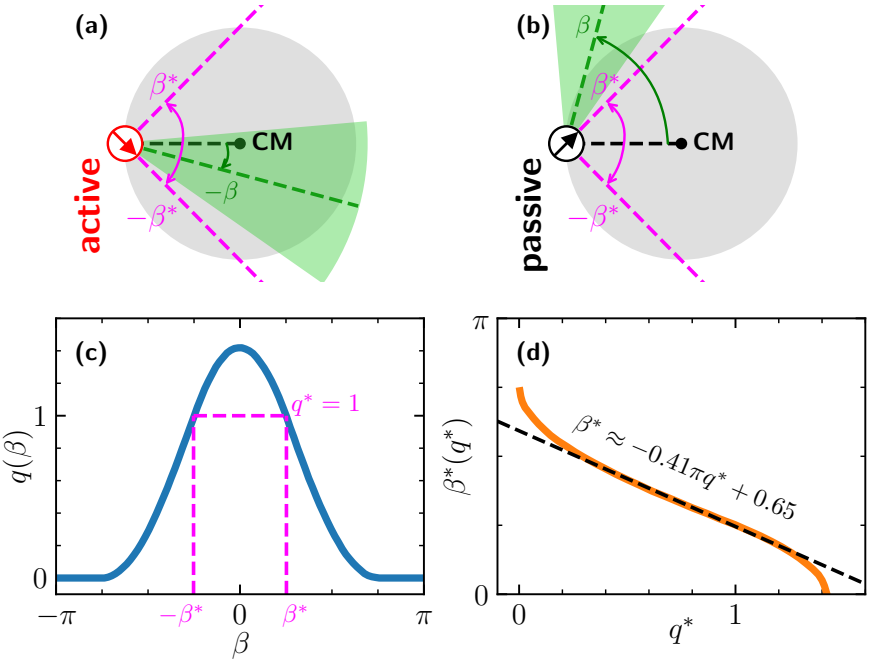

Figure 4.8: *Angle threshold* β^*. A particle located at $r = R$ from the aggregate's center $\boldsymbol{r}_{\rm cm}$, and oriented with vision cone angle β. A particle with orientation (a) $\beta < \beta^*$ is active, whereas with (b) $\beta > \beta^*$ is passive. (c) Perception angular profile $q(\beta)$. Horizontal dashed line indicates the threshold value $q^* = 1$. Positive and negative values of β^* are indicated with vertical dashed lines. (d) Positive branch of the angle threshold β^*, obtained by inverting $q(\beta)$. Dashed line is a linear approximation valid for a broad range of q^*.

uniquely determines the range $(-\beta^*, \beta^*)$. Fig. 4.8d shows that for a large range of $q^* \in (0.2, 1.2)$, the linear approximation $\beta^*(q^*) \approx -0.41q^* + 0.65$ is a very reasonable estimation.

Employing transformations Eq. (3.5) and Eq. (4.8), the polarization components in Eqs.(4.7) are easily computed

$$p_r^a|_{r=R} = -\int_{-\beta^*}^{\beta^*} d\beta \cos(\pi + \beta - \gamma)\frac{\rho_b}{2\pi} = \frac{\rho_b}{\pi}\sin\beta^*\cos\gamma, \tag{4.9a}$$

$$p_t^a|_{r=R} = \int_{-\beta^*}^{\beta^*} d\beta \sin(\pi + \beta - \gamma)\frac{\rho_b}{2\pi} = -\frac{\rho_b}{\pi}\sin\beta^*\sin\gamma. \tag{4.9b}$$

4.2.2 Conservation equations

Now we derive expressions for the aggregate's bulk density ρ_b and radius R from steady state conservation equations. The transport of particles for the cohesive aggregates considered here is given only by thermal diffusion D_t and particle self-propulsion v_0, then the particle current is $\boldsymbol{J} = D_t\nabla\rho - v_0\boldsymbol{p}$. In steady state, the radial flux $\hat{\boldsymbol{r}}\cdot\boldsymbol{J}$ at the interface $r = R$ is conserved, therefore

$$\left[D_t\partial_r\rho - v_0 p_r^a\right]_{r=R} = 0. \tag{4.10}$$

This conservation equation shows that the flux of particles leaving the cluster due to thermal diffusion (first term of the equation), is balanced out by the flux of particles that actively join the aggregate (second term of the equation). To compute the first term above, we employ a step function for the density radial profile

$$\rho(r) = \rho_b\Theta\left(1 - \frac{r}{R}\right), \tag{4.11}$$

which follows from plugging Eq. (4.5) in Eq. (4.3). It is a reasonable approximation for our numerical results in steady state, as we have seen from density radial profiles in Fig. 4.1 and in Fig. 4.3. Plugging this expression for the density into the no-flux condition Eq. (4.10), we obtain

$$\frac{\rho_b}{R} = \frac{v_0}{D_t}p_r^a, \tag{4.12}$$

where we have used that $\partial_x\Theta(x) = \delta(x)$.

Another steady state conserved quantity is given by the number density conservation $\int d^2\boldsymbol{r}\rho(\boldsymbol{r}) = \rho_0 A$ where A is the area covered by the particles in the

initial configuration. For the step function Eq. (4.11), this conservation equation yields

$$\rho_b R^2 = \rho_0 R_0^2. \tag{4.13}$$

Eq. (4.13) can be solved together with Eq. (4.9) and Eq. (4.12), giving expressions for the aggregate's bulk density ρ_b and radius R as functions of the misalignment angle γ,

$$R(\gamma) = \frac{D_t}{v_0} \frac{\pi}{\sin \beta^*} \frac{1}{\cos \gamma}. \tag{4.14}$$

4.3 Aggregate size R and bulk density ρ_b

As studied in Sec. 4.1, the density radial profiles $\rho(r)$ of circular aggregates display a step-like behavior with constant bulk density ρ_b, and a soft decay at the aggregate's boundary $r = R$. Such behavior can be approximated by the function

$$\rho(r) = \frac{\rho_b}{2} + \frac{\rho_b}{2} \tanh\left(\frac{R - r}{\xi}\right) \tag{4.15}$$

where δ corresponds to the width of the aggregate's interface. Employing this function we fit density radial profiles in steady sate, from which we obtain the coefficients R, ρ_b and ξ for various values of the perception threshold q^* and misalignment angle γ. The results for R and ρ_b are shown in Fig. 4.9. Normalization parameters employed are the density $\rho_c \approx 0.9\sigma^{-2}$, and size $R_c \approx 18.5\sigma$ corresponding to a compact aggregate, i.e. the size and density of an aggregate in hexagonal close-packing. In Fig. 4.9a, we observe that at fixed $q^* = 1$ and increasing γ, the aggregate's remains reasonably compact with $R \approx R_c$, and density $\rho_b \approx \rho_c$. The most significant change in this case, is an increase in the interface width δ, which we discuss in more depth in Sec. 4.4. In Fig. 4.9b, we observe that at fixed $\gamma/\pi = 0.25$ aggregates are more dilute for smaller q^* and compact for larger values. Measured numerical data for $\rho(r)$ nicely fit Eq. (4.15). The extracted parameters R and ρ_b are shown in Fig. 4.9c-d for various values of q^* and γ. Data points approaching $\gamma \approx \pi/2$, where $R > 1.5R_c$ are not shown, as we find in those cases the system is non-cohesive and therefore does not reach steady state, see Sec. 3.3. In Fig. 4.9c-d we observe that R decreases with q^* and monotonously increases with γ, diverging at $\gamma = \pi/2$. For the bulk density, we observe a clear behavior $\rho_b \sim R^{-1}$, which is in perfect agreement with the density conservation Eq. (4.13). At $q^* = 1$ and $\gamma < \pi/4$, the minimum size and maximum bulk density are obtained, corresponding to that of a closed-packed configuration, and therefore R and ρ_b display a plateau in that limit. To compare

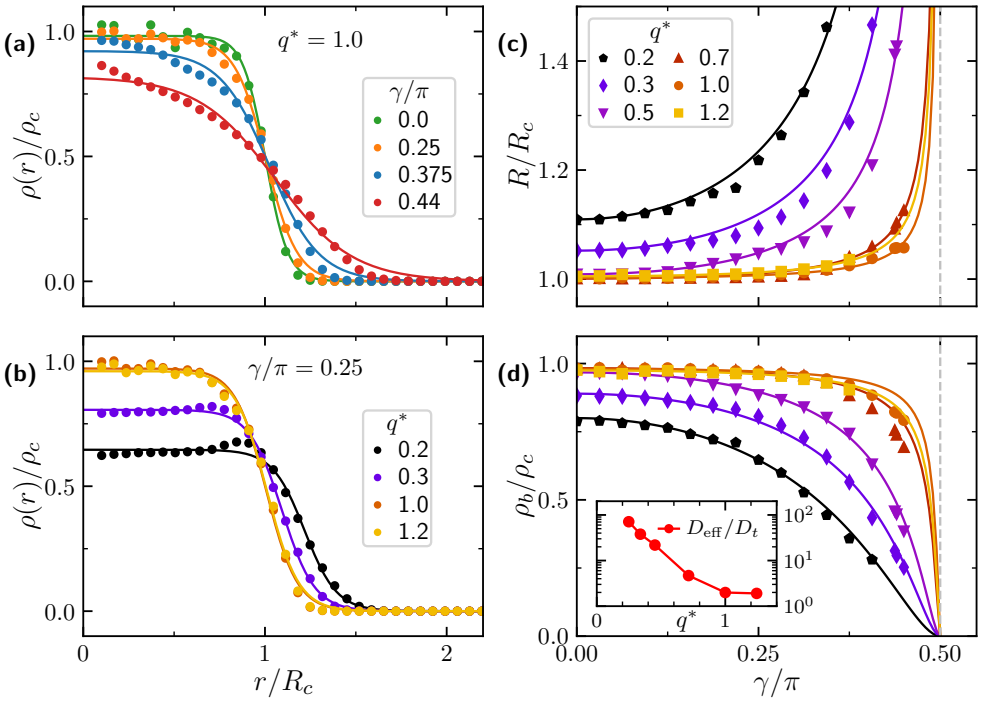

Figure 4.9: *Behavior of aggregates in steady state at given γ and q^*.* Density radial profiles (a) at fixed $q^* = 1$, and (b) at fixed $\gamma = \pi/4$. Solid lines correspond to the fitting function Eq. (4.15). Extracted fit parameters, namely (c) aggregate's size R, and (d) bulk density ρ_b. Solid lines correspond to analytic expression Eq. (4.16) with the effective diffusion $D_{\rm eff}$ as a fit parameter. Inset shows obtained values of $D_{\rm eff}$.

our numerical results for R and ρ_b with analytical expressions derived in previous section, we rewrite Eq. (4.14) as

$$R(\gamma) = \frac{D_{\rm eff}}{v_0}\frac{\pi}{\sin\beta^*}\left[\frac{1}{\cos\gamma} - 1\right] + R_c \tag{4.16}$$

such that the term within angular brackets vanishes at $\gamma = 0$, and $R(0) = R_c$. We impose this boundary condition as the expression derived for R in Eq. (4.14) does not take into account steric interactions, giving non-physical small aggregates (where particles would overlap) at smaller values of γ. Furthermore, we have introduced the effective diffusion $D_{\rm eff}$, which replaces D_t in Eq. (4.11). This serves as a fit parameter accounting for the active diffusivity found at lower values of q^*. In fact, $D_{\rm eff}$ does not depend on the misalignment angle γ as the aggregate's activity distribution is only affected by q^*, see Sec. 4.1. The calculated effective

diffusivity is shown in the inset of Fig. 4.9d, for which we find theory curves nicely agreeing with our numerical data as shown in Fig. 4.9c-d. We observe D_{eff} monotonously decays with q^*, from $D_{\text{eff}} \approx 10^2 D_t$ at $q^* = 0.2$, to $D_{\text{eff}} \approx D_t$ at $q^* = 1$ where there is no activity in the center of the aggregates, instead there is only thermal diffusivity occurring for passive particles in the outer layer.

4.4 Interface width ξ

Apart from bulk properties, the interface width was found to change significantly with the misalignment angle γ. By fitting the data shown in Fig. 4.9a,b with Eq. (4.15), besides the fit parameters ρ_b and R, we also obtain the interface width ξ for each radial profile. To better visualize the behavior of ξ in the density radial profiles, we normalize $\rho(r)$ by using the measured bulk density ρ_b, and shift the center by using the measured aggregate size R. Such that $\rho(r)/\rho_b = 1$ in the bulk, and $r - R = 0$ is the new origin. Rescaled density profiles are shown in Fig. 4.10a-b. For $q^* = 1$ and varying γ, we observe that the center of all curves lie at $r = R$, the curves decrease from a maximum at $\rho = \rho_b$, vanishing at large r. In this representation, it is clear that increasing γ broadens the interface width ξ. On the other hand, at $\gamma/\pi = 0.25$ and varying q^*, see Fig. 4.10c, we observe that

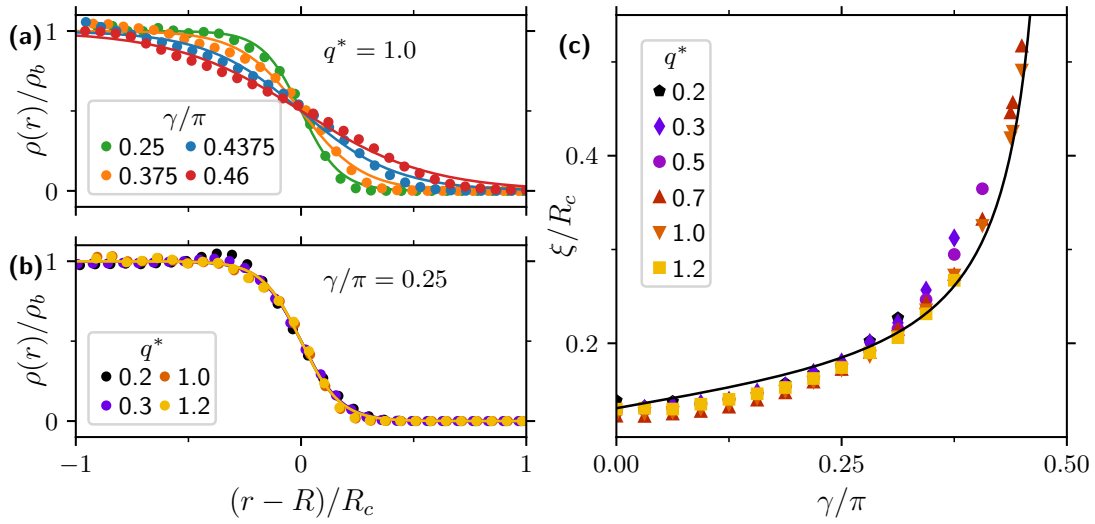

Figure 4.10: *Interface width of the aggregates.* Rescaled density radial profiles (a) at fixed $q^* = 1$, and (b) at fixed $\gamma = \pi/4$. (c) Interface width ξ as a function of the misalignment angle γ at perception threshold q^*. Solid line corresponds to Eq. (4.17).

data for all q^* collapse into the same curve, showing that the interface width ξ is unaffected by the perception threshold. Values of ξ for different γ and q^* are shown in Fig. 4.10c. We observe a divergent growth of ξ with increasing misalignment angle γ, starting from a minimum at $\gamma = 0$ with value $\xi(0) \approx 0.1R_c$ and blowing up at $\gamma = \pi/2$. Moreover, we observe all the data points collapse into a single curve, independent of q^*. Taking into account such behavior and boundary conditions, we propose the phenomenological function

$$\xi(\gamma) = \xi(0) + \tan(\gamma), \tag{4.17}$$

which we find nicely fits our numerical data.

We know the effect of varying q^* is to change the activity distribution of the aggregate. The change in activity occurs in the aggregate's center, however we have found that the outer layer remains homogeneous in all cases. This suggests that the interface width is independent of changes of activity distribution in the center. The effect of the misalignment angle γ on the aggregate can be understood as imposing an effective attractive force between the particles and the aggregate's center, which should be given by the active velocity $v_r \sim v_0 p_r^a$. Furthermore, an effective tangential driving force (a torque) is also imposed, which should be given by $v_t \sim v_0 p_t^a$. From Eqs. 4.9, we have that at the interface the ratio $v_r/v_t \sim \tan\gamma$ which is the second term in Eq. (4.17), this indicates that indeed at the interface effective attraction diminishes with γ, whereas net torque increases. This translates into broader interface width ξ with increasing γ as we observe in our numerical results.

4.5 Bulk angular velocity ω_b

Rigid-body rotations display step-like angular velocity radial profiles $\omega(r)$. In those cases, similar to what we did for $\rho(r)$, we can fit the measured steady state angular velocity with a function similar to Eq. (4.15) which now reads

$$\omega(r) = \frac{\omega_b}{2} + \frac{\omega_b}{2} \tanh\left(\frac{R' - r}{\xi'}\right), \tag{4.18}$$

where ω_b is the bulk angular velocity, R' the profile's size, and ξ' the profile's interface width [1]. Fitting curves at $q^* = 1$ and $\gamma/\pi \leq 0.375$ are shown in Fig. 4.11a. In those cases, the aggregate performs a rigid-body rotation and therefore $\omega(r)$ is step-like and our data nicely fits Eq. (4.18). This holds for a large range of

[1] In general, R' and ξ' do not necessarily correspond to R and ξ measured for $\rho(r)$, which are the actual aggregate's size and interface width.

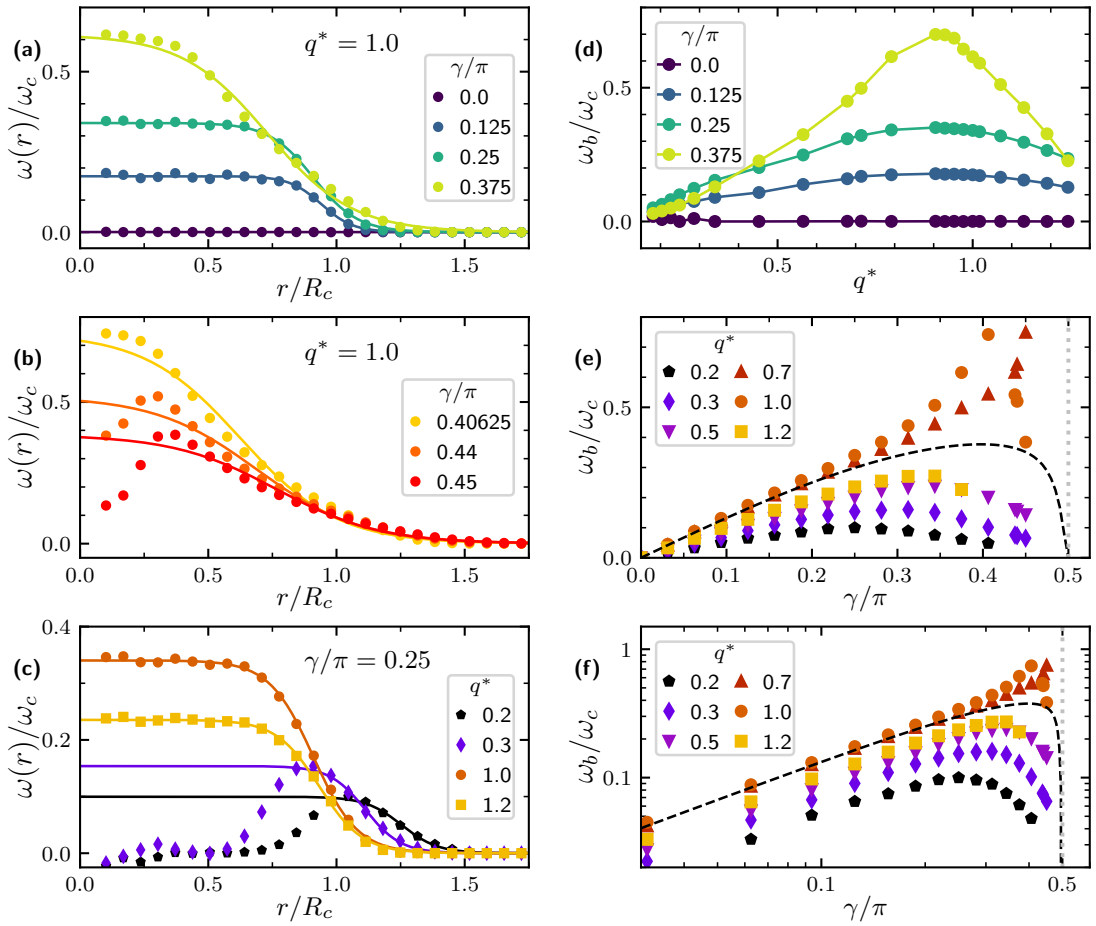

Figure 4.11: *Steady state angular velocity.* Angular velocity radial profiles (a) at $q^* = 1$ and $\gamma/\pi \leq 0.375$, (b) at $q^* = 1$ and $\gamma \geq 0.4$, and (c) at fixed $\gamma = \pi/4$ and $q^* = 0.2$–1.2. Bulk angular velocity ω_b (d) at fixed γ, (e) at fixed q^* in linear scale, and (f) at fixed q^* in logarithmic scale. Solid line in (d-e) corresponds to the theory prediction for $q^* = 1$ in Eq. (4.20).

parameters namely for not too large misalignment angle or too small perception threshold. In the totally aligned case $\gamma = 0$, the aggregate does not rotate. Increasing γ we observe the bulk angular velocity ω_b also increases. Cases with very large γ, i.e. near lateral misalignment $\gamma \lesssim \pi/2$ are shown in Fig. 4.11b. There, profiles $\omega(r)$ show a very broad interface, which eventually become non-monotonous. To account for such behavior when fitting Eq. (4.18), we consider only data points with $r > r_{\max}$, where $r_{\max}$ is the radial distance for which we find the maximum value of the angular velocity $\omega_{\max}$. In this way, we obtain that the maximum angular velocity $\omega_{\max} = \omega_b$ decreases as the misalignment

angle approaches $\gamma = \pi/2$. Aggregates with large $\gamma/\pi \lesssim 0.5$ correspond to fast rotating aggregates which are loose but still cohesive, as discussed in Sec. 4.1.2. Non-monotonous behavior of $\omega(r)$ is also found at small values of q^*, see the profiles for $q^* = 0.2, 0.3$ shown in Fig. 4.11c. There, $\omega(r)$ is maximum near the aggregate's outer-layer. As discussed in Sec. 4.1.3, small q^* leads to aggregates with an active center which does not rotate but has an isotropic displacement field, therefore $\omega(r)$ vanishes close to the center. At $q^* = 1$ where the activity distribution is known to be homogeneous, then $\omega(r)$ is found to be step-like. At $q^* = 1.2$, $\omega(r)$ is also step-like but the value in the bulk diminishes, as in those cases the activity distribution is dominated by passives with a few active particles in the outer layer only.

Obtained values of the bulk angular velocity ω_b for varying q^* and γ are shown in Fig. 4.11d. We observe ω_b shows a clear non-monotonous behavior with q^*, which is due to the aggregates structure transitioning from rotating outer-layer, to homogeneous-activity rigid-body rotation, to passive-center rigid-body rotation. The effect is most dramatic for $\gamma/\pi = 0.375$ shown here. The dependence with γ is shown in Fig. 4.11e-f. To provide an analytic understanding of this result, we employ the following expression for the bulk angular velocity

$$\omega_b = v_0 \frac{p_t^a}{R}. \tag{4.19}$$

The terms p_t^a and R correspond to those obtained in Eq. (4.16) and Eq. (4.9), which are valid only for aggregates displaying rigid-body rotations. For this reason, we do not expect Eq. (4.19) to work in the cases where we have rotations only in the outer layer, which is the case for small q^*. Furthermore, Eq. (4.19) is not expected to work either for cases with almost lateral perception $\gamma/\pi \lesssim 0.5$, where the radial profiles show a very broad interface and are non-monotonous. Note that Eq. (4.19) does not contain any information about the activity distribution of the system. The derived expression for the tangential polarization p_t^a considered only particles at $r = R$, such that the product $v_0 p_t^a$ accounts for the tangential velocity exerted by particles at the interface. This value is the same for all particles of an aggregate displaying rigid-body rotation, but for different structures the tangential velocity is not expected to be the same. For this reason, the validity of Eq. (4.19) is restricted to $q^* \approx 1$ and small values of γ. Plugging Eq. (4.9) into Eq. (4.19) we obtain

$$\omega_b(\gamma) = v_0 \frac{\rho_b}{R} \frac{\sin \beta^*}{\pi} \sin \gamma, \tag{4.20}$$

which is found to be in good agreement between with the data within its range of validity, see Fig. 4.11e. This can be seen in more detail in the logarithmic

representation Fig. 4.11f. Moreover, we find that for small misalignment angle a linear growth $\omega_b \sim \gamma$ holds for other values of q^* as well, emphasizing that the aggregates rotation is driven with velocity $v_0 p_t^a \sim \gamma$ by the tangentially co-oriented active particles.

4.6 Summary

The aggregate's structural properties were studied by means of radial profiles for the density $\rho(r)$ and angular velocity $\omega(r)$, which were found to behave as step-like or non-monotonous functions of r for different values of the control parameters. At $q^* = 1$ increasing the misalignment angle γ, we found that the aggregates interface becomes broad while keeping an almost constant size R and bulk density ρ_b. For values near lateral perception $\gamma/\pi \lesssim 0.5$, we found the interesting case of fast rotating aggregates, which have a broad interface, and they are diluted while still cohesive. These structures showed the largest bulk angular velocity ω_b found, however they also showed a slowly rotating center. At fixed $\gamma = \pi/4$ increasing the perception threshold q^*, we found a dramatic change in the activity distribution of the aggregates. We found smaller values of q^* lead to aggregates composed mainly of active particles with passives only in the outer layer. Such activity distribution translates into more fluid structures that rotate only in the outer layer, as a result of an imbalance in orientation-dependent activity where co-oriented particles are active while anti-oriented ones remain passive. Homogeneous activity distribution is found only for $q^* = 1$, where the aggregates are compact—with a crystalline internal structure—and display rigid-body rotations. Moreover, for values slightly above $q^* = 1$, the aggregate becomes mainly passive with only a few active particles in the outer layer. In this case the aggregates were found to be compact but slow-rotating.

Furthermore, we derived analytic expressions from a continuum description of the aggregate corresponding to a rotating disk of density ρ_b and size R. We obtained a system of equations, which were solved by finding an expression for the polarization of the active particles, which served as a closure in conservation equations for the particle flux and number density. This led to formulas for the size and bulk density at given γ and q^*. Resulting analytic expressions were found to be in good agreement with our numerical results, given fitting parameters accounting for the steric interactions and the activity distribution (not considered in the derivation). Finally, we analyzed the interface width. We found it grows with increasing γ and, unlike clustering in MIPS, we found it grows with decreasing Péclet number P_e. Surprisingly, the perception threshold q^* does not affect the interface, which we found is coupled to the homogeneous activity distribution occurring in the outer later at any value of q^*.

Part II

Mixtures of particles with misaligned visual perception

5 Emergence of directed swarms

To design novel strategies that lead to *motility-induced* emergent collective behavior is one of the current challenges in active matter [4]. One striking case of emergence, is when a system of identical active agents form cohesive macroscopic structures that are able to swarm altogether performing directed motion. Such behavior has been found, e.g. in systems of self-propelled rods [40, 153, 154], and more recently in systems of attractive active Brownian particles [155]. There, particles cooperate to move in sync in a given direction, while penalizing motion in opposite directions. In binary mixtures, collective behavior emerges from cooperation given the different intrinsic properties of each species, e.g. active-passive particles [156–164], colloids with different short-attractive long-repulsive (SALR) potentials [165], with different chiralities [166–172], and with different diffusivities [173]. In recent years, mixtures of particles displaying motility-induced self-organization into directed swarms have been described, e.g. for mixtures of colloids with non-reciprocal phoretic interactions[174], and also for light-activated colloids with aligning interactions [107].

In this chapter we study a binary mixture of particles with misaligned visual perception that self-organizes into a species-separated bean-shaped directed swarm. We quantify dynamical features of the swarms by means of parameters such as the largest cluster size, species separation, fraction of actives, center of mass speed, and mean-squared displacement. For different values of the perception threshold q^*, we find that the system can be either cohesive, dissolve over time leaving a trail of particles, or it can also remain loose non-separated and non-self-propelling. We analyze the shape of the swarms, showing that the misalignment angle γ can be used to control the bean's aperture angle and swarm elongation. To obtain a phase diagram, we systematically vary the parameters (q^*, γ), and also identify the values for which directed swarms are robust and self-propel with maximum speed.

5.1 Formation of directed swarms

Here we study a similar model as in chapters 3 and 4, although in this case not all particles are identical but instead a binary mixture is considered. Dynamics are governed by overdamped Langevin equations of motion (3.1). Particles here perceive neighbors within a restricted cone of vision, see Eq. (3.2), and after surpassing certain perception threshold q^*, they activate with self-propulsion velocity v_0, or remain passive otherwise, see Eq. (3.3). The mixture has N_1 particles with a visual perception that is *misaligned* with respect to the self-propulsion direction by an angle γ_1, and N_2 particles with $\gamma_2 = -\gamma_1$. See Fig. 5.1. In this chapter we consider that the mixture is equimolar $N_1 = N_2$. Other system parameters corresponds to those in Table 3.1.

We perform particle-based numerical simulations of $N_1 = N_2 = 500$ particles which initially are homogeneously distributed within a circle of radius $R_0 = 25\sigma$. The cutoff radius of the vision cone is set to $r_{\text{cut}} = 100\sigma$ and the simulation box is considered to be unbounded. Here, each particle posses a perception threshold of $q^* = 1$ and misalignment angles $\gamma_1 = -\gamma_2 = \pi/4$. The vision cone aperture angle is set to $\alpha = \pi/4$.

We find that at shorter times $t/\tilde{\tau} < 0.4$ where $\tilde{\tau} = 10^4\tau_B$ and $\tau_B = \sigma/v_0$ is the ballistic time, the binary mixture collapses into a single compact aggregate, see Fig. 5.2a. Cohesion is ensured due to orientation-dependent motility, where particles that are in-oriented perceive a larger number of neighbors in the bulk and become active, whereas out-oriented ones do not perceive enough

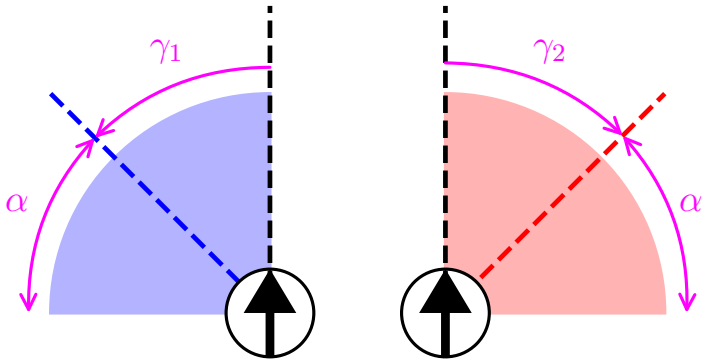

Figure 5.1: *Particle species in the binary mixture.* Species 1 has misalignment angle $\gamma_1 = \pi/4$, and species 2 has $\gamma_2 = -\pi/4$. Both with $\alpha = \pi/4$. The vision cone range is shortened for the sake of clarity.

neighbors and therefore remain passive. This mechanism translates into effective attractions between particles, thus keeping the system cohesive and compact, see Sec. 3.1.1. After collapse, a transient self-sorting process occurs during the time interval $t/\tilde{\tau} = 0.4$–0.8. There, the aggregate's center of mass starts to slowly move. The initial trajectory of a single particle is shown in the zoom-in in Fig. 5.2b, it describes a circling motion occurring during self-sorting. Once the

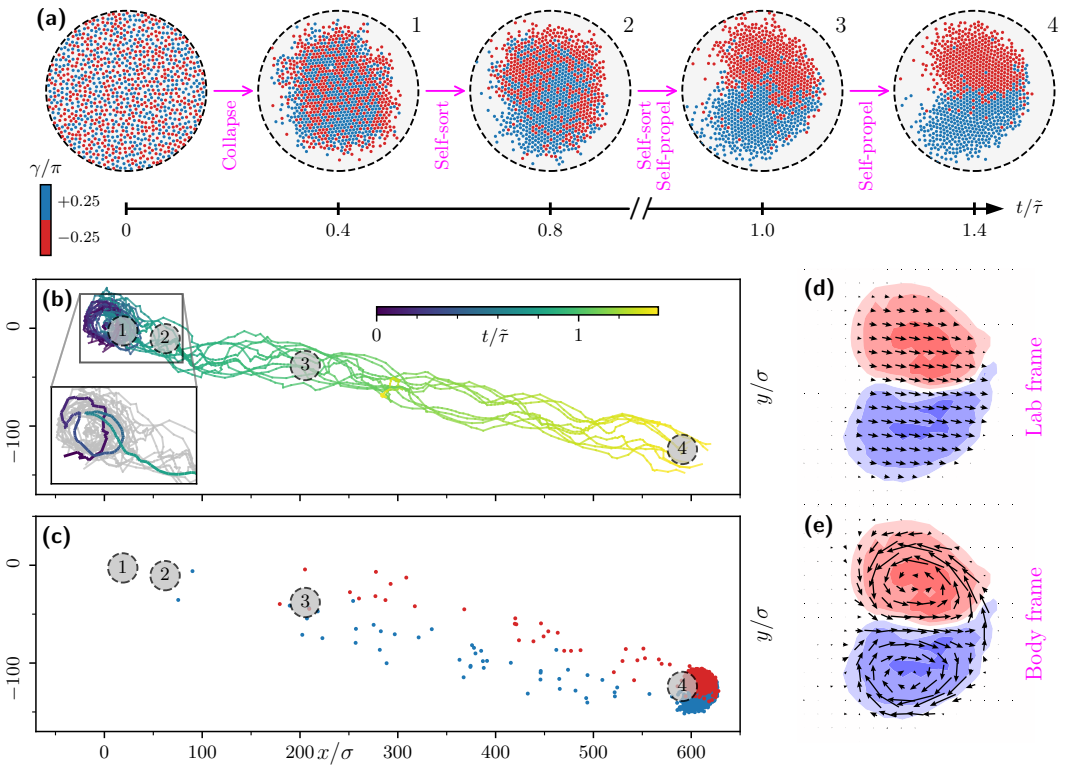

Figure 5.2: *Emergence of a species-separated directed swarm for $\gamma = \pi/4$ and $q^* = 1$.* (a) Particle configuration snapshots showing the system's time evolution. Time is normalized by $\tilde{\tau} = 10^4 \tau_B$ where $\tau_B = \sigma/v_0$ is the ballistic timescale. Dashed circles indicate the size of the initial circular configuration. For clarity, particles outside of this circle are not shown. Snapshots are centered at the center of mass $\boldsymbol{r}_{\mathrm{cm}}$. (b) Trajectories in the lab frame of 10 representative particles, each color-coded by time. Numbers indicate the center of mass positions corresponding to the snapshots in (a). Zoom-in indicates single particle trajectories at $t/\tilde{\tau} < 0.8$. (c) Particle configuration at time $t/\tilde{\tau} = 1.4$. (d-e) Time-averaged coarsed-grained local density (colorized by species) and velocity field (arrows) calculated both in (d) the lab frame, and (e) body frame.

system is reasonably separated at later times $t/\tilde{\tau} = 0.8$–1.4, particle trajectories describe directed straight motion. In this case, as the aggregate persistently self-propels at $t/\tilde{\tau} > 1$, it also dissolves leaving a trail of particles behind, see Fig. 5.2c.

To visualize the dynamical behavior as the swarm self-propels, we coarse-grain both the particle density and the velocity field. For this we subdivide the space into square cells of length $l = 3\sigma$ each. Within each of them, we calculate the local particle density, as well as the average particle velocity, where the velocity of each particle i is calculated from the particle displacements $\boldsymbol{v}_i = [\boldsymbol{r}_i(t+\Delta t) - \boldsymbol{r}_i(t)]/\Delta t$ with the time step set to $\Delta t/\tilde{\tau} = 0.002$. Here Δt is chosen small enough to account only for the instantaneous velocity of the particles, although it is still larger than the ballistic time $\Delta t = 20\tau_B$ to disregard isotropic displacements due to Brownian diffusion. To gain better statistics, we also perform a time-average over configurations in steady-state during a time interval of $\Delta\tau/\tilde{\tau} = 0.02$. In Fig. 5.2d-e, the resulting time-averaged coarsed-grained local density and velocity fields are shown, both in the lab and body frames of reference. We observe the swarm has a bean shape consisting of two lobes, each one corresponding mostly to a single species subdomain. In the lab frame the velocity field shows to be polarized indicating that the swarm propagates in a given direction. In the body frame the velocity field describes two counter-rotating vortices, corresponding to the counter-rotation of each of the species subdomains.

The self-sorting mechanism can be explained as follows: (i) initially the system forms a species homogeneous compact structure, where particles at the boundaries flow freely either counter- or clockwise depending on the sign of their perception misalignment angle γ_i, see Fig. 5.3a-b, (ii) particles flowing in opposite directions

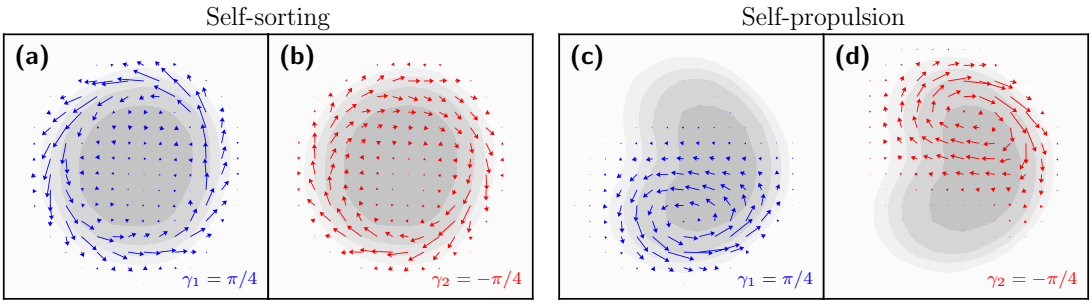

Figure 5.3: *Velocity fields during self-sorting and self-propulsion.* Time-averaged coarsed-grained velocity field during (a-b) self-sorting at $0.02 < t\tilde{\tau} < 0.32$, and (c-d) self-propulsion at $0.9 < t/\tilde{\tau} < 1.2$. Gray color code indicates local number density. The velocity field is obtained in the body frame, and decomposed into species contributions, such that in (c,d) only species 1 are considered, and (b,d) only species 2.

block each other due steric interactions, leading to species accumulations at the boundaries, (iii) the process continues until particles in the bulk also flow to the boundaries where they accumulate, eventually the system fully separates into counter-rotating species subdomains, see Fig. 5.3c-d.

5.2 Dissolving directed swarm

With the parameters $q^* = 1$ and $\gamma = \pi/4$, we have found that the emergent directed swarm leaves a trail of particles thus dissolving over long enough time. To see how the system dissolves, we perform a long simulation with total time $t/\tilde{\tau} = 4$. Particle trajectories show that the swarm performs directed motion followed by spiraling before fully dissolving into a gas, see Fig. 5.4. Particles left behind in

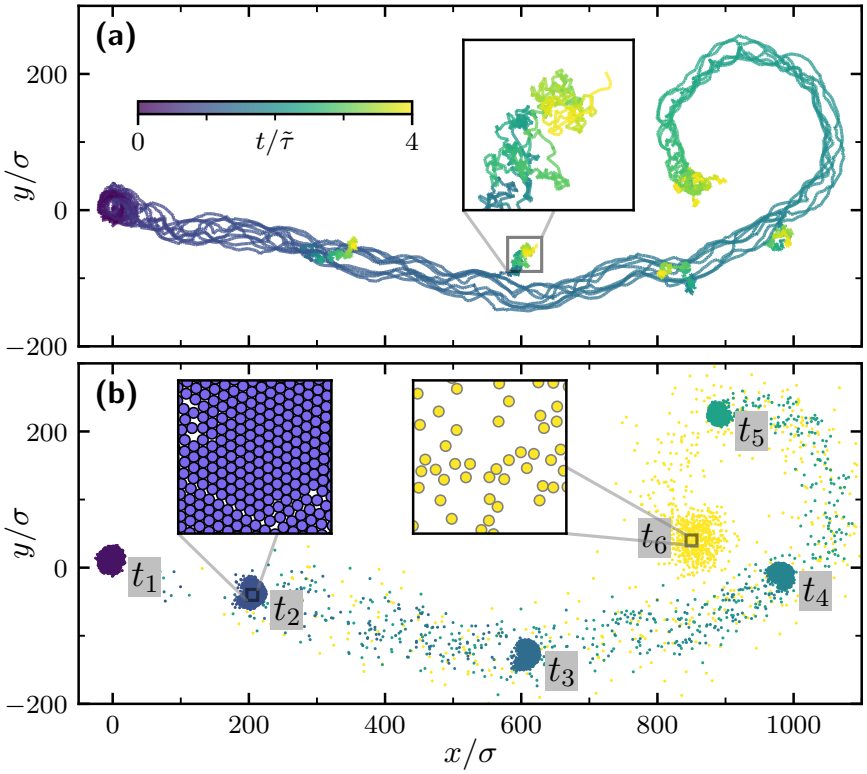

Figure 5.4: *Dissolving directed swarm.* (a) 10 representative particle trajectories color coded by time. Zoom-in shows the trajectory of a particle that is left behind in the trail. (b) Superimposed snapshots of $i = 6$ particle configurations at $t_i/\tilde{\tau} = 0.2,\ 1,\ 1.4,\ 1.8,\ 2.3, 4$. Zoom-ins show particle configurations of the aggregate's bulk at times t_2 and t_6.

the trail do not perceive enough neighbors and are therefore passive displaying a random walk behavior at longer times, see the zoom-in in Fig. 5.5a. Eventually, the swarm loses cohesion so its compact structure fluidizes becoming a dissolved passive gas, see zoom-ins in Fig. 5.5b. Accordingly, we observe three different time-evolution regimes where the system: (i) self-sorts at $t/\tilde{\tau} \lesssim 1$, (ii) self-propels while leaving a trail of particles at $1 \lesssim t/\tilde{\tau} \lesssim 3$, and (iii) dissolves at $t/\tilde{\tau} \gtrsim 3$.

5.2.1 Separation and self-propulsion

To better understand the self-sorting process, we introduce the species separation parameter defined as

$$b_s(t) = \frac{1}{N} \sum_{i=1}^{N} \frac{n_{i,s}(t) - n_{i,o}(t)}{n_i(t)}, \tag{5.1}$$

where n_i is the number of neighbors of particle i, $n_{i,s}$ the number of neighbors of the *same* type as i, and $n_{i,o}$ to the number of neighbors of *opposite* type from i. A particle j is considered to be neighbor of i if the interparticle distance is smaller than a given cutoff radius, $r_{ij} < r_{\text{cut}}$. The separation parameter is minimum with $b_s = 0$ for an homogeneous distribution of neighbors or when the system is diluted, and it is maximum with $b_s = 1$ if the system is completely separated in different domains. Intermediate values $0 < b_s < 1$ account for partially separated domains. In our results, b_s always remains smaller than 1 due to the presence of the interface between sub-domains, as well as the boundaries with empty space. In Fig. 5.5a-b two particle configurations are shown at times $t_1/\tilde{\tau} = 0.5$ and $t_2/\tilde{\tau} = 1.25$, corresponding to cases with $b_s \approx 0.1$ when the cluster is mostly species homogeneous, and $b_s \approx 0.6$ when the particles in the cluster are almost perfectly separated into two well-defined adjacent domains. The time evolution of the parameter $b_s(t)$ is shown in Fig. 5.5c. For the dissolving swarm under consideration, we observe a non-monotonous behavior of $b_s(t)$. The separation parameter vanishes both at $t = 0$ an in the long-time limit, in the former case the system is homogeneously distributed in species, and in the later the system is diluted. The separation parameter monotonously increases from $b_s = 0$ during the self-sorting process at $t/\tilde{\tau} < 1$, reaching a maximum value of $b_s \approx 0.7$. As the swarm dissolves during self-propulsion, b_s decreases monotonously until $t/\tilde{\tau} \approx 3.5$ where $b_s = 0$ again.

To quantify the coupling between species separation and swarm's self-propulsion, we also calculate the center of mass normalized velocity, defined as

$$u_c(t) = \frac{1}{v_0} \sum_{i=1}^{n_c} \frac{|\boldsymbol{r}_i(t + \Delta t) - \boldsymbol{r}_i(t)|}{\Delta t}, \tag{5.2}$$

where the position displacement is measured during the time interval $\Delta t = 10\tau_B = 0.001\tilde{\tau}$. This is a reasonable choice of Δt as it is smaller than the timescale $\tilde{\tau}$

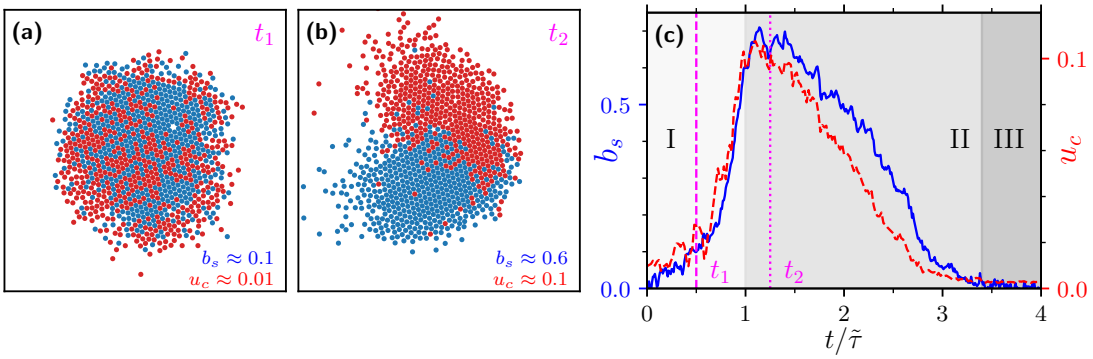

Figure 5.5: *Self-sorting and self-propulsion of a dissolving directed swarm.* Snapshots of particle configurations at times (a) $t/\tilde{\tau} = 0.5$, and (b) $t/\tilde{\tau} = 1.125$. (c) Time evolution of the species separation parameter b_s (left axis), and of the center of mass normalized velocity u_c (right axis). Shaded regions indicate time windows of three dynamical regimes: (I) self-sorting, (II) self-propulsion and dissolution, and (III) dissolution.

during which the system self-sorts, while still larger than the Brownian diffusion timescale $1/D_t$ so displacements due to thermal diffusion do not contribute to the calculation of u_c. To account only for the bulk of the swarm, and disregard particles left behind in the trail, the sum in (5.2) goes over particles in the largest cluster of size n_c (how we perform the cluster analysis is described below). The time evolution $u_c(t)$ is shown in Fig. 5.5c. This parameter behaves very similar to b_s: it monotonously increases from $u_c = 0$ during the self-sorting process, reaches a maximum value of $u_c = 0.1$, then monotonously decreases as the system dissolves at longer times, which clearly indicates that self-sorting and self-propulsion are related phenomena.

5.2.2 Dissolution and activity

To quantify the swarm's dissolution, we identify the largest cluster by performing a cluster analysis as follows: particles i and j are considered to be neighbours if their interparticle distance is $r_{ij} < r_{\text{cut}}$, then the largest collection of neighbours is considered to form the largest cluster. We set the cutoff radius to $r_{\text{cut}} = 1.5\sigma_{\text{eff}}$. This cutoff is small enough to account only for the swarm and not the trail of particles left behind, besides it is slightly larger than the effective particle diameter σ_{eff} to also account for some of the particles in the swarm's outer-layer which are not in hexagonal close-packing but still belong to the largest cluster.

We define then the largest cluster size as

$$n_c = \frac{N_c}{N}, \tag{5.3}$$

where N_c is the number of particles identified to be in the largest cluster, and N the total number of particles in the system. n_c is larger when the system forms a single compact aggregate, and it is very small when the system is diluted. Typical snapshots of these limiting cases are shown in Fig. 5.6a,c. To see how the swarm dissolves over time, we obtain the time evolution $n_c(t)$, see Fig. 5.6e. This quantity shows a clear constant behavior with $n_c = 1$ during the self-sorting process, indicating there the system remains cohesive. Then, during self-propulsion, n_c linearly decays as particles are left behind in the trail. At longer times, before fully dissolving at $t/\tilde{\tau} \approx 3$, we find the cluster has shrunk up, giving $n_c \approx 0.4$. Then,

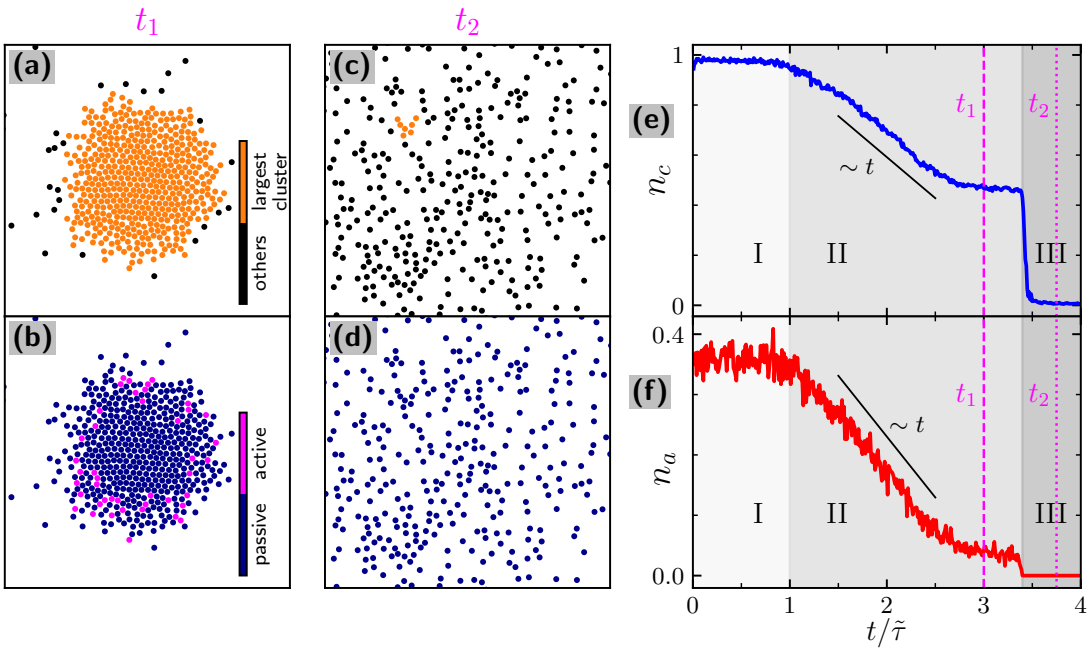

Figure 5.6: *Dissolution of the swarm in the long-time limit.* Snapshots of the particle configuration at time (a-b) $t/\tilde{\tau} = 3$, and (c-d) $t/\tilde{\tau} = 3.725$. In (a,c) color code indicates particles in the largest cluster, and in (b,d) indicates activity. Time evolution of (e) n_c the fraction of particles in the largest cluster, and (f) n_a the fraction of active particles in the largest cluster. Black lines in (e,f) are a guide to the eye indicating linear decrease of the parameters during dissolution. Vertical discontinuous lines indicate times t_1 and t_2 of snapshots in (a-d).

at $t/\tilde{\tau} > 3.5$, the system is dissolved and species are homogeneously distributed with $b_s = 0$, as well as non-motile with $u_c = 0$.

We find n_c abruptly drops to zero during the dissolving regime, meaning cohesion is completely lost, so interparticle distances increase above $r_{ij} > r_{\text{cut}}$. Such abrupt drop is related to particles' activity, as active particles in the outer layer are the ones holding the aggregate together. To quantify this, we calculate the fraction of particles that are active

$$n_a = \frac{N_a}{N}, \tag{5.4}$$

where N is the total number of particles, and N_a the total number of actives. Here we consider the entire system, not only particles in the largest cluster, such that passives in the trail also contribute to the ratio. The activity distribution of particles in the swarm changes over time. Before dissolution, it is mostly passive with only a few actives in the outer layer, then it is only passives when the system is fully dissolved, see Fig. 5.6b,d. The obtained time evolution $n_a(t)$ is shown in Fig. 5.6f. We find that initially the fraction of actives is $n_a \approx 0.35$. After separation, the system starts to lose particles and the amount of actives linearly decays over time. At $t/\tilde{\tau} \approx 3.5$ the amount of active particles has dropped to zero, meaning that there are no active forces left to keep the system cohesive such that the system dissolves, showing the behavior of a passive gas.

5.2.3 Spiraling motion

Another interesting behavior we observe for the system under consideration is the spiraling trajectory described by the swarm before complete dissolution at longer times. We observe that the spiraling direction is in that case counter-clockwise, as can be seen in Fig. 5.4. To better understand this behavior, we consider the swarm's trajectory during the interval $1.8 < t/\tilde{\tau} < 4$, see Fig. 5.7a. Here we observe that the system configuration is separated in species subdomains where particles with $\gamma_1/\pi = 0.25$ display a counter-clockwise rotation (the same direction as the swarm's spiraling trajectory), whereas particles with $\gamma/\pi = -0.25$ rotate in the clockwise direction, as can be seen from the figure insets. The spiraling motion is consequence of fluctuations in the species distribution. As the swarm propagates and leaves a trail of particles behind, the species concentration can vary over time and change the dynamics of the swarm by modifying the velocity field.

To quantify this, we calculate the time evolution of the swarm's species fraction, namely

$$n_i(t) = \frac{N_{c,i}(t)}{N}, \tag{5.5}$$

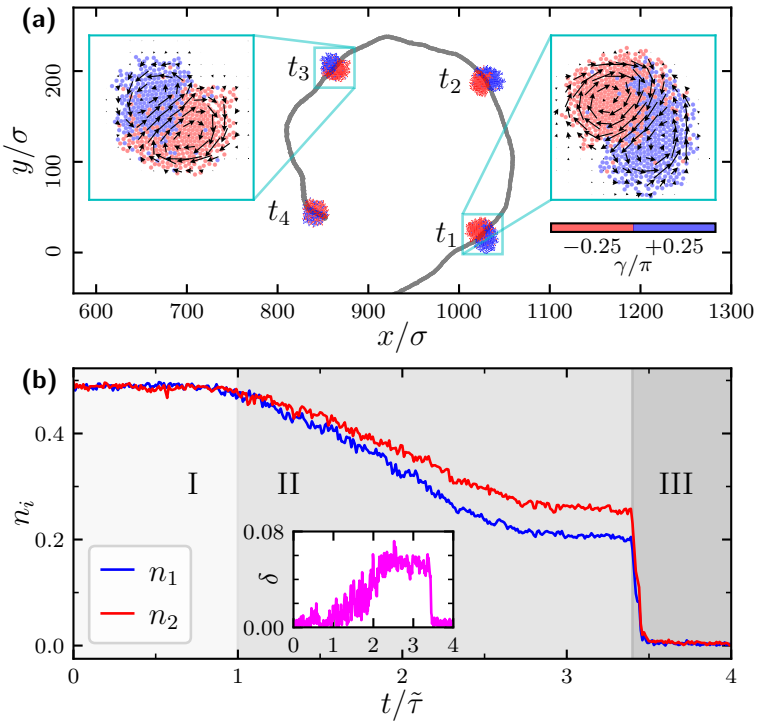

Figure 5.7: *Spiraling motion of the dissolving directed swarm.* (a) Swarm's trajectory at $1.8 < t/\tilde{\tau} < 4$. Configuration snapshots are shown at times $t_i/\tilde{\tau} = 1.8, 2, 2.3, 3$. For better visualization, only particles in the largest cluster are shown. Arrows in the insets correspond to the time-averaged coarsed grained velocity field in the body frame, calculated during an interval of time of $\Delta t/\tilde{\tau} = 0.04$. (b) Time evolution of n_i the fraction of particles of species $i = 1, 2$ in the largest cluster. Inset indicates time evolution of the molarity $\delta = |n_1 - n_2|$.

where $N_{c,i}$ is the number of particles of species $i = 1, 2$ in the largest cluster. Results are shown in Fig. 5.7b. We observe that both n_1 and n_2 stay reasonably constant with $n_1 = n_2 = 1$ during the self-sorting process up to $t/\tilde{\tau} = 1$. During self-propulsion, species fractions monotonously decrease and saturate at $t/\tilde{\tau} > 3$, reaching values of $n_1 \approx 0.2$ and $n_2 \approx 0.25$ such that $n_2 > n_1$. Finally, at $t/\tilde{\tau} \approx 3.5$, we observe that n_1 and n_2 abruptly drop to zero as the largest cluster loses cohesion and dissolves. The parameter

$$\delta = |n_1 - n_2| \tag{5.6}$$

quantifies the *species molarity* of the system; it is $\delta = 0$ when the system is equimolar and $\delta = 1$ when it contains only a single species. In the inset in Fig. 5.7b, we observe an increase in δ, emphasizing that the swarm becomes

non-equimolar over time during self-propulsion. For the simulation considered, we observe that the spiraling direction of the dissolving swarm is dictated by the species with smaller concentration in the largest cluster, in this case species 1 with $\gamma_1/\pi = 0.25$ which produces rotations in the counter-clockwise direction. Note that the dominance of one species over the other, either $n_1 > n_2$ or $n_2 < n_1$ results from spontaneous symmetry breaking as the swarm dynamically changes its species molarity δ, therefore the trajectory can also spontaneously spiral either counter- or clockwise. More detailed analysis of the dynamics of non-equimolar swarms are studied in Ch. 6.

5.2.4 System realizations

To test the types of trajectories that can be described by the dissolving swarm due to symmetry breaking, we perform 24 independent realizations of a binary mixture with fixed parameters $q^* = 1$ and $\gamma = \pi/4$. Results of simulations run until $t/\tilde{\tau} = 10$ are shown in Fig. 5.8a. The center of mass for all realizations here start at the origin, then they describe directed outwards motion. When the swarm is smaller at longer times, its center of mass motion shows to be localized, as indicated by the figure inset. We observe that for different realizations the center of mass propagates isotropically in different directions. We obtain the swarm's distance from the origin at $t/\tilde{\tau} = 10$ and average over the 24 realizations, giving $R_{\rm av} = 780\sigma$ which corresponds to 31 cluster diameters (the size of the swarm is roughly the same as the initial circular configuration $R_0 = 25\sigma$, see snapshots in Fig. 5.2a).

To quantify the average time at which the system completely dissolves, we first compute the largest cluster size n_c for each system realization. Results are shown in Fig. 5.8b. In all cases the system starts as a single cluster containing all particles, giving $n_c = 1$. Then, the system separates and self-propels while leaving a trail of particles behind, leading to a decrease of the largest cluster size until it reaches a minimum of $n_c \approx 0.45$. Next, the swarm loses cohesion and it fully dissolves, showing an abrupt drop to $n_c = 0$. However, from the 24 realizations, only 22 of them fully dissolve, while 2 of them remain of minimum size $n_c^{\rm min} = 0.45$. Considering the 22 realizations where the system dissolves, we calculate the characteristic dissolving time τ_d from

$$n_c(\tau_d) = n_c^{\rm min}, \tag{5.7}$$

where $n_c^{\rm min} \approx 0.45$. We obtain that $\tau_d/\tilde{\tau} \approx 3.2$. Moreover, 22 of the realizations show a decrease of the fraction of actives from $n_a \approx 0.4$ to zero at longer times, and only the 2 realizations that do not fully dissolve and show to saturate with a very

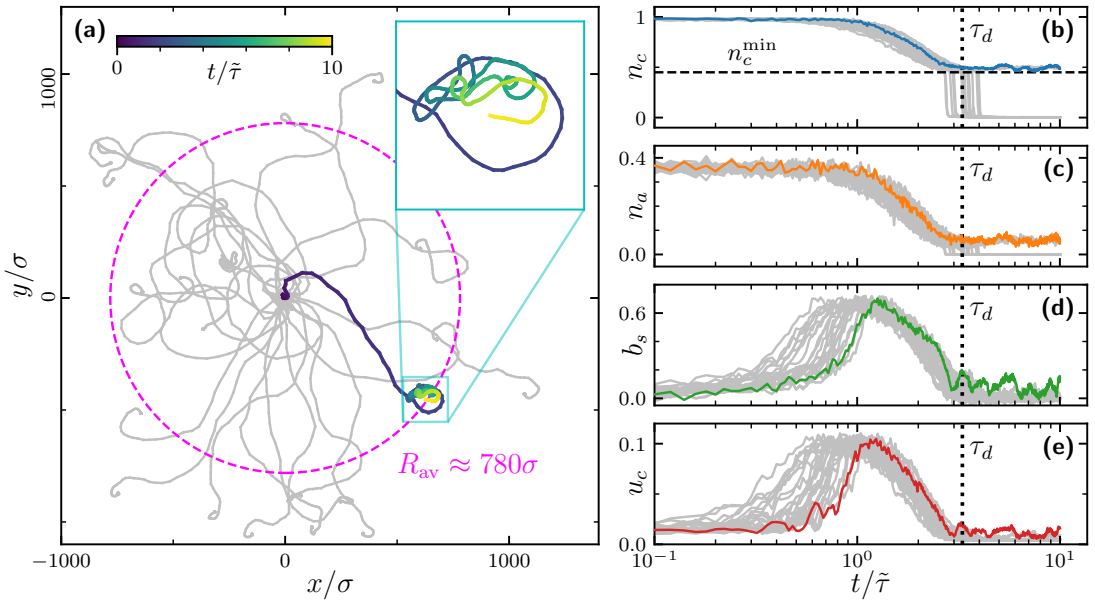

Figure 5.8: *Dynamical behavior of dissolving directed swarms at* $q^* = 1$ *and* $\gamma = \pi/4$. Results for a total of 24 independent realizations. (a) Center of mass trajectories. Dashed circle indicates the average center of mass distance from the origin R_{av} at $t/\tilde{\tau} = 10$. Dynamic parameters defined in Eqs. (5.1) to (5.4), namely (b) largest cluster size n_c, (c) fraction of actives n_a, (d) species separation b_s, and (e) center of mass normalized velocity u_c. Highlighted lines correspond to data of a single realization where the system does not fully dissolve during the simulation time. Vertical dotted lines indicate the dissolution time τ_d, and dashed line in (a) indicates the minimum cluster size n_c^{min} reached before the swarm loses cohesion.

small value of $n_a \approx 0.1$, see Fig. 5.8c. In those two cases, it is that small population of actives that keep the largest cluster cohesive. Nevertheless, all 24 realizations show a non-monotonous behavior for both the species separation parameter b_s and the swarm's velocity u_c, showing a maximum of $b_s \approx 0.7$ and $u_c \approx 0.1$ at time $t/\tilde{\tau} \approx 1$, see Fig. 5.8d-e. This indicates that for all realizations the steady-state is non-separated and non-self-propelling. To understand why in some cases the system does not fully dissolve, note that full dissolution depends on the passive dilution of the trail of particles: when the swarm is surrounded by a passive trail, it can still reabsorb particles to remain cohesive; the swarm loses cohesion only when the trail has diluted enough, and active particles in the outer layer cannot keep the swarm cohesive anymore. Therefore, for very long simulations, we expect that any dissolving swarm should eventually lose cohesion.

5.3 Non-separating loose aggregate

The directed swarm obtained for $q^* = 1$ dissolves as a consequence of particles being left behind at a reasonable distance from the swarm's bulk, such that they are not able to rejoin. Due to the inverse distance dependence of the perception function employed, particles that are far from a reasonably large cluster—the swarm—are guaranteed to be passive. To address this issue, we simply lower the value of the perception threshold q^*, which allows particles to reactivate and rejoin before they are left behind in the trail. However, as we have studied in Ch. 4, q^* has an important impact in the activity distribution, so the formation of species-separated compact swarms is not always guaranteed.

To test this, we perform simulations employing the same system preparation and parameters as in Sec. 5.1, however here we set the perception threshold to $q^* = 0.3$ and run very long simulations, up to $t/\tilde{\tau} = 10$. Snapshots in Fig. 5.9 show that the system remains cohesive as a single loose aggregate which shows to be species homogeneous, i.e. it does not self-sort into definite sub-domains as in the case with $q^* = 1$. Furthermore, the resulting aggregate is mainly active with only a few passives in the outer layer. As we learned in Ch. 4, a low threshold value $q^* = 0.3$ induces particles in the bulk to be active regardless of their orientation, whereas only particles in the outer layer can be passive when their cone of vision points out of the aggregate where they perceive no neighbors. This behavior is independent of the misalignment angle γ and explains why the system here is loose, as more activity in the bulk leads to a loose center as well.

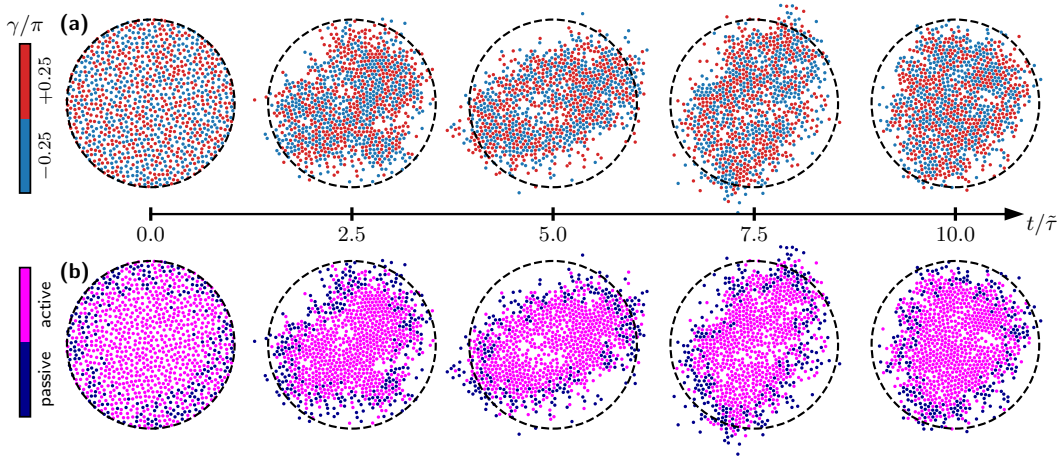

Figure 5.9: *Snapshots of a non-separating loose aggregate at* $q^* = 0.3$. Particle configurations color coded by (a) particle type, and (b) particle activity.

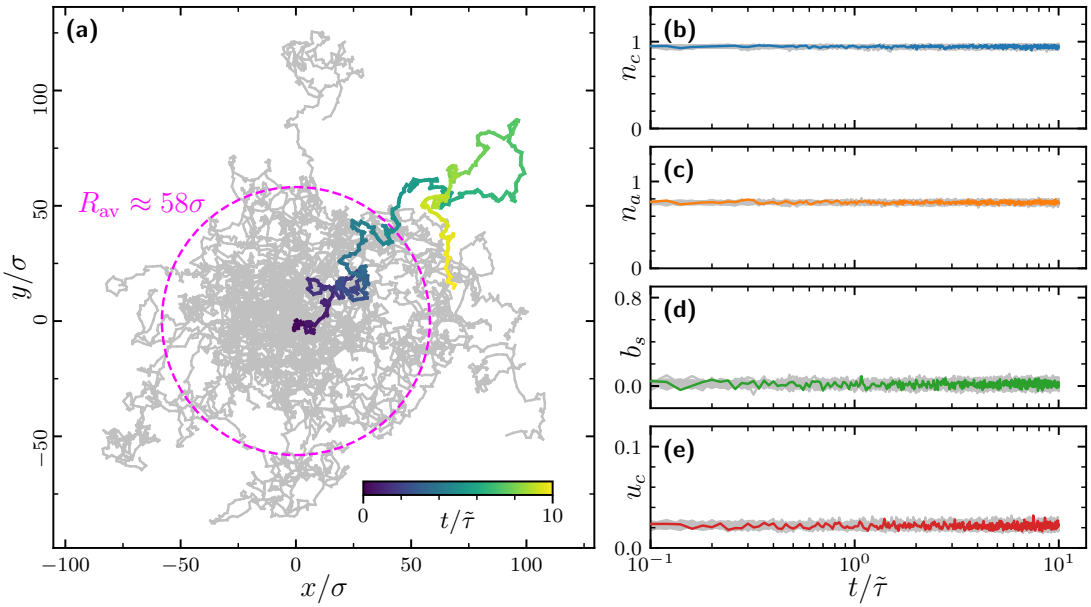

Figure 5.10: *Dynamical behavior of non-separating loose aggregates at* $q^* = 0.3$. Results for 24 independent realizations. (a) Center of mass trajectories. Dashed circle indicates the average center of mass distance at $t/\tilde{\tau} = 10$ which is $R_{\mathrm{av}} \approx 58\sigma$. (b-e) Dynamic parameters defined in Eqs. (5.1) to (5.4). Data corresponding to a single realization is highlighted in each panel for better visualization.

To test the stability of this configuration, we perform 24 independent realizations of the system at $q^* = 0.3$ and $\gamma = \pi/4$. Center of mass trajectories are shown in Fig. 5.10a. We observe that the aggregates in this case do not display persistent directed motion, but rather their trajectories describe a random walk type of motion. We obtain the average over 24 realizations of the aggregates distance from the origin, giving $R_{\mathrm{av}} \approx 58\sigma$ which is much smaller than for dissolving swarms with $q^* = 1$. We also obtain dynamic parameters as defined in Eqs. (5.1) to (5.4). Results in Fig. 5.10b-e show dynamic parameters remain constant for all 24 realizations during the entire simulation, proving the stability of the steady state. The species separation parameter remains $b_s = 0$ during the entire simulation, so the system never self-sorts into subdomains. The center of mass normalized velocity remains very small with $u_c \approx 0.02$ showing the aggregate does not self-propel. The largest cluster size is $n_c \approx 1$, indicating the system forms a single cluster that remains cohesive. $n_a \approx 0.8$ shows that the aggregate is dominated by actives during the entire simulation, as also shown by the snapshots in Fig. 5.9b.

5.4 Robust directed swarm

For an intermediate value of the perception threshold, namely $q^* = 0.7$, we observe swarms that remain cohesive, separate into well-defined species subdomains and perform overall directed motion. We say such swarms are *robust*, i.e. they do not dissolve over time as we have found for swarms at $q^* = 1$. Center of mass trajectories show how the swarms travel long distances during the simulation time of $t/\tilde{\tau} = 10$, see Fig. 5.11, giving an average center of mass distance from the origin of $R_{\text{av}} \approx 5808\sigma$ which is much larger than cases at $q^* = 0.3$ and $q^* = 1$. Corresponding dynamic parameters are shown in Fig. 5.11b-e. We observe that the largest cluster size remains constant over time with $n_c = 1$ for all 24 system realizations, indicating the swarms are cohesive in all cases. This also shows that the swarms remain equimolar as no particles are lost over time, so the species molarity gives $\delta = 0$. The fraction of actives n_a we obtained also show to be constant over time with $n_a = 0.6$, indicating the swarms are dominated by actives. Both the separation parameter b_s and swarm's normalized velocity u_c show a monotonous increase in time saturating at $t/\tilde{\tau} \approx 1$ with values of $b_s = 0.7$ and $u_c = 0.1$, respectively. This behavior implies that species

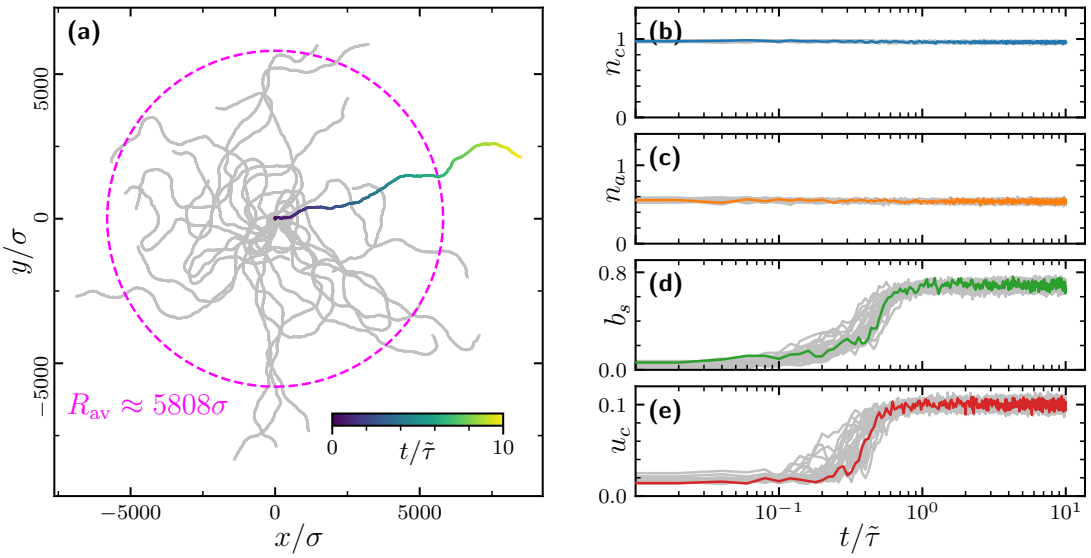

Figure 5.11: *Dynamical behavior of robust directed swarms at* $q^* = 0.7$. Results for 24 independent realizations. (a) Center of mas trajectories. Dashed circle indicates the average center of mass distance at $t/\tilde{\tau} = 10$ which is $R_{\text{av}} \approx 5808\sigma$. (b-e) Dynamic parameters defined in Eqs. (5.1) to (5.4). Data corresponding to a single realization is highlighted in each panel for better visualization.

separation and self-propulsion of the swarms are coupled processes also in this case, thus swarms propagate with maximum speed once they have reached full separation. In contrast to the case $q^* = 1$, here b_s and u_c saturate with positive values at longer times, showing that swarms remain species-separated and keep self-propelling with significant constant speed of $u_c = 0.1$, i.e. 10 times smaller than a colloid's active velocity v_0.

Now we aim to characterize the peculiar bean shape of the directed swarms described above. In particular, we want to quantify how the shape changes with the misalignment angle γ. We focus on the behaviors obtained from particle-based numerical simulations as described in Sec. 5.1 with a perception threshold of $q^* = 0.6$ and intermediate values of the misalignment angle around $\gamma/\pi = 0.2 - 0.35$. We choose these parameters as in those cases we have found that a robust self-propelled swarm is formed. For values below $\gamma/\pi = 0.2$, the swarm is almost circular and does not significantly self-propel, and for values above $\gamma/\pi = 0.35$ the swarm dissolves over time and eventually becomes a gas. To describe the shape, we will use two related parameters: the cluster's elongation λ, and the aperture angle β. We calculate λ by performing a time-average in steady state of the coarsed grained local density, see Fig. 5.12a-b. We consider a reference axis

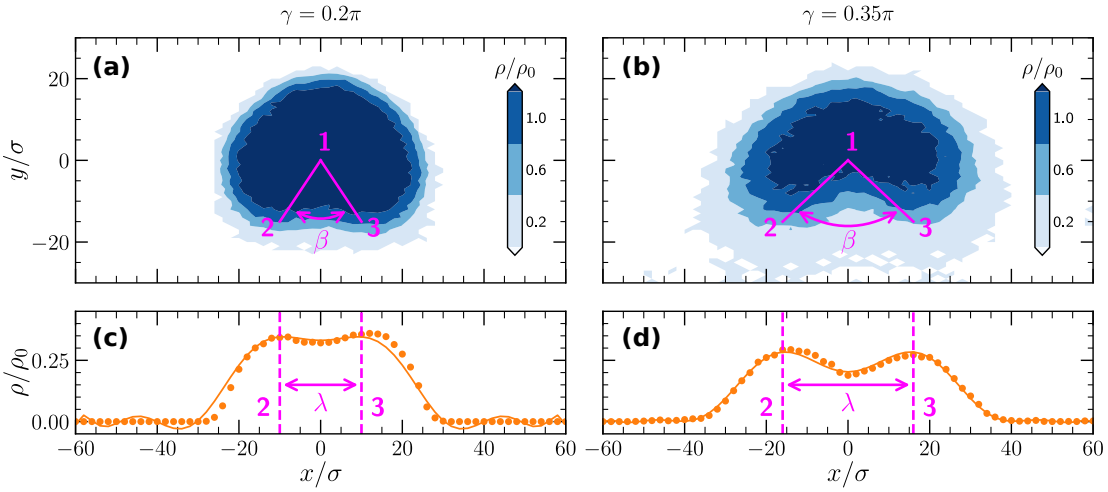

Figure 5.12: *Measurement of the swarm's shape.* Time-averaged coarsed-grained local density ρ for $\gamma = 0.2\pi$ (a) and $\gamma = 0.35\pi$ (b). Local density profiles $\rho(x)$ at $y = -15\sigma$ for $\gamma = 0.2\pi$ (c) and $\gamma = 0.35\pi$ (d). The reference point 1 corresponds to the center of mass, whereas 2 and 3 correspond to the local density maxima obtained from the profiles $\rho(x)$. The distance between density maxima is indicated by λ, and the swarm's aperture angle indicated by β.

in the body-frame, such that the shape of the local density displays a reflexive symmetry $\rho(x) = \rho(-x)$. Next, we obtain the density profiles $\rho(x)$ at a distance $y = -15\sigma$ from the cluster's center of mass $(x_1, y_1) = (0, 0)$. We choose $y = -15\sigma$ as there the density profiles $\rho(x)$ are bimodal due to the distinctive lobes of the bean shaped cluster, with two maxima measured at $(x_2, y_2) = (-x_{\max}, -15\sigma)$, and $(x_3, y_3) = (x_{\max}, -15\sigma)$, see Fig. 5.12c-d. We define the elongation as the separation between the two density maxima,

$$\lambda = 2x_{\max}. \tag{5.8}$$

The aperture angle β is defined as the angle between the segments l_{12} and l_{23}, where l_{12} is defined as the segment between the points (x_1, y_1) and (x_2, y_2), and l_{13} as the segment between the points (x_1, y_1) and (x_3, y_3), see Fig. 5.12a-b. From the law of cosines we have that $\lambda^2 = l_{12}^2 + l_{13}^2 - 2l_{12}l_{13}\cos\beta$. As the swarm's bean shape is symmetrical, the segments equality $l_{13} = l_{23}$ holds, then $\cos\beta = 1 - \lambda^2/2l_{13}^2$. The segment between points 1 and 3 in terms of the elongation λ and the vertical distance $y_1 = -15\sigma$ is given by $l_{13}^2 = (15\sigma)^2 + \lambda^2/4$. It follows that the aperture angle is

$$\beta = \arccos\left\{\frac{1 - (\frac{\lambda}{30\sigma})^2}{1 + (\frac{\lambda}{30\sigma})^2}\right\}. \tag{5.9}$$

With increasing misalignment angle γ, we observe a linear increase of the swarm's elongation, and also of the aperture angle β, see Fig. 5.13a-b. We verify the relation between λ and β is given by Eq. (5.9), see Fig. 5.13c.

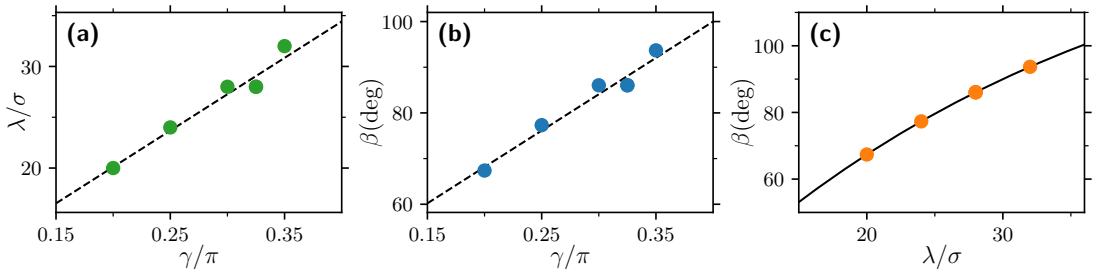

Figure 5.13: *Swarm shape parameters.* Parameters obtained from the measurement of the cluster shape as shown in Fig. 5.12. (a) Aperture angle β and (b) elongation λ as a function of the misalignment angle γ. Dashed lines correspond to a linear fit. (c) Relation between λ and β, solid line corresponds to Eq. (5.9).

5.5 Comparison of dynamical behaviors

Now we quantitatively compare dynamical behaviors of the different types of swarms we have found so far, namely non-separating cases with $q^* = 0.3$, robust with $q^* = 0.7$, and dissolving with $q^* = 1$. To characterize the different types of transport processes, we calculate the mean-squared displacement

$$\mathrm{MSD}(t) = \frac{1}{N}\sum_{i=1}^{N} |\boldsymbol{r}_i(t) - \boldsymbol{r}_i(0)|^2, \tag{5.10}$$

which is a measure of the deviation of the particles positions with respect to their own initial positions. We average over the 24 independent realizations obtained at each given q^*. Results are shown in Fig. 5.14a. We compare the mean-squared displacement with $\mathrm{MSD}(t) \sim t^m$ during the steady state where our results show to follow a power law behavior. Transport is considered to be ballistic when $m = 2$, diffusive when $m = 1$, and sub-diffusive when $m < 1$. In all cases the MSD shows a monotonous increase during the initial collapse (see figure inset) followed by a

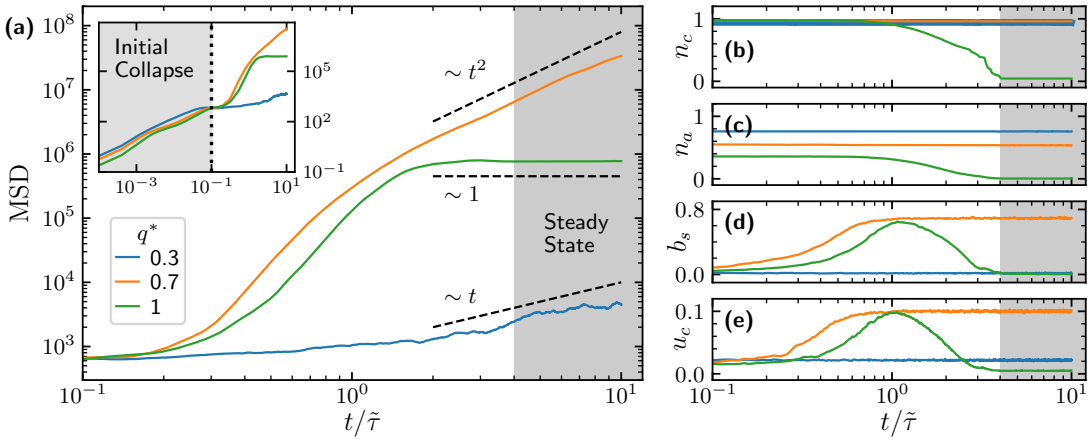

Figure 5.14: *Comparison of averaged dynamic parameters at fixed $\gamma = \pi/4$ varying q^*.* Results correspond to data averaged over 24 independent realizations. Time evolution of (a) mean-squared displacement, (b) largest cluster size n_c, (c) fraction of actives n_a, (d) separation parameter b_s, and (e) swarm's normalized velocity u_c. Shaded region corresponds to the steady state $t/\tilde{\tau} > 4$. Dashed lines in (a) are a guide to the eye showing different scaling behaviors of the mean-squared displacement $\mathrm{MSD} \sim t^m$, where $m = 0$ corresponds to a sub-diffusive transport, $m = 1$ diffusive, and $m = 2$ ballistic. Inset shows data at short times $t/\tilde{\tau} < 1 \times 10^{-1}$ corresponding to the initial collapse.

plateau around $t/\tilde{\tau} = 1 \times 10^{-1}$ when the system is a single compact aggregate and the self-sorting phase starts. At $t/\tilde{\tau} > 1 \times 10^{-1}$ for non-separating aggregates with $q^* = 0.3$, we observe that the MSD increases again and reaches steady state at $t/\tilde{\tau} \approx 4$ displaying approximate diffusive transport MSD $\sim t$. This corresponds to the Brownian type of motion we observe for non-separating aggregates, see Fig. 5.9. For robust directed swarms obtained at $q^* = 0.7$, the transport seems to be super-ballistic during the transient with $m > 2$, as a result of the system self-sorting then self-propelling, going from an almost static position to perform ballistic directed motion in steady state with MSD $\sim t^2$. From trajectories in Fig. 5.11 we observe that indeed the swarms center of mass describe almost straight motion, however sometimes it can also perform sharp turns and continue straight in a different direction. Therefore, for much longer simulations where trajectories are able to cover larger areas, it is expected that the transport becomes diffusive. For dissolving directed swarms at $q^* = 1$, the transport is also super-ballistic during the transient, then sub-diffusive with MSD ~ 1 in steady state when the center of mass of the system does not displace significantly for the time considered.

To complete the picture, we also show the average over 24 realizations for the dynamic parameters in Figs. 5.8 to 5.11. Results are shown in Fig. 5.14b-e. We observe that before reaching steady state, some of the dynamic parameters vary during the transient process, which was discussed in detail in Secs. 5.2 to 5.4. From values in steady state it is clear that at $q^* = 0.3$ the system is cohesive giving $n_c = 1$, it is mainly active with $n_a = 0.8$, non-separated $b_s = 0$, and its center of mass slowly moves with $u_c = 0.02$. At $q^* = 0.7$ the system is cohesive $n_c = 1$, it is mostly active with $n_a = 0.6$, separated with $n_c \approx 0.75$, and propagates with velocity $u_c = 0.1$. At $q^* = 1$ the system dissolves into a passive gas leading to $n_c = 0$ and $n_a = 0$, the gas is also species homogeneous $b_s = 0$ and its center of mass does not propagate $u_c = 0$, emphasizing the sub-diffusive transport of the swarm shown in Fig. 5.14a.

5.6 Exploration of the parameter space

To determine the range of parameters (q^*, γ) over which the system either dissolves or remains as a robust directed swarm and complete the picture provided in previous sections, we perform several additional simulations with $q^* \in (0.2, 1.3)$ and $\gamma/\pi \in (0, 0.5)$. We run long simulations up to a time of $t/\tilde{\tau} = 10$.

5.6.1 Steady state properties for varying q^*

We compute the dynamic parameters defined in Sec. 5.1 for the case $\gamma/\pi = 0.25$ and varying q^*. We test 12 values of q^*, and divide our results into low threshold $q^* \in (0.2, 0.4)$, medium $q^* \in (0.5, 0.7)$, and high $q^* \in (0.8, 1.3)$, see Fig. 5.15. At very low perception threshold, for $q^* = 0.2$ the largest cluster size displays a constant value of $n_c \approx 0.7$ over time, but also displays strong fluctuations around the mean. As the system here is mostly active with $n_a \approx 0.8$, the particle spatial distribution can rapidly rearrange giving strong fluctuations of the interparticle distances r_{ij}, hence it is more probable to have particle pairs with $r_{ij} > r_{\text{cut}}$, where $r_{\text{cut}} = 1.5\sigma_{\text{eff}}$ is the cutoff radius employed in the cluster analysis. Thus explaining the fluctuating behavior of n_c in this case. For $q^* = 0.3, 0.4$ we also observe that the system remains cohesive with $n_c = 1$ without showing significantly large fluctuations. Fraction of actives n_a are also constant in time, we observe decreasing values from $n_a \approx 0.8$ for $q^* = 0.2$ to $n_a \approx 0.7$ for $q^* = 0.5$, which agrees with the fact that particles are less likely to become active when

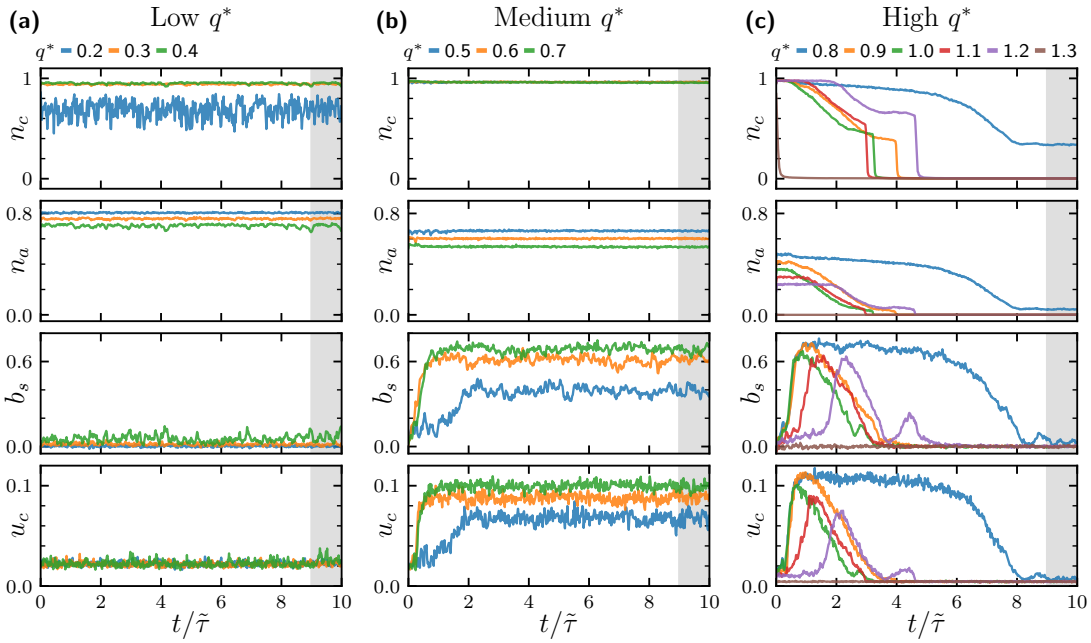

Figure 5.15: *Dynamic parameters at fixed $\gamma = \pi/4$ and varying q^*.* Time evolution of the largest cluster size n_c, fraction of actives n_a, species separation b_s, and normalized center of mass velocity u_c. Columns correspond to (a) low (b) medium, and (c) high values of the perception threshold q^*. Shaded region indicates the steady state $t/\tilde{\tau} > 9$.

the perception threshold becomes larger. For all $q^* = 0.2, 0.3, 0.4$ we observe the system does not separate nor self-propel, giving $b_s = 0$ and $u_c \approx 0.02$. Therefore, we identify cases with low perception threshold to correspond to non-separating loose aggregates as described in Sec. 5.3.

For intermediate values of the perception threshold, namely $q^* = 0.5, 0.6, 0.7$, the largest cluster size is $n_c \approx 1$, and it is constant over time, indicating in all cases the system remains cohesive. Again, we observe the fraction of actives remains constant over time, showing a slight decrease from $n_a \approx 0.7$ for $q^* = 0.5$ to $n_a \approx 0.5$ for $q^* = 0.7$. Both the species separation parameter and the swarm's speed show a monotonous increase at short times, then saturate for most of the simulation indicating the system remains stable. We conclude that systems with $q^* = 0.5, 0.6, 0.7$ shown here correspond to robust directed swarms, as studied in Sec. 5.4, with steady state separation parameter of $b_s \approx 0.4, 0.6, 0.7$, and swarm speed $u_c \approx 0.07, 0.09, 0.1$.

For perception threshold $q^* = 0.8$, $n_c(t)$ shows a very slow decrease and saturate in steady state with a low value of $n_c \approx 0.4$. The fraction of actives also decrease and saturate with an almost vanishing value of $n_a \approx 0.05$. The species separation parameter and swarm speed both show a non-monotonous behavior with $b_s = u_c = 0$ in steady state. Therefore, we identify this case to be a dissolving swarm where, at longer times, a small aggregate coexist with a trail of particles. Some of the particles in the trail can reactivate and rejoin the aggregate thus keeping it cohesive, however cohesion can still be lost at even longer times due to a density fluctuation in the trail—which we do not see in this case. For $q^* = 0.9 - 1.2$ we observe the behavior of dissolving directed swarms as studied in Sec. 5.2, namely: $n_c(t)$ and $n_a(t)$ decrease over time then abruptly drop to zero indicating lost cohesion, whereas $b_s(t)$ and $u_c(t)$ show a non-monotonous behavior indicating the system self-sorts and self-propels initially but the emergent swarms here leave a trail of particles behind and eventually dissolve. For $q^* = 1.2$ we observe a second peak appearing for $b_s(t)$ and $u_c(t)$ around $t/\tilde{\tau} \approx 4$, corresponding to a cluster that is formed again from the trail of particles, which can occur due to sufficiently large density fluctuation in the trail. However, as the trail keep passively diffusing, the reformed cluster quickly loses cohesion, leading again to vanishing values of $b_s 0$ and u_c again. For $q^* = 1.3$ we observe all dynamic parameters vanish during the entire simulation, indicating that cohesion is lost immediately, particles remain passive and the system never separates, nor self-propels. In this case the perception threshold is so high that the initial configuration simply diffuses as a passive gas from the beginning.

We quantify parameters in steady state by averaging data shown in Fig. 5.15 over the time window $9 < t/\tilde{\tau} < 10$. Results are shown in Fig. 5.16. In steady state, we observe that the largest cluster size $\overline{n_c}$ reaches a plateau of $\overline{n_c} \approx 1$ over

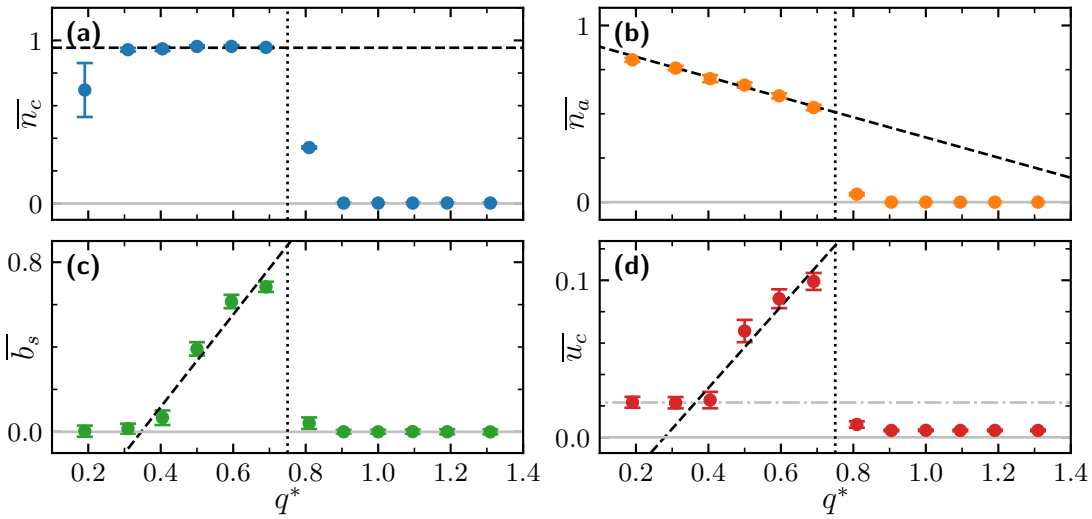

Figure 5.16: *Steady state parameters at fixed $\gamma = \pi/4$ and varying q^*.* Steady state parameters obtained by averaging data shown in Fig. 5.15 over the time window $9 < t/\tilde{\tau} < 10$. Dashed lines corresponds to a linear fit of the steady state values at $q_c^* = 0.4 - 0.7$. Vertical dotted lines indicate the critical perception threshold value $q^* \approx 0.75$. Dashed dotted silver line in (d) corresponds to the swarm speed value of $\overline{u_c} \approx 0.02$.

a range of values of the perception threshold, namely for $q^* = 0.3 - 0.7$, then it decreases and drops to zero for higher values $q^* = 0.8 - 1.3$. A transition from cohesive to non-cohesive is found to occur around the critical value $q_c^* \approx 0.75$. The fraction of actives $\overline{n_a}$ show a linear decrease for $q^* = 0.2 - 0.7$, then it abruptly drops to zero for q^* larger than the critical threshold. Both the species separation parameter $\overline{b_s}$ and swarm speed $\overline{u_c}$ show a non-monotonous behavior with q^*. At $q^* = 0.5 - 0.7$, these parameters show a linear increase until they reach a maximum of $\overline{b_s} \approx 0.7$ and $\overline{u_c} \approx 0.1$ at $q^* = 0.7$. Therefore, we identify a transition of the system from non-separated to separated self-propelled around $q^* \approx 0.45$. Note that non-separating loose aggregates occurring at $q^* \leq 0.4$ show a very small yet non-vanishing velocity of $\overline{u_c} = 0.01$, corresponding to a random walk motion as seen in Fig. 5.10.

5.6.2 Steady state properties for varying γ

The misalignment angle γ, taken to be of same magnitude for both species (i.e. $\gamma_1 = -\gamma_2 = \gamma$), plays a crucial role in the dynamics of the binary mixture. In the totally aligned case $\gamma = 0$, the system corresponds not to a mixture but to a

system containing a single species of particles, which we know self-organizes into a cohesive non-separating and non-motile compact aggregate, as we previously studied in chapters 3 and 4. For lateral visual perception $\gamma = \pi/2$, i.e. when the cone of vision is perpendicular to the direction of self-propulsion of the particles, the system is expected to be non-cohesive, given that in this case there is no special preference for particles to actively move towards or away of the aggregate. Therefore, emerging directed swarms are expected to occur only for intermediate values of the misalignment angle within the open interval $\gamma/\pi \in (0, 0.5)$. To characterize behaviors within this range of values, we perform particle-based numerical simulations employing the same parameters as in Sec. 5.1, for a total time of $t/\tilde{\tau} = 10$. In this case, we fix the perception threshold to $q^* = 0.7$ and test several values of the misalignment angle γ.

We separate our results for low values of the misalignment angle $\gamma/\pi = 0{-}0.15$, medium values $\gamma/\pi = 0.175 - 0.275$, and high $\gamma/\pi = 0.3 - 0.5$. From results shown in Fig. 5.17, we can identify that systems with low misalignment angle γ correspond to non-separating loose aggregates, as parameters $n_c = 1$, $b_s \approx 0$,

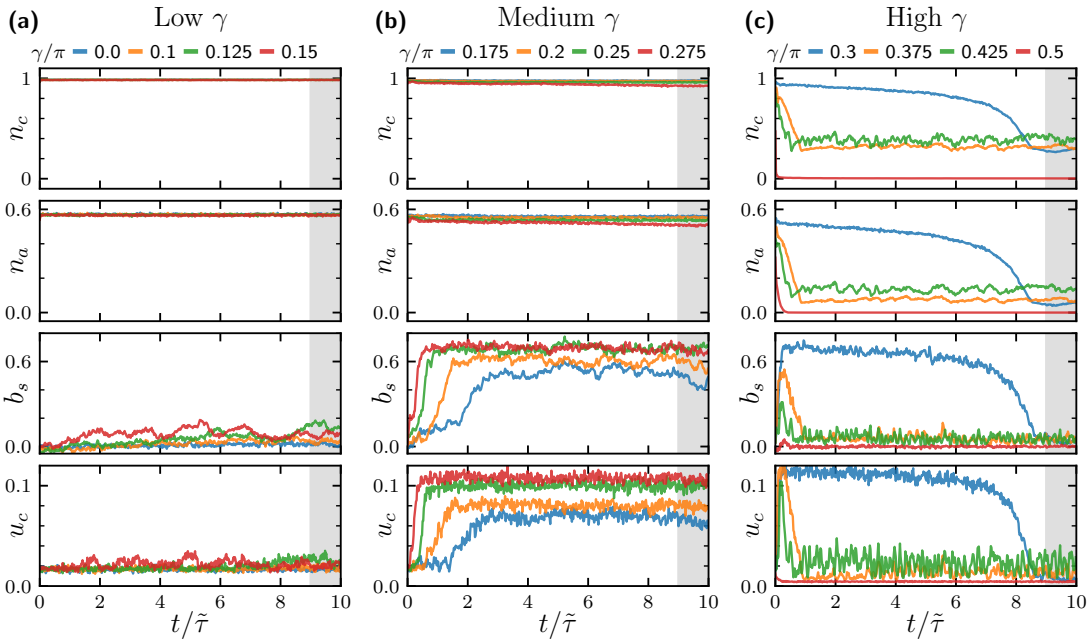

Figure 5.17: *Dynamic parameters at fixed $q^* = 0.7$ and varying γ.* Time evolution of the largest cluster size n_c, fraction of actives n_a, species separation b_s, and normalized center of mass velocity u_c. Columns correspond to (a) low (b) medium, and (c) high values of γ. Shaded region indicates the steady state $t/\tilde{\tau} > 9$.

and $u_c \approx 0.02$ remain constant over the entire simulation. The fraction of actives $n_a \approx 0.6$ remains constant in all cases, showing this parameter does not depend on γ. Medium values of γ correspond to robust directed swarms; cohesion is observed from constant $n_c = 1$ over the entire simulation, as well as monotonously increasing species separation $b_s(t)$ and swarm speed $u_c(t)$ parameters which saturate at longer times. Again, here $n_a \approx 0.6$, emphasizing this parameter depends only on the perception threshold q^* but not γ. High values of γ shown here correspond to dissolving directed swarms. For $\gamma/\pi = 0.3, 0.375, 0.425$ we observe systems that do not lose cohesion at longer times but remain with finite largest cluster size $n_c \approx 0.4$. In those cases also $n_a \approx 0.1$, indicating there is a non-vanishing population of actives keeping the largest cluster cohesive. $b_s(t)$ shows to decrease and vanish at longer times. $u_c(t)$ also decreases and fluctuates around an average very small value $u_c \approx 0.02$ corresponding to random walk motion.

We obtain steady state parameters by averaging data from dynamic parameters during $9 < t/\tilde{\tau} < 10$ which we regard as the steady state. Results are shown in Fig. 5.18. In steady state, the largest cluster size shows a plateau of $\overline{n_c} = 1$ for $\gamma/\pi < 0.29$. For larger misalignment angle, $0.29 < \gamma/\pi < 0.5$, $\overline{n_c}$ shows to be significantly smaller yet non-vanishing. This behavior corresponds to clusters

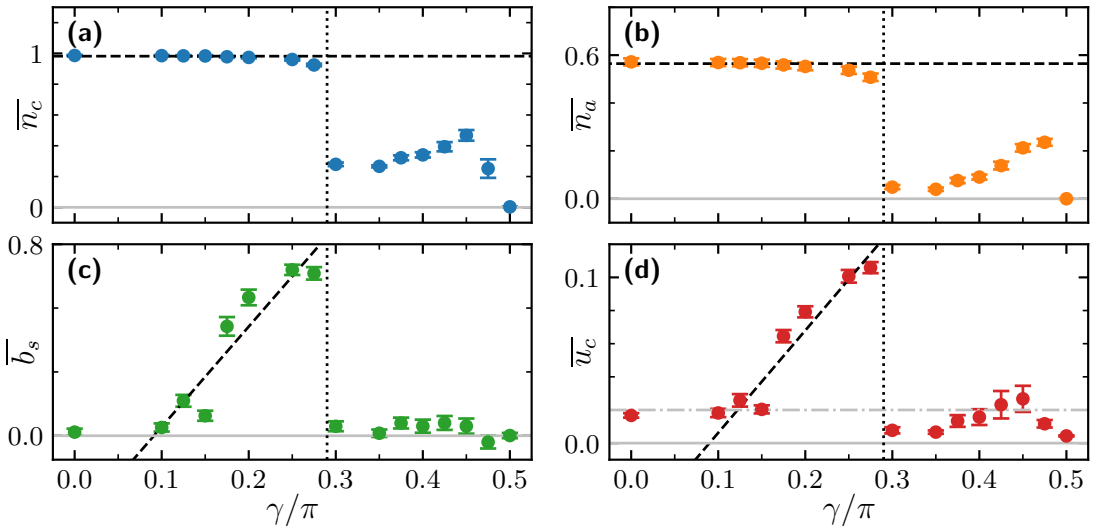

Figure 5.18: *Steady state parameters at fixed $q^* = 0.7$ and varying γ.* Averages in steady state of the dynamical parameters. Vertical dotted lines indicate the critical misalignment angle value $\gamma_c \approx 0.29$. Dashed lines in (a,b) fit plateau regions at $\gamma < \gamma_c$. Dashed lines in (c,d) correspond to linear fitting of the data for $\gamma/\pi = 0.1 - 0.275$. Dashed dotted line in (d) corresponds to $\overline{u_c} \approx 0.02$.

that do not lose cohesion but coexist with a trail of particles during the simulation time considered, but as we argued before this system is metastable and a density fluctuation in the trail would end the cohesion of the aggregate. We identify a transition occurring at a critical misalignment angle of $\gamma_c/\pi = 0.29$, where the system changes from being a single cohesive aggregate at $\gamma < \gamma_c$ to a small metastable aggregate at $\gamma > \gamma_c$. The fraction of actives shows a similar transition from $\overline{n_a} \approx 0.6$ at $\gamma < \gamma_c$ to smaller values between $0 < n_a < 0.2$, corresponding to active particles in the outer layer of the metastable aggregate. Parameters b_s and u_c both show a similar qualitative behavior in the steady state values. This emphasizes both separation into species sub-domains and swarm self-propulsion are coupled effects. We observe that emergent directed swarms occur only for $\gamma/\pi = 0.175 - 0.3$, which show a linear increase in the species separation and swarm speed with maximum values of $\overline{b_s} \approx 0.7$ and $\overline{u_c} \approx 0.1$ at $\gamma/\pi = 0.3$.

5.6.3 Phase diagram

To finish characterizing the parameter space, now we aim to gather all our results into a phase diagram (γ, q^*) for which we perform some additional simulations with parameters $q^* = 0.3 - 1.3$ and $\gamma/\pi = 0 - 0.5$ run until $t/\tilde{\tau} = 10$. We run single realizations for each pair (γ, q^*) and consider the steady state to be $t/\tilde{\tau} > 9$. Results for the steady state largest cluster size $\overline{n_c}$ and species separation parameter $\overline{b_s}$ are shown in Fig. 5.19. To establish a criteria to differentiate between different phases, we regard systems with $\overline{n_c} < 0.8$ to be diluted, and

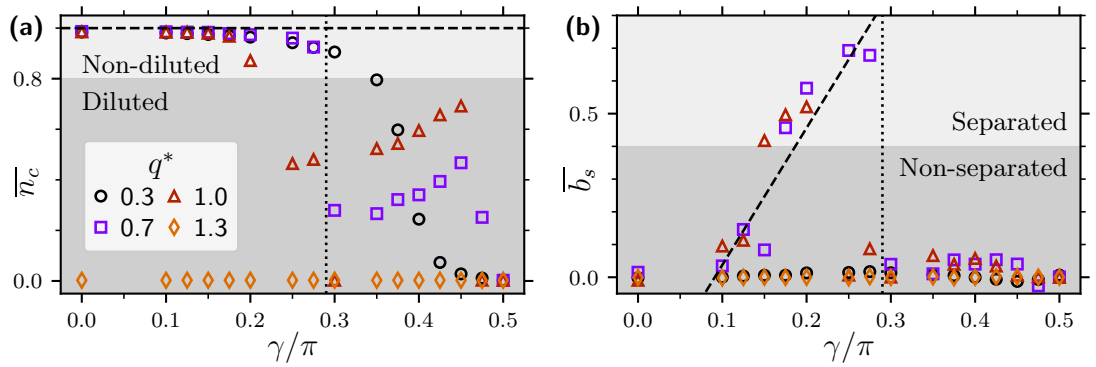

Figure 5.19: *Steady state averages for varying γ and fixed q^*.* (a) Largest cluster size $\overline{n_c}$, and (b) species separation parameter $\overline{b_s}$. Vertical dotted lines correspond to the critical misalignment angle $\gamma_c/\pi = 0.29$ found for $q^* = 0.7$. Dashed line in (a) corresponds to $\overline{n_c} = 1$, and in (b) to a linear fit of the data for $\gamma/\pi = 0.1 - 0.275$ at $q^* = 0.7$.

systems with $\overline{b_s} > 0.4$ to be separated. We observe that for $q^* < 1.3$ and $\gamma < \gamma_c$ most systems remain cohesive with $n_c > 0.8$, such that those cases are considered as non-diluted. For $\gamma > \gamma_c$ we observe intermediate values $0 < \overline{n_c} < 0.8$, which correspond to metastable cohesive aggregates—aggregates in coexistence with a diluted trail. Moreover, all those cases are non-separated as they show $\overline{b_s} \approx 0$, meaning that while metastable aggregates remain cohesive at longer times they do not separate, hence do not self-propel. Separated cases are observed only for intermediate values of the misalignment angle $\gamma/\pi = 0.1 - 0.275$. Note also that for $q^* = 1.3$ systems are always diluted and non-separated.

Our results are better visualized in the phase diagram shown in Fig. 5.20. The criteria to identify each phase is as follows: (I) non-diluted (cohesive) and non-separated aggregates correspond to cases with $\overline{n_c} > 0.8$, and $\overline{b_s} < 0.4$; (II) cohesive species separated directed swarms have $\overline{n_c} > 0.8$, and $\overline{b_s} > 0.4$; (III) Diluted non-separated systems have $\overline{n_c} < 0.8$ and $\overline{b_s} < 0.4$. Here we observe that smaller values of (γ, q^*) correspond to species homogeneous loose aggregates, and larger values to species homogeneous diluted systems. Robust directed swarms exist only for intermediate values of (γ, q^*).

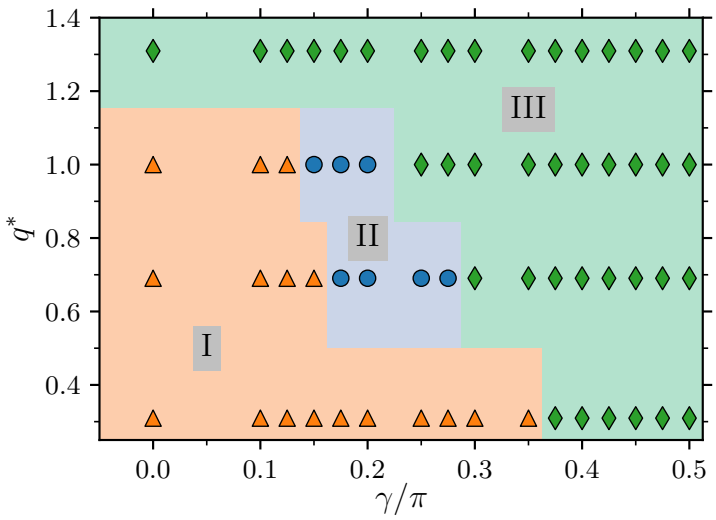

Figure 5.20: *Phase diagram γ-q^*.* Phase diagram showing regions of systems with behaviors: (I) non-separating loose aggregates, (II) robust directed swarms, and (III) species homogeneous diluted systems—including cases where dissolving directed swarms initially emerge.

5.7 Summary

We have described a simple yet interesting self-organization strategy of an equimolar mixture of particles with opposite misaligned visual perception and discontinuous motility that leads to particle aggregation, separation into counter-rotating species subdomains, and subsequent self-propulsion of the directed swarms. For misalignment angle $\gamma/\pi = 0.25$ and perception threshold $q^* = 0.7$ we found such emergent directed swarms remain robust over time and show super-diffusive transport. For a larger threshold value $q^* = 1$, we found swarms leaving a trail of particles as they propagate, thus dissolving over time. At longer times they become non-equimolar as they leave particles behind that can be either of species 1 or 2, this translates into a spiraling motion of the swarm, which can be either counter- or clock-wise due to spontaneous symmetry breaking. For lower threshold $q^* = 0.3$ we found that the system forms species homogeneous cohesive loose aggregates that are mainly active, display strong fluctuations of the particle distribution, and Brownian-like motion of the center of mass.

We studied how varying misalignment angle influences the bean shape of the swarms, which we quantified by means of the bean aperture angle β and elongation λ. We found the two parameters to linearly increase with γ. To characterize the dynamics of the system, we computed dynamic parameters like the largest cluster size n_c, species separation b_s, swarm's speed u_c, and the fraction of actives in the largest cluster n_c. We found the swarm's speed and species separation parameter to be highly correlated in time, showing a maximum of $\overline{b_s} = 0.7$ and $\overline{u_c} = 0.1$ for robust directed swarms with $\gamma = \pi/4$ and $q^* = 0.7$. Finally, we obtained steady state time averages of the dynamic parameters, which served to identify the different phases for different particle parameters allowing us to obtain a phase diagram (γ, q^*).

6 Swarms with guided trajectories

The design of new strategies to control the dynamics of groups of self-propelled particles is one of the important challenges of the actual research in active matter systems. Until now we have shown how particles with perception-dependent motility can change from a dilute non-cohesive group to a cohesive static cluster, cohesive rotating, and also to a cohesive group with intrinsic self-propulsion. To find simple procedures that allow to guide the swarm is the goal of this chapter. External manipulation of the dynamics of active colloids have been achieved before by several methods, e.g. by employing external magnetic fields [23, 175–178], light fields [176, 177, 179, 180], and acoustics [176, 181]. Understanding what system parameters lead to self-organized swarms that navigate with specific types of trajectories can be useful to develop future technological applications, for example to perform targeted drug delivery [29, 182–184].

We now want to study cases where the emerging swarms describe different types of trajectories, which allow to guide their overall motion. We approach this in two different ways. In Sec. 6.1, we study the case when the swarm is non-equimolar while remaining cohesive over time. We perform particle-based numerical simulations by considering parameters corresponding to a robust directed swarm, i.e. perception threshold $q^* = 0.7$ and misalignment angle $\gamma = \pi/4$. We show how species-separated swarms emerge at given values of the species number ratio determined by N_1 and N_2, or in other words at given molarity δ. We find the resulting swarms display either a straight, helical, or a random walk type of motion. We characterize the center of mass trajectories for each case, as well as the swarm's speed u_c, mean-squared displacement (MSD) and velocity autocorrelation $C_{\boldsymbol{vv}}$. In Sec. 6.2, we investigate how to externally guide the motion of the swarms to achieve trajectories describing specific patterns. In this case, we propose a simple strategy that consists in dynamically switching the misalignment angles of the particles between $\gamma_1 = -\gamma_2$ and $\gamma_1 = \gamma_2$, leading the swarm trajectories to describe a straight pattern followed by a brief rotation or turn, we therefore refer to these as run-and-turn swarms. We also characterize the time it takes a species-separated swarm to demix when choosing $\gamma_1 = \gamma_2$, which is useful to tune the specific dynamics.

6.1 Non-equimolar mixtures

For binary mixtures of particles with perception-dependent motility and misaligned vision, we found a case where a dissolving directed swarm emerges given parameters $\gamma = \pi/4$ and $q^* = 1$. The trajectory of the swarm showed first a straight trajectory followed by a helical motion and dissolution of the swarm into a passive gas. We associated the helical motion to the molarity variation of the swarm, that occurred as the swarm leaves a trail of particles over time. Here we study in more detail the impact on the swarm dynamics produced by changing the system's molarity. For this, we perform particle-based numerical simulations, where we consider parameters corresponding to the emergence of a robust directed swarm, i.e. a system with $\gamma = \pi/4$ and $q^* = 0.7$, see Sec. 5.4. We initialize particles with an homogeneous spatial distribution within a circle of radius $R_0 = 25\sigma$, with species distribution homogeneous as well. Then, the dynamics of the resulting aggregate depends on the molarity parameter $\delta = |n_1 - n_2|$, which we defined in Eq. (5.6)—the fraction of particles of species $i = 1, 2$ is $n_i = N_i/N$, with N_i the number of particles of species i, and $N = N_1 + N_2$ the total number of particles. From definition, $\delta = 0$ corresponds to an equimolar system $n_1 = n_2$ like the robust aggregate studied in Ch. 5, and $\delta = 1$ to a system containing a single species of particles, like the one studied in Ch. 3 and Ch. 4. Intermediate values $0 < \delta < 1$ correspond to cases where the system is non-equimolar. Here we focus on systems with $N_1 > N_2$.

6.1.1 Helical trajectories

We perform simulations of total run-time $t/\tilde{\tau} = 10$ for systems with molarities $\delta = 0, 0.2, 0.4, 0.6, 0.8, 1$, final snapshots are shown in Fig. 6.1. We observe that in all cases the systems remain cohesive and compact. For the smaller values tested, $\delta = 0, 0.2, 0.4$ (namely percentage ratios of 50:50, 60:40, and 70:30) the system separates into species subdomains, where each subdomain rotates in a definite direction, as dictated by the misalignment angles γ_1 and γ_2. For $\delta = 0.4$ (ratio 70:30) the system is still able to separate, leaving a small subdomain of particles with $\gamma_2/\pi = -0.25$. However, for $\delta = 0.6, 0.8$ (ratios 80:20 and 90:10) the system does not separate anymore, but remains homogeneous in species, showing a rigid-body rotation in the counter-clockwise direction. Such non-separation of the system is due to the very small amount of particles with $\gamma_1/\pi = -0.25$ that are homogeneously distributed within the bulk of the aggregate. In the bulk particles cannot freely move as they are bounded in a closed-packing configuration of neighbours dominated by species with $\gamma_2/\pi = 0.25$. Therefore, these particles are only dragged to rotate in the same direction of motion of the overall aggregate,

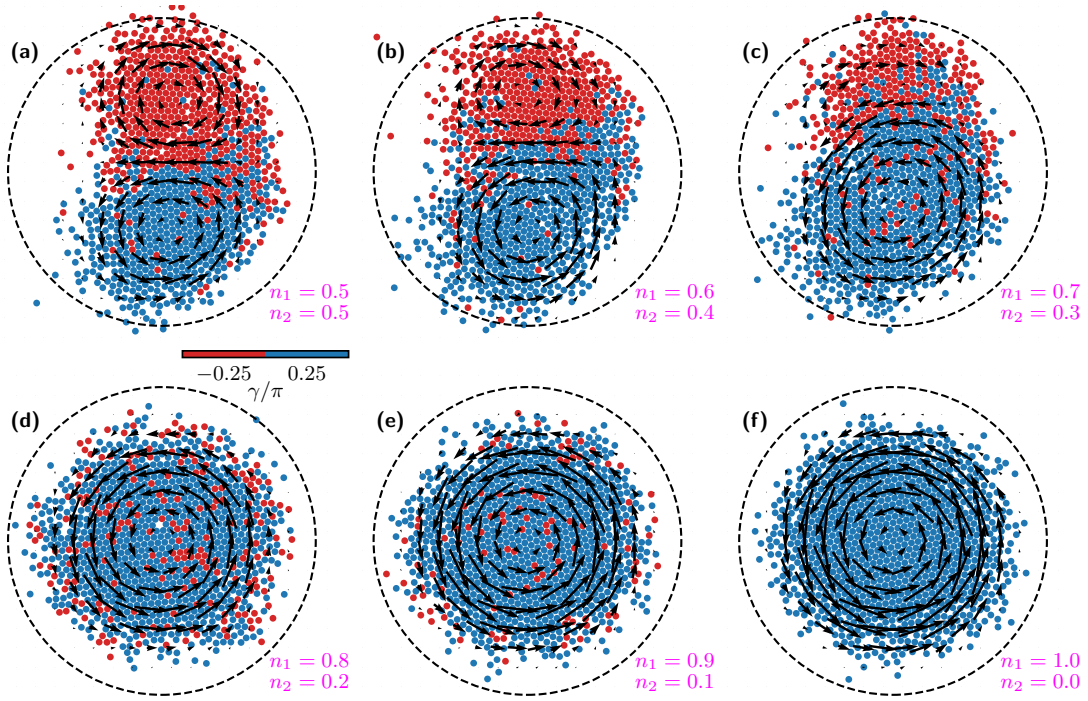

Figure 6.1: *Particle configurations of steady-state mixtures with molarity δ.* Molarity values for (a-f) correspond to $\delta = 0, 0.2, 0.4, 0.6, 0.8, 1$, respectively, with corresponding fraction of particles shown in the labels. Arrows indicate local displacement vector field.

i.e. in the counter-clockwise rotation as dictated by the dominant species. Particles in the outer-layer can move freely, switching their motion from passive to active depending on their orientation. Nonetheless, there are not enough particles with γ_1 to counter-balance the rotation of particles with γ_2.

Center of mass trajectories of cases with $\delta = 0, 0.2, 0.4, 0.6, 0.8, 1$ are shown in Fig. 6.2. We observe that, for the equimolar case $\delta = 0$ the trajectory is clearly drifting in a given direction (in this case towards the upper right corner of the box). This behavior corresponds to the robust directed swarms studied in Ch. 5. Although with a large persistence, it should be noted that this is not a guided motion, and that the direction is given by spontaneous breakdown of the system's symmetry, which is therefore random. Interestingly, for $\delta = 0.2, 0.4$ trajectories display a circling motion; for $\delta = 0.2$ the circling motion is coupled to a drifting of the center of mass thus describing a helical trajectory, whereas for $\delta = 0.4$ the center of mass does not drift a significant amount. Trajectories for larger values of the molarity $\delta = 0.6, 0.8, 1$ display a random-walk type of motion, showing larger

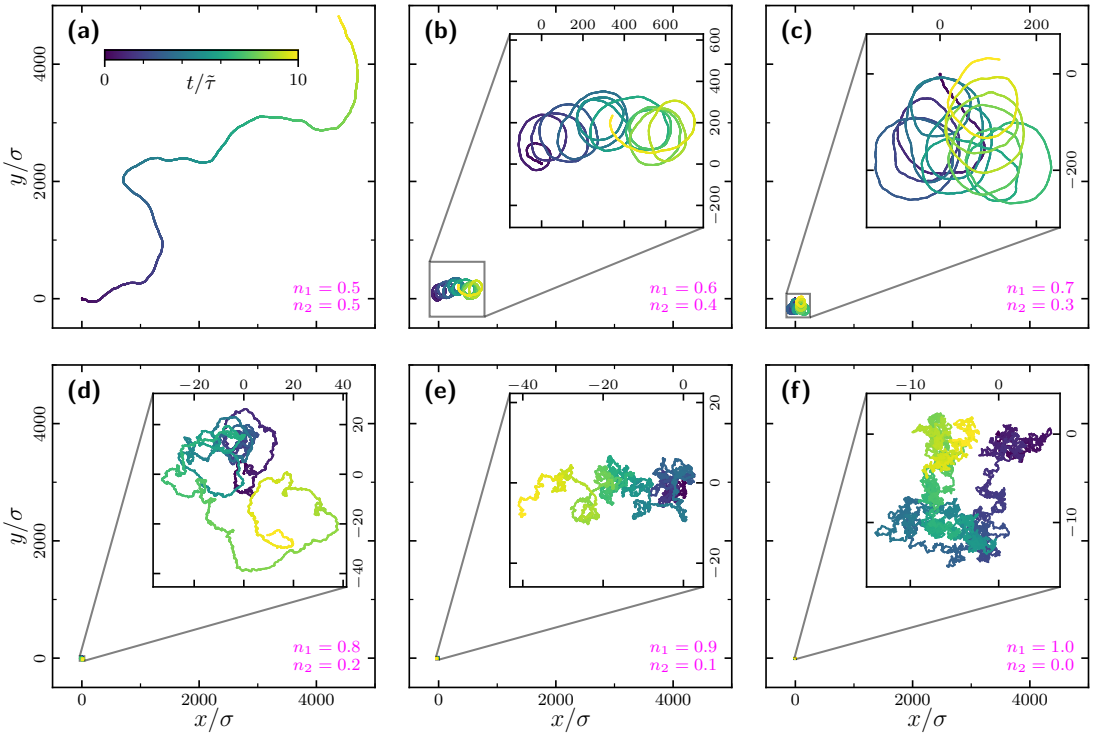

Figure 6.2: *Center of mass trajectories of mixtures with molarity δ.* Trajectories in (a-f) correspond to mixture of particles with molarity $\delta = 0, 0.2, 0.4, 0.6, 0.8, 1$, respectively. Color code corresponds to time evolution. Note the box scale is the same in all of the panels, so the zoom-in in (b-f) allow to see the details of smaller scale trajectories.

displacements for the case $\delta = 0.6$, and smaller displacements for $\delta = 0.8, 1$, i.e. the effective diffusion decreases with δ.

6.1.2 Dynamic parameters

To better characterize the different types of motion of the swarms, first we quantify the swarm's transport properties. For this we calculate the mean-squared displacement as defined in Eq. (5.10). Results for cases $\delta = 0, 0.2, 1$ are shown in Fig. 6.3a. In all cases, the MSD shows a monotonous increase during the initial collapse followed by a plateau around $t/\tilde{\tau} = 1 \times 10^{-1}$ when the system forms a single compact aggregate and the self-sorting phase starts. At $t/\tilde{\tau} > 1 \times 10^{-1}$ for the single-species case $\delta = 1$, the MSD shows to remain constant at longer times, indicating that the aggregate is non-self-propelling and also its center of mass remains almost static, showing sub-diffusive transport. This behavior results from

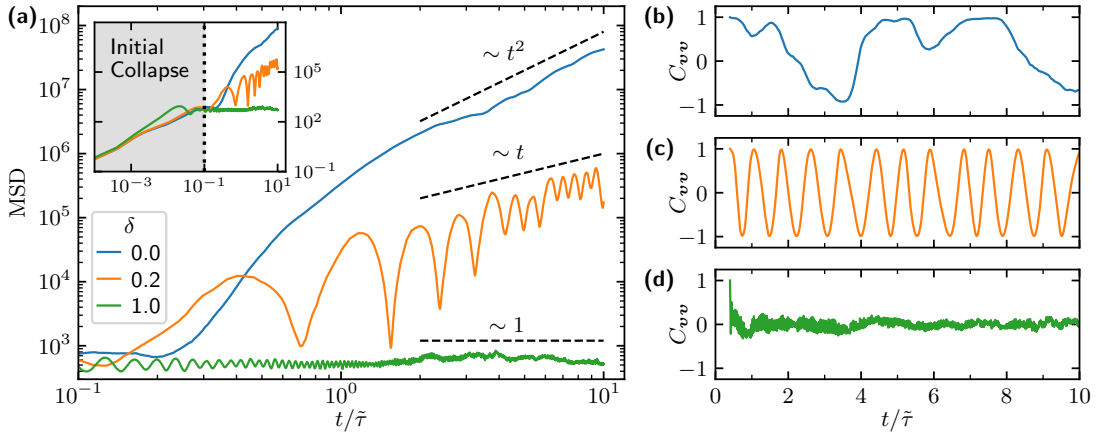

Figure 6.3: *Mean-squared displacement and normalized velocity auto-correlation of a mixture with molarity* δ. Time evolution of the (a) mean-squared displacement (MSD), and (b-d) normalized velocity auto-correlation $C_{\boldsymbol{vv}}$. For reference, cases corresponding to an equimolar mixture with $\delta = 0$, as well as a single-species system with $\delta = 1$ are shown. Inset shows data at short times $t/\tilde{\tau} < 1 \times 10^{-1}$ corresponding to the initial collapse.

a combination of effective attractions induced by orientation-dependent motility, and steric interactions preventing particles to overlap. Switching motility from passive to active, prevents particles in the aggregate's outer layer to diffuse out, but instead they rejoin when they reorient, as studied in Ch. 3. For the equimolar case $\delta = 0$, the MSD shows the swarm's motion is ballistic with MSD $\sim t^2$ in the long-time limit here considered. However, note that for much longer simulations, when the trajectory is able to explore a larger area, the behavior can become diffusive again. For the intermediate case $\delta = 0.2$, where the swarm describes a helical trajectory, the mean-squared displacement in the long-time limit is MSD $\sim t$ indicating diffusive transport. In this case, we observe oscillations of the MSD due to the circling motion of the swarm, which is superimposed to the drifting motion leading the MSD to increase over time.

To better characterize the swarm's circling motion we calculate the normalized velocity auto-correlation, defined as

$$C_{\boldsymbol{vv}}(t) = \frac{1}{N}\sum_{i=1}^{N} \hat{\boldsymbol{v}}_i(t) \cdot \hat{\boldsymbol{v}}_i(0) \tag{6.1}$$

where $\hat{\boldsymbol{v}}_i = \boldsymbol{v}_i/|\boldsymbol{v}_i|$ is the normalized physical velocity of particle i calculated from displacements as $\boldsymbol{v}(t) = [\boldsymbol{r}(t+\Delta t) - \boldsymbol{r}(t)]/\Delta t$ during a time interval of $\Delta t/\tilde{\tau} = 0.1$. This time interval should be large enough to reflect the behavior of the center of

mass trajectory, and disregard fluctuations given by small displacements due to random motion of individual passive particles, which occur mainly in the outer-layer. The velocity auto-correlation is $C_{\boldsymbol{vv}} = 1$ when the velocity vectors point in the same direction as in the initial time, $C_{\boldsymbol{vv}} = -1$ when they point in opposite directions, and $C_{\boldsymbol{vv}} = 0$ when they are perpendicular or randomized on average. We observe that for $\delta = 0$, $C_{\boldsymbol{vv}}$ shows a non-periodic fluctuating behavior, corresponding to the trajectory in Fig. 6.2a. For example, note that the minimum occurring at $t/(10^4\tau_B) \approx 3.5$ corresponds to the center of mass turning its direction of motion at that time. On the other hand, for $\delta = 1$, the velocity auto-correlation shows small amplitude fast fluctuations around $C_{\boldsymbol{vv}} = 0$, showing that the particle velocities decorrelate during the measurement interval $\Delta t/\tilde{\tau} = 0.1$. For $\delta = 0.2$, $C_{\boldsymbol{vv}}$ shows an almost perfect periodic behavior indicating that the trajectory performs a circular motion. Furthermore, from the peak-to-peak distance of the curve, we obtain that the average periodicity of the swarm's circling motion, which in this case happens to be $\tau_c \approx \tilde{\tau}$.

To investigate the transition from species-separated to non-species-separated with increasing δ, we calculate the center of mass normalized velocity u_c or *swarm speed* as defined in Eq. (5.2), which is calculated from center of mass displacements during a small time step of $\Delta t/\tilde{\tau} = 0.001$ and normalized by the particle's self-propulsion v_0. We know that when the system is non-separated the center of mass performs localized random-walk thus displacing a small amount and giving a small u_c. On the other hand, for separated cases the center of mass displaces over larger areas giving a larger u_c. Time evolution for some values of the molarity δ

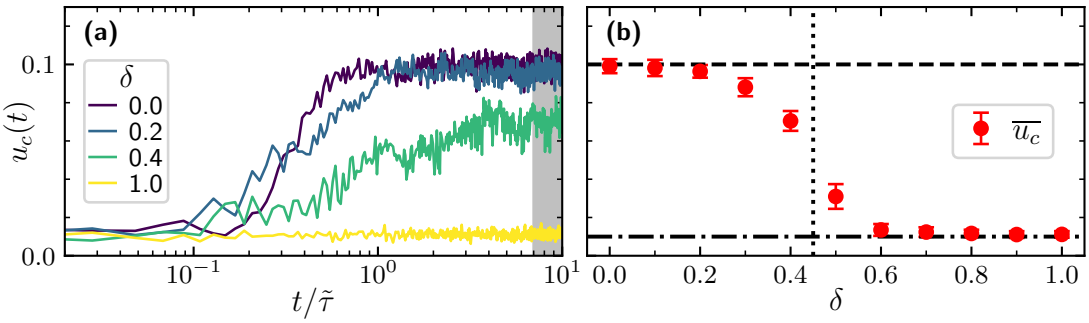

Figure 6.4: *Swarm speed u_c of mixtures with molarity δ.* (a) Time-evolution of the center of mass normalized velocity $u_c(t)$ (the *swarm speed*). Shaded region indicates steady-state. (b) Time-averaged steady-state swarm speed $\overline{u_c}$ for several values of δ. Dashed and dashed-dotted horizontal lines are a guide to the eye indicating values at $\overline{u_c} = 0.1$ and $\overline{u_c} = 0.01$, respectively. Dotted vertical line indicates the approximate critical value $\delta_c = 0.45$.

are shown in Fig. 6.4a. We observe that for $\delta = 0, 0.2$, the swarm speed increases and saturates at longer times with value $u_c \approx 0.1$. We observe a similar behavior for $\delta = 0.4$, but here the saturation occurs at smaller values $u_c \approx 0.07$. Time-averaged values in steady state, which we calculate at longer times $t/\tilde{\tau} > 7$, are shown in Fig. 6.4b. We observe that there is a smooth transition from motile with $\overline{u_c} \approx 0.1$ to non-motile with $\overline{u_c} \approx 0.01$, which is obtained with increasing molarity δ. The critical value of the transition is $\delta_c \approx 0.45$. The smaller values of the swarm speed we observe $\overline{u_c} \approx 0.01$ correspond to an aggregate that performs random walk motion, as shown in Fig. 6.2d-f.

6.2 Run-and-turn guided swarms

We have so far seen that different types of trajectories can be achieved within our system, i.e. either persistent straight trajectories, helical ones, or random walks, all of which depend on the molarity δ together with the other system parameters. This varied behavior can be useful to guide the swarm by externally manipulating the particle properties at a given instant of time t, then leaving the system to evolve and self-organize. This method does not require of any additional external force directly modifying the particle dynamics. Accordingly, various strategies can be designed to guide the swarm motion. One is to dynamically modify the particles species distribution to change their molarity δ depending on the type of trajectory we aim to achieve. For example, we can switch from a directed trajectory of an equimolar swarm with $\delta = 0$, to a helical trajectory of a swarm with $\delta = 0.2$. Changing the species distribution introduces an additional sorting step, which delays the dynamics. Once the system has separated, the direction of motion of the resulting separated swarm cannot be controlled in this case, as it comes from spontaneous symmetry breaking. A simpler strategy is to keep the species distribution over time, and only switch the misalignment angles between $\gamma_1 = -\gamma_2$ to $\gamma_1 = \gamma_2$, which corresponds to switching the collective behavior between directed swarms and rotating aggregates.

6.2.1 Mixing time

When misalignment angles are set to $\gamma_1 = \gamma_2$, the species-separated subdomains of the swarm remixes leading to an species-homogeneous aggregate. To test the time it takes the system to remix, we first consider a species-separated swarm which was formed after a simulation of an equimolar mixture $\delta = 0$ is completed. Here we take the configuration shown in Fig. 6.1a to be the starting point. Then, we set misalignment angles to be $\gamma_1 = \gamma_2 = \pi/4$ corresponding to a single-species

system, however we keep the particle type identifiers in order to see how the aggregate's species subdomains behave. We evolve the system during a time of $t/\tilde{\tau} = 20$. To quantify the mixing process, we calculate the time evolution of the species separation parameter $b_s(t)$ as defined in Eq. (5.1). Results are shown in Fig. 6.5. We observe the system performs a solid-body rotation in the counter-clockwise direction, as the aggregate rotates its shape changes from being slightly elongated at short times $t/\tilde{\tau} = 1 \times 10^{-2}$ with $b_s \approx 0.7$ (see Fig. 6.5a) with the species still separated, to circular and center separated while homogeneous in the outer-layer at $t/\tilde{\tau} = 1 \times 10^{-1}$ with $b_s \approx 0.3$ (see Fig. 6.5b). At even longer times, $t/\tilde{\tau} = 2 \times 10^{1}$, the system finally becomes species-homogeneous with $b_s \approx 0$ (see Fig. 6.5c). The behavior of $b_s(t)$ in Fig. 6.5d shows that the system remixes very fast initially at $t/\tilde{\tau} < 0.1$, then b_s decreases slowly following an approximate power law decay $b_s \sim t^{-0.25}$ which we obtained by fitting data in the time window $0.1 < t/\tilde{\tau} < 10$. At longer times $t/\tilde{\tau} > 10$, b_s drops to

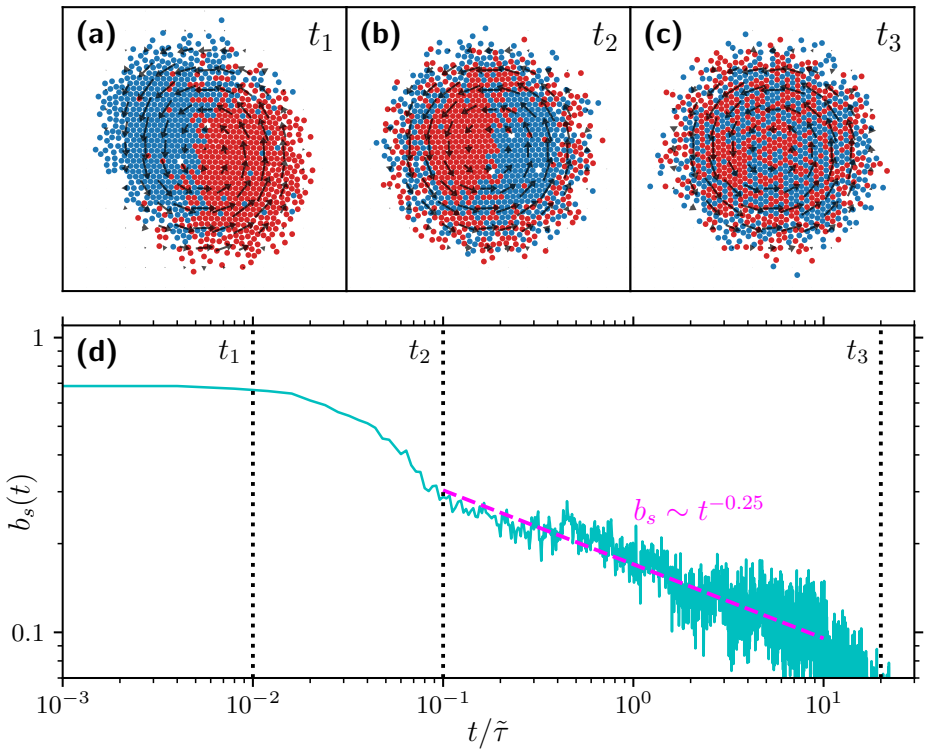

Figure 6.5: *Species mixing of a rotating aggregate.* (a-c) Snapshots showing the species mixing process. Snapshots are taken at times $t_i/\tilde{\tau} = 0.01, 0.1, 20$. Arrows indicate local velocity field. (d) Time evolution of the species separation parameter b_s. Vertical dotted lines indicate times of snapshots in (a).

small values below $b_s = 0.1$ indicating the system is fully mixed. The initial fast mixing process corresponds to particles in the outer-layer freely moving and rearranging their positions due to their circular motion when they are active, together with pure Brownian diffusion when they are passive. The slower mixing process corresponds to particles in the bulk being blocked from moving by others, due to the aggregate's internal crystalline structure, then it takes a significantly long time until particles in the bulk are able to move closer to the outer-layer.

6.2.2 Run-and-turn trajectories

One simple strategy to guide the swarm with precision is to keep the mixture equimolar while tuning only the species misalignment angles γ_1 and γ_2. We first consider system parameters $q^* = 0.7$ and $\gamma_1 = -\gamma_2 = \pi/4$. After the species-separated directed swarm has emerged, we change the misalignment of the particles to $\gamma_1 = \gamma_2$. When misalignment angles are set to $\gamma_1 = \gamma_2$, the system is not a mixture anymore since both species are now described by the same particle properties (same perception threshold q^* and misalignment angle γ). In this case, we know the system does not perform a directed motion anymore, but a solid-body rotation, as studied in Ch. 3 and Ch. 4. However, we can still keep track of individual particle types, such that each particle i still holds an identifier either 1 or 2. Next, we can switch back the particles misalignment angles to $\gamma_1 = -\gamma_2$, so the system again corresponds to an equimolar mixture performing directed motion. We say this procedure corresponds to a run-and-turn type of dynamics; *run* during some time τ_r when it has $\gamma_1 = -\gamma_2$, and *turn* for some time τ_r when it has $\gamma_1 = \gamma_2$. Note that this is related to a run-and-tumble motion [62], with the important difference that in our case we have control over the turn step, as we can choose the rotation direction to be either counter- or clockwise depending on the sign of the misalignment angle $\gamma_1 = \gamma_2$, and how large it will be turning τ_t

Snapshots of the system configuration during subsequent run and turn steps are shown in Fig. 6.6, illustrating how the system is able to reverse its direction of motion after one turn step. The turn duration here is $\tau_t/\tilde{\tau} = 0.03$, which is a very short time step such that the system does not remix into an species-homogeneous aggregate, as discussed in previous section. For the swarm to describe a significantly large straight trajectory, we need to choose the run step duration τ_r to be much larger than the turn duration τ_t. In this case we choose the run duration to be $\tau_r/\tilde{\tau} = 0.4$. Then, the run-and-turn procedure is repeated several times. Resulting center of mass trajectories of the swarm are shown in Fig. 6.7a. This trajectory shows that the motion of the swarm is confined due to the almost bouncing-back motion. By reducing the turn duration to a half, i.e. $\tau_t/\tilde{\tau} = 0.015$, the aggregate does not perform a half-rotation, but instead it deviates the direc-

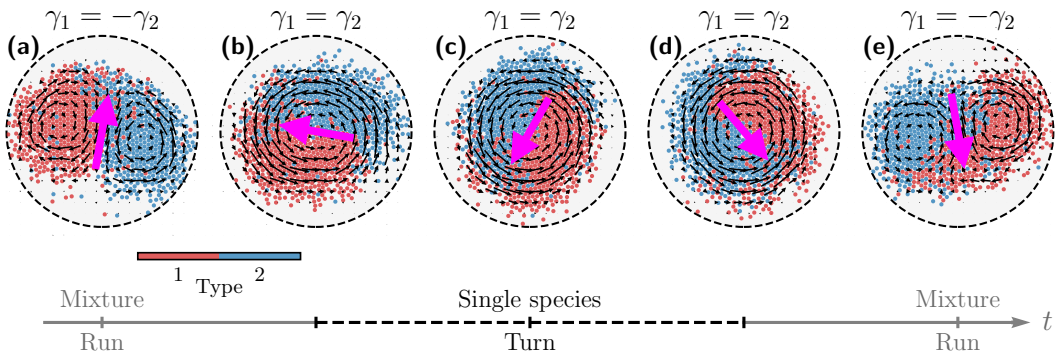

Figure 6.6: *Reversal of the direction of motion of a swarm.* Sequence of snapshots of a guided swarm configuration with (a) $\gamma_1 = -\gamma_2$, corresponding to a mixture phase where the swarm performs a *run*, i.e. directed motion; (b,c,d) $\gamma_1 = \gamma_2$, corresponding to a single-species phase, where the aggregate rotates in the counter-clockwise direction, corresponding to a *turn* of the swarm; then (e) $\gamma = -\gamma_2$ again. Small arrows indicate time-averaged coarsed-grained velocities. Large arrows are a guide to the eye to see the system's counter-clockwise rotation during the turning phase. Particles are color-coded by their type during the mixing phases.

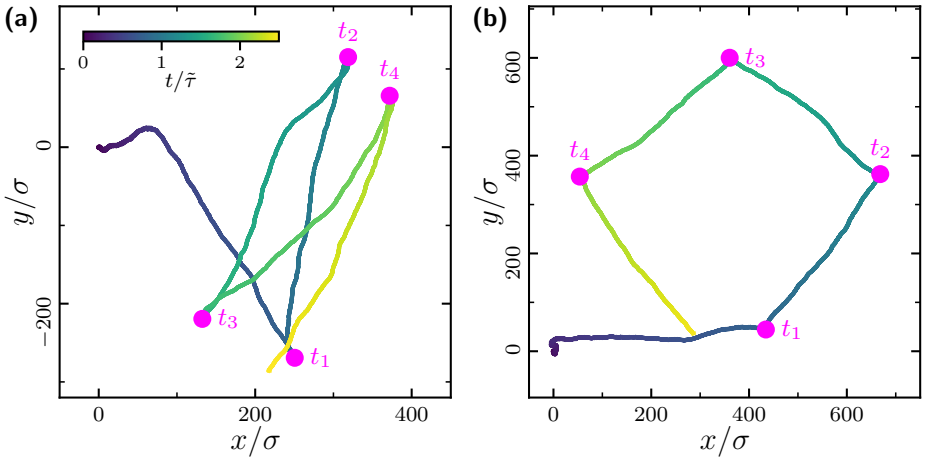

Figure 6.7: *Externally guided swarm trajectories.* Center of mass trajectories of a guided swarm with run step duration of $\tau_r/\tilde{\tau} = 0.4$, and turn step duration of (a) $\tau_t/\tilde{\tau} = 0.03$, and (b) $\tau_t/\tilde{\tau} = 0.015$. Labels $t_i/\tau_r \approx 1, 2, 3, 4$ indicate the instants after a run step τ_r, which is then followed by a short turn step τ_t.

tion of the swarm almost by approximately a 90 deg angle, leading to a trajectory that approximates a square shape, see Fig. 6.7b.

6.3 Summary

In this chapter we have explored two different strategies to guide a swarm of colloids with perception-dependent motility. First, we studied a non-equimolar mixture of particles consisting of N_1 particles with misalignment angle $\gamma_1 = \pi/4$, and N_2 particles with $\gamma_2 = -\pi/4$. We focused on the case with perception threshold $q^* = 0.7$, which leads to the emergence of a robust directed swarm for an equimolar mixture case $N_1 = N_2$. We found that the system separates into species subdomains for systems with molarities $\delta = 0, 0.2, 0.4$ (corresponding to species percentage ratios 50:50, 60:40, and 70:30, respectively). For $\delta = 0.2, 0.4$ we found that the center of mass of the non-equimolar swarm described helical trajectories, whereas for $\delta = 0$ the trajectory drifted in a given direction without helical motion. For larger molarity $\delta > 0.4$, trajectories describe a random walk. In fact, we found a smooth transition from motile to non-motile swarm, which we quantified by means of the normalized swarm velocity u_c; where we found the directed swarm speed was $\overline{u_c} \approx 0.1$ in steady state, whereas non-motile swarms showed $\overline{u_c} \approx 0.01$ corresponding to random walk motion. The critical molarity at which the transition takes place was determined to be approximately at $\delta_c = 0.45$. Furthermore, for $\delta = 0.2$ we found the swarm displays diffusive transport for the simulation time considered. We also characterized the helical motion of the center of mass of this case, by computing the velocity auto-correlation, showing an oscillating behavior of period $\tau_c \approx \tilde{\tau}$.

We also investigated a strategy that corresponds to externally guided motion obtained by dynamically tuning species misalignment angles γ_1 and γ_2. We achieved a run-and-turn type of dynamics for the directed swarm, by considering a long run step during which the system is equimolar, and a short turn step during which the misalignment angles was set to $\gamma_1 = \gamma_2$. We quantified the species remix during the turn step by means of the species separation parameter b_s. From here, we determined that the mixing time until the system becomes species-homogeneous is significantly long compared to the time it takes the aggregate to perform a single solid-body rotation. We only considered the case when the misalignment angle is positive during the turn step, thus we only observed rotating aggregates turning in the counter-clockwise direction, which introduced a bias in the direction of the swarm. Furthermore, by tuning duration of the tumbling step, we found that the trajectory can describe different types of patterns.

7 Conclusions and outlook

Different types of collective behaviors emerging in two dimensional systems of colloids with perception-dependent motility are here investigated mainly by means of particle-based numerical simulations. We consider colloids governed by Brownian dynamics with short-range repulsion accounting for volume exclusion. Furthermore, colloids are considered to perceive neighbours within a cone of vision of aperture half-angle $\alpha = \pi/4$. Then, the perception parameter was taken to be the inverse function of the interparticle distances $q_i \sim \sum_j (1/r_{ij})$, and the motility $v(q_i) = v_0\Theta(q_i - q^*)$ with $\Theta(\cdot)$ the Heaviside step function and q^* the perception threshold. We also consider the cone of vision to be *misaligned* an angle γ with respect to the self-propulsion direction of motion $\boldsymbol{e}$. Colloidal suspensions described by this simple model display a rich variety of dynamical and structural properties for different system parameters.

In Ch. 3, we considered single-species systems of colloids at fixed γ and q^*. Starting from a homogeneously distributed and diluted circular configuration, the colloids aggregate into a single cohesive and rotating circular cluster. We explained this behavior by means of perception radial profiles, which showed that colloids display an orientation-dependent motility translating into an effective attractive force and net torque exerted on the aggregate. For the circular aggregate, particle density increases towards the center of mass, such that when a particle's vision cone points towards the aggregate's center it perceives a large number of neighbors and becomes active, remaining passive otherwise. Cohesion was then found to emerge from the motility imbalance between active *in-oriented* particles, i.e particles with $\hat{\boldsymbol{r}} \cdot \boldsymbol{e} = -1$, and passive *out-oriented* ones, i.e. particles with $\hat{\boldsymbol{r}} \cdot \boldsymbol{e} = 1$. On the other hand, rotation was found to emerge from the vision cone misalignment, as tangentially oriented colloids with a vision cone co-oriented with the aggregate's center of mass were found to drive the system to rotate, whereas anti-oriented ones were found to remain passive and dragged by actives when located within the bulk. Furthermore, we obtained a value of the perception threshold leading to the formation of *compact aggregates* that showed an hexagonal close-packed internal structure, as well as an homogeneous activity distribution. This value of the perception threshold was later employed as a normalization factor, such that $q^* = 1$ and $\gamma = \pi/4$ were considered to be the standard parameters. For systems of $N = 1000$ particles at $q^* = 1$ and $\gamma = \pi/4$,

we found the radius of gyration of compact aggregates to be $\overline{R_g} \approx 13\sigma$ with σ the particle diameter, and the average hexatic order $\overline{\Psi_6} \approx 0.75$ (smaller than unity due to the presence of the outer-layer). Finally, we characterized the system dynamics for parameters $q^* = 1$ and varying γ by means of the radius of gyration $R_g(t)$, and the rotational order $O_R(t)$ obtained from the velocity field $\boldsymbol{v}$—calculated from particle displacements, not from self-propulsion $v_0\boldsymbol{e}$ which is isotropic due to rotational diffusion. We obtained that R_g diverges for systems of particles with lateral visual perception $\gamma = \pi/2$, and it is minimum with $\overline{R_g} \approx 13\sigma$ for $\gamma = 0$. The rotational order O_R showed a non-monotonous behavior with maximum value of $\overline{O_R} \approx 0.8$ at $\gamma = \pi/4$ and vanishing both at $\gamma = 0$ and $\gamma = \pi/2$.

In Ch. 4 we focused on the structural properties of the aggregates. For this we obtained radial profiles for the density $\rho(r)$, angular velocity $\omega(r)$, and polarization components both in the radial $p_r(r)$ and tangential $p_t(r)$ directions with respect to the center of mass $\boldsymbol{r}_{\rm cm}$. At $q^* = 1$ and $0 < \gamma/\pi \leq 0.375$, we found $\rho(r)$ plateau near the origin, then shows a soft decay towards the outer-layer vanishing at larger radial distances r where no particles are found. From $\rho(r)$ we extracted the aggregate's size R, bulk density ρ_b, and interface width δ. With increasing γ, we obtained constant values of $\rho_b \approx \rho_c$ and $R \approx R_c$, where $\rho_c \approx 0.63\sigma^{-2}$ and $R_c \approx 22.37\sigma$ correspond to the bulk density and size of a compact aggregate. The interface width δ showed to monotonously increase with γ from $\delta \approx 1.5R_c$ at $\gamma/\pi = 0$, to $\delta \approx 0.3$ at $\gamma/\pi = 0.375$. We also obtained the active and passive contributions to the radial profiles, showing that the system's activity distribution remains homogeneous in this case. Both the radial polarization of the passives $p_r^p(r)$ and tangential polarization of the actives $p_t^a(r)$ showed to be always positive, whereas $p_r^a(r)$ and $p_t^p(r)$ showed only negative values. Such polarization imbalance was determined to be a consequence of the orientation-dependent motility behavior explained in Ch. 3. Profiles $\omega(r)$ showed to plateau giving a bulk angular velocity ω_b that significantly increased with γ; showing a minimum of $\omega_b = 0$ at $\gamma/\pi = 0$ and a maximum of $\omega_b \approx 0.6$ at $\gamma/\pi = 0.375$. At $q^* = 1$ and near lateral perception $0.4 < \gamma/\pi < 0.5$, the density radial profile $\rho(r)$ showed a much broader interface without a plateau to extract ρ_b, instead a maximum near the center with $\rho(0) \approx \rho_c$ appear then a monotonous decay with increasing radial distances. For values very close to $\gamma/\pi = 0.5$, namely for $\gamma/\pi = 0.46, 0.47$, we found that the system is not cohesive anymore, as in those cases the motility imbalance between in- and out-oriented particles does not hold, i.e. either in- or out-oriented particles can activate with almost same probability. In this case, $\omega(r)$ showed again a very broad interface, with a maximum that decreases from $\omega(0) \approx 0.7\omega_c$ at $\gamma/\pi \approx 0.4$, to $\omega(0.2R_c) \approx 0.4\omega_c$ at $\gamma/\pi = 0.45$. Furthermore, at fixed γ we found that the activity distribution dramatically changes with varying q^*. For $\gamma = \pi/4$ and a low value of the perception threshold $q^* = 0.3$, we found an aggregate that was

mainly active with only a few passives in the outer layer. The radial profile $\rho(r)$ showed a more dilute bulk density of $\rho_b \approx 0.75\rho_c$ compared to the compact case with $\rho_b \approx \rho_c$, while its size remained almost the same giving $R \approx R_c$. Profile $\omega(r)$ showed a non-monotonous behavior with maximum value $\omega(R_c) \approx 0.2\omega_c$ at the interface $r = R_c$, and vanishing both at the origin and larger distances r. This demonstrated that the dilute aggregate emerging at $q^* = 0.3$ rotates only in the outer layer where both actives and passives coexist. We explained this behavior by means of perception radial profiles $q(r)$ showing that within the bulk particles are active regardless of their orientation, while in the outer layer only in- and co-oriented ones can activate. For $q^* = 0.7$, the system was also found to be mostly active, however the aggregate was found to be compact as here passives in the outer layer exist in a broader range of radial distances $0.1 < r/R_c < 1$. In this case, the bulk angular velocity was found to be $\omega_b \approx 0.3\omega_c$. For $q^* = 1.2$ we found the system again forms a compact aggregate, but here it was mostly passive with only a few actives driving aggregate's rotation with $\omega_b \approx 0.2\omega_c$ while keeping it compact with $\rho_b \approx \rho_c$ and $R \approx R_c$. In conclusion, the bulk's angular velocity was found to be a non-monotonous function of the perception threshold q^*, which was found to modify the activity distribution. Finally, we derived analytical expressions from conservation equations for the density and particle flux. For this, we considered a continuum description corresponding to a solid-body rotation driven by activity at the interface. We found a satisfactory agreement between theory and numerical results for the bulk density ρ_b, size R, and bulk angular velocity ω_b of the aggregates as a function of the parameters γ and q^*. Mismatch between theory and simulations was found for ω_b at larger values of γ, where $\rho(r)$ does not plateau near the origin. Besides, to consider changes in motility distribution, we employed a fit parameter D_{eff} accounting for an effective diffusion that increases with increasing number of actives within the bulk.

In Ch. 5, we considered a binary mixture of particles with misalignment angle $\gamma_1 = -\gamma_2$. For standard parameters $q^* = 1$ and $\gamma_1 = -\gamma_2 = \pi/4$, we found that the system self-organizes into a single species-separated directed swarm. The system's dynamical behavior is characterized by means of the largest cluster size n_c, species separation b_s, fraction of active particles n_a, and swarm's normalized velocity u_c. At short times $t/\tilde{\tau} < 1$, where $\tilde{\tau} = 10^4\tau_B$ with τ_B the particle's ballistic time, we found that the system first aggregates into a cohesive species-homogeneous cluster which later self-sorts into two well-defined species subdomains showing an increase of both $b_s(t)$ and $u_c(t)$ until a time $t/\tilde{\tau} = 1$ when they reach a maximum of $b_s \approx 0.7$ and $u_c \approx 0.1$, respectively. During this regime the largest cluster size remains constant with $n_c \approx 1$ as the system is cohesive, besides the fraction of actives remains $n_a \approx 0.35$. At longer times $t/\tilde{\tau} > 1$ the system starts leaving a trail of particles behind, thus dissolving over time and

showing a monotonous decrease of all dynamic parameters that eventually vanish at $t/\tilde{\tau} > 3.5$. For a lower value of the perception threshold, namely $q^* = 0.7$, we found that the system forms a robust directed swarm, which remains cohesive over time showing steady-state values $n_c \approx 1$, $n_a \approx 0.5$, $b_s \approx 0.7$, and $u_c \approx 0.1$. In this case, particles at the outer layer far from the center are not left behind in a trail, as with smaller threshold value q^* they easily reactivate and quickly rejoin the swarm. We characterized the bean shape of the swarm for systems with $q^* = 0.7$ and varying values of the misalignment angle $\gamma/\pi \in (0.15, 0.35)$, showing the swarm's asphericity λ and bean aperture angle β to linearly increase with γ. For $q^* = 0.3$ and $\gamma = \pi/4$, we found the system forms a loose and non-separated aggregate that does not self-propel. Dynamic parameters in this case remain constant, giving $n_c \approx 1$, $n_a \approx 0.75$, $b_s = 0$, and $u_c = 0$, the particles are active in the center regardless of their orientation, which prevents particles to be dragged and kept together in close packing, nor they are able to separate into species subdomains. To complete the picture, we performed simulations for different values of q^* and γ and obtained a phase diagram showing regions where the system is either cohesive separated, cohesive non-separated, or non-cohesive non-separated.

In Ch. 6, we studied cases when the mixture is non-equimolar, which we found can lead to cohesive species-separated swarms that describe helical trajectories. We found a transition between motile and non-motile swarm with increasing molarity δ, showing a maximum of $u_c \approx 0.1$ in the equimolar case $\delta = 0$ and vanishing in the single-species case $\delta = 1$; the transition was found to occur approximately at $\delta = 0.45$. We also characterized the dynamical behavior of non-equimolar swarms, for which we calculated the mean-squared displacement (MSD) and velocity autocorrelation function $C_{\boldsymbol{vv}}$. The MSD showed non-equimolar swarms perform diffusive transport in the long-time limit, while describing a helical trajectory with circling period of $\tau_h/\tilde{\tau} \approx 1$. Finally, we showed a simple strategy to externally guide a swarm, which we obtained by switching the misalignment angles between $\gamma_1 = \gamma_2$ and $\gamma_1 = -\gamma_2$. We found this simple rule translates into consecutive run-and-turn motions of the swarm, allowing to describe different types of guided trajectories. The exact path followed by the trajectories was found to be dependent on the turn step τ_t, such that smaller values of τ_t determine the swarm's turning angle θ_t between two consecutive straight motions. To implement this strategy more accurately, one could quantify the dependence $\theta_t(\tau_t)$ which would allow us to choose the appropriate duration of the time step corresponding to a specific trajectory.

The model investigated in this thesis can be easily implemented in experiments of light activated colloids employing an external feedback loop to account for anisotropic interactions [41, 45, 180]. Rotating aggregates and directed swarms

have been recently achieved in these type of experiments [44, 107]. However, they require an involved alignment interaction mechanism demanding a high degree of control in the experiments. One advantage of our model is that it does not consider local torques on each colloid, so the only ingredient required in experiments is a mechanism to account for the anisotropic interactions together with individual activation of the colloids. Throughout the thesis, we have employed systems of $N = 1000$ particles, which can be a somewhat large number to control in experiments. While smaller N could affect the structural properties of the emergent collective behaviors, we know orientation-dependent motility inducing rotations and species-separation are generic mechanisms and therefore smaller systems should still display collective behaviors explored in this thesis. System parameters that could be also further studied is the effect of the Péclet number, for example by considering particles that switch their motility between fast and slow; the effect of the vision cone aperture angle α, and the softness of the repulsive potential. One interesting direction to study employing our model is to consider the effect of confinement, which is known to have a significant impact on the collective behavior of systems of active particles [8, 185–192]. For example, we could add a motility rule that account for swarm avoidance of walls, in this way we could further guide the overall motion. Another interesting ingredient to consider is the effect of hydrodynamic interactions, which can modify the cohesion and structure of colloidal aggregates [84, 193, 194]. In the case of a single-species system of colloids with misaligned perception-dependent motility, this can also strongly affect the aggregate's rotation speed. For binary mixtures, we have proposed one straightforward strategy to control the center of mass trajectory of directed swarms by dynamically tuning particle parameters. In recent years, several examples of self-organization and collective goal-achievement strategies have been studied in systems of active particles by employing reinforcement learning techniques [195–201]. Such methodology could be included in our model, for example by considering colloids that learn how to tune the misalignment angle γ in order to achieve desired types of collective behaviors and self-guide its overall motion.

Bibliography

[1]M. Kardar, *Statistical Physics of Particles* (Cambridge University Press, 2007).

[2]M. Kardar, *Statistical Physics of Fields* (Cambridge University Press, 2007).

[3]I. Prigogine, *Non-equilibrium statistical mechanics* (Courier Dover Publications, 2017).

[4]G. Gompper et al., "The 2020 motile active matter roadmap", J. Phys.: Condens. Matter **32**, 193001 (2020).

[5]M. J. Bowick et al., "Symmetry, Thermodynamics, and Topology in Active Matter", Phys. Rev. X **12**, 010501 (2022).

[6]S. Ramaswamy et al., "Active nematics on a substrate: Giant number fluctuations and long-time tails", EPL **62**, 196 (2003).

[7]T. Vicsek and A. Zafeiris, "Collective motion", Phys. Rep. **517**, 71–140 (2012).

[8]C. Bechinger et al., "Active Particles in Complex and Crowded Environments", Rev. Mod. Phys. **88**, 045006 (2016).

[9]B. Liebchen and H. Löwen, "Synthetic Chemotaxis and Collective Behavior in Active Matter", Acc. Chem. Res. **51**, 2982–2990 (2018).

[10]Y. Fu et al., "Microscopic Swarms: From Active Matter Physics to Biomedical and Environmental Applications", Micromachines **13**, 295 (2022).

[11]K. Tunstrøm et al., "Collective States, Multistability and Transitional Behavior in Schooling Fish", PLoS Comput. Biol. **9**, e1002915 (2013).

[12]M. Ballerini et al., "Interaction ruling animal collective behavior depends on topological rather than metric distance: Evidence from a field study", PNAS **105**, 1232–1237 (2008).

[13]L. Gómez-Nava et al., "Intermittent collective motion in sheep results from alternating the role of leader and follower", Nat. Phys. **18**, 1–8 (2022).

[14]A. Attanasi et al., "Collective Behaviour without Collective Order in Wild Swarms of Midges", PLOS Comput. Biol. **10**, e1003697 (2014).

[15]I. S. Aranson, "Bacterial active matter", Rep. Prog. Phys. **85**, 076601 (2022).

[16]G. H. Koenderink et al., "An active biopolymer network controlled by molecular motors", PNAS **106**, 15192–15197 (2009).

[17]J. Elgeti et al., "Hydrodynamics of sperm cells near surfaces", Biophysical journal **99**, 1018–1026 (2010).

[18]H. R. Vutukuri et al., "Light-switchable propulsion of active particles with reversible interactions", Nat. Commun. **11**, 2628 (2020).

[19]J. R. Gomez-Solano et al., "Transient coarsening and the motility of optically heated Janus colloids in a binary liquid mixture", Soft Matter **16**, 8359–8371 (2020).

[20]B. Zhang et al., "Reconfigurable emergent patterns in active chiral fluids", Nat. Commun. **11**, 4401 (2020).

[21]A. Bricard et al., "Emergent vortices in populations of colloidal rollers", Nat. Commun. **6**, 7470 (2015).

[22]T. Kawai et al., "Degenerate states, emergent dynamics and fluid mixing by magnetic rotors", Soft Matter **16**, 6484–6492 (2020).

[23]G. Junot et al., "Collective hydrodynamic transport of magnetic microrollers", Soft Matter **17**, 8605–8611 (2021).

[24]H. Carstensen et al., "Self-assembly and percolation in two dimensional binary magnetic colloids", Soft Matter **18**, 6222–6228 (2022).

[25]J. Yu et al., "Pattern generation and motion control of a vortex-like paramagnetic nanoparticle swarm", Int. J. Robotics Res. **37**, 912–930 (2018).

[26]H. Xie et al., "Reconfigurable magnetic microrobot swarm: Multimode transformation, locomotion, and manipulation", Sci. Robot. **4**, `10.1126/scirobotics.aav8006` (2019).

[27]M. Dorigo et al., "Swarm Robotics: Past, Present, and Future [Point of View]", Proc. IEEE **109**, 1152–1165 (2021).

[28]H. Hussein et al., "Actuation of Mobile Microbots: A Review", Adv. Intell. Syst. **n/a**, 2300168 (2023).

[29]Z. Yu et al., "Swarming magnetic photonic-crystal microrobots with on-the-fly visual pH detection and self-regulated drug delivery", InfoMat **n/a**, e12464 (2023).

[30]Y. Hou et al., "A review on microrobots driven by optical and magnetic fields", Lab Chip **23**, 848–868 (2023).

[31]T. Armstrong-Sly, *Starling Roost*, 2011, `https://www.flickr.com/photos/tonyarmstrong/5381370808`.

[32]T. C. Schneirla and G. Piel, "THE ARMY ANT", Sci. Am. **178**, 16–23 (1948).

[33]M. C. Marchetti et al., "Hydrodynamics of soft active matter", Rev. Mod. Phys. **85**, 1143–1189 (2013).

[34]D. Needleman and Z. Dogic, "Active matter at the interface between materials science and cell biology", Nat. Rev. Mater. **2**, 17048 (2017).

[35]W. Wang et al., "The impact of individual perceptual and cognitive factors on collective states in a data-driven fish school model", PLoS Comput. Biol. **18**, e1009437 (2022).

[36]W. Wang et al., "Dynamic and programmable self-assembly of micro-rafts at the air-water interface", Sci. Adv. **3**, e1602522 (2017).

[37]L. G. Nava et al., "A novel approach to chemotaxis: Active particles guided by internal clocks", EPL **130**, 68002 (2020).

[38]S. Ceron et al., "Programmable self-organization of heterogeneous microrobot collectives", Proc. Natl. Acad. Sci. **120**, e2221913120 (2023).

[39]A. M. Stevens and E. P. Greenberg, "Quorum sensing in vibrio fischeri: essential elements for activation of the luminescence genes", J. Bacteriol. **179**, 557–562 (1997).

[40]C. Abaurrea Velasco et al., "Collective behavior of self-propelled rods with quorum sensing", Phys. Rev. E **98**, 022605 (2018).

[41]T. Bäuerle et al., "Self-organization of active particles by quorum sensing rules", Nat. Commun. **9**, 3232 (2018).

[42]L. Barberis and F. Peruani, "Large-Scale Patterns in a Minimal Cognitive Flocking Model: Incidental Leaders, Nematic Patterns, and Aggregates", Phys. Rev. Lett. **117**, 248001 (2016).

[43]R. S. Negi et al., "Emergent collective behavior of active Brownian particles with visual perception", Soft Matter **18**, 6167–6178 (2022).

[44]T. Bäuerle et al., "Formation of stable and responsive collective states in suspensions of active colloids", Nat. Commun. **11**, 2547 (2020).

[45]F. A. Lavergne et al., "Group formation and cohesion of active particles with visual perception–dependent motility", Science **364**, 70–74 (2019).

[46]J. K. G. Dhont, *An Introduction to Dynamics of Colloids*, Studies in Interface Science 2 (Elsevier, Academic Press, 1996).

[47]H. Risken and T. Frank, *The Fokker-Planck equation: methods of solution and applications*, 2nd, Springer Series in Synergetics (Springer, 1996).

[48]R. Zwanzig, *Nonequilibrium statistical mechanics*, 1st ed. (Oxford University Press, 2001).

[49]R. Brown, "Xxvii. a brief account of microscopical observations made in the months of june, july and august 1827, on the particles contained in the pollen of plants; and on the general existence of active molecules in organic and inorganic bodies", The philosophical magazine **4**, 161–173 (1828).

[50]A. Einstein et al., "On the motion of small particles suspended in liquids at rest required by the molecular-kinetic theory of heat", Annalen der physik **17**, 208 (1905).

[51]R. Newburgh et al., "Einstein, perrin, and the reality of atoms: 1905 revisited", Am. J. Phys. **74**, 478–481 (2006).

[52]S. G. Brush, "A history of random processes: i. brownian movement from brown to perrin", Archive for history of exact sciences **5**, 1–36 (1968).

[53]J. Perrin, *Brownian movement and molecular reality* (Courier Corporation, 2013).

[54]K. Sekimoto, "Langevin equation and thermodynamics", Prog. Theor. Phys. Supp. **130**, 17–27 (1998).

[55]J. Weber, "Fluctuation dissipation theorem", Physical Review **101**, 1620 (1956).

[56]R. Kubo, "The fluctuation-dissipation theorem", Rep. Prog. Phys. **29**, 255 (1966).

[57]J. T. Edward, "Molecular volumes and the stokes-einstein equation", J. Chem. Educ. **47**, 261 (1970).

[58]L. D. Landau and E. M. Lifshitz, *Fluid Mechanics: Landau and Lifshitz: Course of Theoretical Physics, Volume 6* (Elsevier, 2013).

[59]J. O'Byrne et al., "Time irreversibility in active matter, from micro to macro", Nat. Rev. Phys. **4**, 167–183 (2022).

[60]E. M. Purcell, "Life at low Reynolds number", Am. J. Phys. **45**, 10 (1977).

[61]P. Romanczuk et al., "Active brownian particles: from individual to collective stochastic dynamics", The European Physical Journal Special Topics **202**, 1–162 (2012).

[62]A. P. Solon et al., "Active brownian particles and run-and-tumble particles: A comparative study", Eur. Phys. J. Spec. Top. **224**, 1231–1262 (2015).

[63]H. Margenau, "Van der waals forces", Rev. Mod. Phys. **11**, 1 (1939).

[64]J. C. Slater and J. G. Kirkwood, "The van der waals forces in gases", Phys. Rev. **37**, 682 (1931).

[65]J. Bialké et al., "Microscopic theory for the phase separation of self-propelled repulsive disks", EPL **103**, 30008 (2013).

[66]I. Buttinoni et al., "Dynamical Clustering and Phase Separation in Suspensions of Self-Propelled Colloidal Particles", Phys. Rev. Lett. **110**, 238301 (2013).

[67]C. B. Caporusso et al., "Motility-Induced Microphase and Macrophase Separation in a Two-Dimensional Active Brownian Particle System", Phys. Rev. Lett. **125**, 178004 (2020).

[68]M. E. Cates and J. Tailleur, "Motility-Induced Phase Separation", Annu. Rev. Condens. Matter Phys. **6**, 219–244 (2015).

[69]E. Chacon et al., "Intrinsic structure perspective for MIPS interfaces in two dimensional systems of Active Brownian Particles", Soft Matter **18**, 10.1039/D1SM01493E (2022).

[70]Y. Fily and M. C. Marchetti, "Athermal Phase Separation of Self-Propelled Particles with No Alignment", Phys. Rev. Lett. **108**, 235702 (2012).

[71]F. Ginot et al., "Aggregation-fragmentation and individual dynamics of active clusters", Nat. Commun. **9**, 1–9 (2018).

[72]G. Gonnella et al., "Motility-induced phase separation and coarsening in active matter", Comptes Rendus Physique **16**, 316–331 (2015).

[73]J. Martin-Roca et al., "Characterization of MIPS in a suspension of repulsive active Brownian particles through dynamical features", J. Chem. Phys. **154**, 164901 (2021).

[74]G. S. Redner et al., "Reentrant phase behavior in active colloids with attraction", Phys. Rev. E **88**, 012305 (2013).

[75]G. S. Redner et al., "Structure and Dynamics of a Phase-Separating Active Colloidal Fluid", Phys. Rev. Lett. **110**, 055701 (2013).

[76]J. T. Siebert et al., "Phase behavior of active Brownian disks, spheres, and dimers", Soft Matter **13**, 1020–1026 (2017).

[77]J. T. Siebert et al., "Critical behavior of active Brownian particles", Phys. Rev. E **98**, 030601 (2018).

[78]A. P. Solon et al., "Generalized thermodynamics of motility-induced phase separation: phase equilibria, Laplace pressure, and change of ensembles", New J. Phys. **20**, 075001 (2018).

[79]J. Stenhammar et al., "Phase behaviour of active Brownian particles: the role of dimensionality", Soft Matter **10**, 1489–1499 (2014).

[80]T. Speck et al., "Dynamical mean-field theory and weakly non-linear analysis for the phase separation of active Brownian particles", J. Chem. Phys. **142**, 224109 (2015).

[81]J. W. Cahn, "On spinodal decomposition", Acta metallurgica **9**, 795–801 (1961).

[82]E. Favvas and A. C. Mitropoulos, "What is spinodal decomposition", J. Eng. Sci. Technol. Rev **1**, 25–27 (2008).

[83]A. Zöttl and H. Stark, "Hydrodynamics Determines Collective Motion and Phase Behavior of Active Colloids in Quasi-Two-Dimensional Confinement", Phys. Rev. Lett. **112**, 118101 (2014).

[84]S. Roca-Bonet et al., "Clustering of self-thermophilic asymmetric dimers: the relevance of hydrodynamics", Soft Matter **18**, 7741–7751 (2022).

[85]T. E. Will, "Flock leadership: understanding and influencing emergent collective behavior", The Leadership Quarterly **27**, 261–279 (2016).

[86]A. Cavagna et al., "The physics of flocking: Correlation as a compass from experiments to theory", Phys. Rep. **728**, 1–62 (2018).

[87]T. Vicsek et al., "Novel Type of Phase Transition in a System of Self-Driven Particles", Phys. Rev. Lett. **75**, 1226–1229 (1995).

[88]C. W. Reynolds, "Flocks, herds and schools: a distributed behavioral model", in Proceedings of the 14th annual conference on computer graphics and interactive techniques (1987), pp. 25–34.

[89]J. A. Acebrón et al., "The Kuramoto model: A simple paradigm for synchronization phenomena", Rev. Mod. Phys. **77**, 137–185 (2005).

[90]Y. Kuramoto, "Cooperative Dynamics of Oscillator Community: A Study Based on Lattice of Rings", Prog. Theor. Phys. **79**, 223–240 (1984).

[91]S. H. Strogatz, "From Kuramoto to Crawford: exploring the onset of synchronization in populations of coupled oscillators", Physica D: Nonlinear Phenomena **143**, 1–20 (2000).

[92]Y. Kuramoto and D. Battogtokh, "Coexistence of Coherence and Incoherence in Nonlocally Coupled Phase Oscillators", ArXivcond-Mat0210694 (2002).

[93]M. Suzuki, "Relationship among exactly soluble models of critical phenomena. i: 2d ising model, dimer problem and the generalized xy-model", Prog. Theor. Phys. **46**, 1337–1359 (1971).

[94]C. Lupp and E. G. Ruby, "Vibrio fischeri Uses Two Quorum-Sensing Systems for the Regulation of Early and Late Colonization Factors", J. Bacteriol. **187**, 3620–3629 (2005).

[95]Y.-H. Dong and L.-H. Zhang, "Quorum sensing and quorum-quenching enzymes", J. Microbiol. **43**, 101–109 (2005).

[96]J. E. González and N. D. Keshavan, "Messing with bacterial quorum sensing", Microbiol. Mol. Biol. Rev. **70**, 859–875 (2006).

[97]S. P. Diggle et al., "Quorum sensing", Curr. Biol. **17**, R907–R910 (2007).

[98]M. Rein et al., "Collective Behavior of Quorum-Sensing Run-and-Tumble Particles under Confinement", Phys. Rev. Lett. **116**, 058102 (2016).

[99]A. Fischer et al., "Quorum-sensing active particles with discontinuous motility", Phys. Rev. E **101**, 012601 (2020).

[100]J. Singh and A. V. A. Kumar, "Phase separation in a two-dimensional binary colloidal mixture by quorum sensing activity", Phys. Rev. E **101**, 022606 (2020).

[101]F. Jose et al., "A phase separation of active colloidal suspension via Quorum-sensing", Soft Matter **17**, 3153–3161 (2021).

[102]N. F. Britton et al., *Reaction-diffusion equations and their applications to biology.* (Academic Press, 1986).

[103]H. Risken, *The Fokker-Planck Equation: Methods of Solution and Applications*, 1st (Springer-Verlag, Berlin Heidelberg New York Tokyo, 1984).

[104]John David Jackson, *Classical Electrodynamics, 2nd Edition* (1975).

[105]J. K. G. Dhont et al., "Motility-induced inter-particle correlations and dynamics: a microscopic approach for active Brownian particles", Soft Matter **17**, 5613–5632 (2021).

[106]J. Bickmann and R. Wittkowski, "Predictive local field theory for interacting active Brownian spheres in two spatial dimensions", J. Phys.: Condens. Matter **32**, 214001 (2020).

[107]C.-J. Chen and C. Bechinger, "Collective response of microrobotic swarms to external threats", New J. Phys. **24**, 033001 (2022).

[108]S. Plimpton, "Fast parallel algorithms for short-range molecular dynamics", J. Comput. Phys. **117**, 1–19 (1995).

[109]A. P. Thompson et al., "Lammps-a flexible simulation tool for particle-based materials modeling at the atomic, meso, and continuum scales", Comput. Phys. Commun. **271**, 108171 (2022).

[110]D. Van Der Spoel et al., "Gromacs: fast, flexible, and free", J. Comput. Chem. **26**, 1701–1718 (2005).

[111]W. Van Gunsteren and H. Berendsen, "Algorithms for brownian dynamics", Molecular Physics **45**, 637–647 (1982).

[112]M. P. Allen and D. J. Tildesley, *Computer Simulation of Liquids: Second Edition*, 2nd ed. (Oxford University Press, Oxford, 2017).

[113]P. E. Kloeden et al., *Stochastic differential equations* (Springer, 1992).

[114]N. G. V. Kampen, *Stochastic Processes in Physics and Chemistry* (Elsevier, 2011).

[115]P. E. Kloeden and E. Platen, "Higher-order implicit strong numerical schemes for stochastic differential equations", J. Stat. Phys. **66**, 283–314 (1992).

[116]L. Caprini et al., "Hidden velocity ordering in dense suspensions of self-propelled disks", Phys. Rev. Res. **2**, 023321 (2020).

[117]P. Baconnier et al., "Selective and collective actuation in active solids", Nat. Phys. **18**, 1–6 (2022).

[118]E. S. Bililign et al., "Motile dislocations knead odd crystals into whorls", Nat. Phys. **18**, 212–218 (2022).

[119]Y.-E. Keta et al., "Disordered Collective Motion in Dense Assemblies of Persistent Particles", Phys. Rev. Lett. **129**, 048002 (2022).

[120]D. M. Lobmeyer and S. L. Biswal, "Grain boundary dynamics driven by magnetically induced circulation at the void interface of 2D colloidal crystals", Sci. Adv. **8**, eabn5715 (2022).

[121]P. Digregorio et al., "Unified analysis of Topological Defects in 2D systems of Active and Passive disks", Soft Matter **18**, 566–591 (2021).

[122]L. Bonn et al., "Fluctuation-induced dynamics of nematic topological defects", Phys. Rev. E **106**, 044706 (2022).

[123]Y. Rouzaire and D. Levis, "Dynamics of topological defects in the noisy Kuramoto model in two dimensions", Front. Phys. **10** (2022).

[124]Y.-E. Keta et al., "Intermittent relaxation and avalanches in extremely persistent active matter", Soft Matter **19**, 3871–3883 (2023).

[125]N. Ramrattan et al., "A corresponding-states framework for the description of the mie family of intermolecular potentials", Molecular Physics **113**, 932–947 (2015).

[126]H. Watanabe et al., "Phase diagram and universality of the Lennard-Jones gas-liquid system", J. Chem. Phys. **136**, 204102 (2012).

[127]S. Stephan et al., "Review and comparison of equations of state for the lennard-jones fluid", Fluid Phase Equilibria **523**, 112772 (2020).

[128]D. M. Heyes and H. Okumura, "Equation of state and structural properties of the weeks-chandler-andersen fluid", J. Chem. Phys. **124** (2006).

[129]Y. Tang, "Role of the Barker–Henderson diameter in thermodynamics", J. Chem. Phys. **116**, 6694–6700 (2002).

[130]M. Sanoria et al., "Influence of interaction softness on phase separation of active particles", Phys. Rev. E **103**, 052605 (2021).

[131]J. Martín-Roca et al., "Dynamical anomalies and structural features of active Brownian particles characterized by two repulsive length scales", J. Chem. Phys. **156**, 164502 (2022).

[132]J. W. Essam, "Percolation theory", Rep. Prog. Phys. **43**, 833 (1980).

[133]E. Brézin and J. Zinn-Justin, "Finite size effects in phase transitions", Nuclear Physics B **257**, 867–893 (1985).

[134]D. Frenkel and B. Smit, *Understanding molecular simulation: from algorithms to applications*, Vol. 1 (Elsevier, 2001).

[135]A. A. Chialvo and P. G. Debenedetti, "On the use of the verlet neighbor list in molecular dynamics", Comput. Phys. Commun. **60**, 215–224 (1990).

[136]P. Gonnet, "Pairwise verlet lists: combining cell lists and verlet lists to improve memory locality and parallelism", J. Comput. Chem. **33**, 76–81 (2012).

[137]W. Mattson and B. M. Rice, "Near-neighbor calculations using a modified cell-linked list method", Comput. Phys. Commun. **119**, 135–148 (1999).

[138]Boost, *Boost C++ Libraries*, `http://www.boost.org/`, Last accessed 2019, 2019.

[139]J. S. Centre, Journal of large-scale research facilities **7**, A182 (2018).

[140]CMake, *CMake Libraries*, `https://cmake.org/`, Last accessed 2019, 2019.

[141]OpenMP, *OpenMP Libraries*, `https://www.openmp.org/`, Last accessed 2019, 2019.

[142]G. Van Rossum and F. L. Drake Jr, *Python reference manual* (Centrum voor Wiskunde en Informatica Amsterdam, 1995).

[143]A. Stukowski, "Visualization and analysis of atomistic simulation data with ovito–the open visualization tool", Model. Simul. Mater. Sci. Eng. **18**, 015012 (2009).

[144]C. R. Harris et al., "Array programming with NumPy", Nature **585**, 357–362 (2020).

[145]J. D. Hunter, "Matplotlib: a 2d graphics environment", Computing In Science & Engineering **9**, 90–95 (2007).

[146]R. Bastien and P. Romanczuk, "A model of collective behavior based purely on vision", Sci. Adv. **6**, eaay0792 (2020).

[147]P. Stengele et al., "Group formation and collective motion of colloidal rods with an activity triggered by visual perception", Phys. Rev. E **106**, 014603 (2022).

[148]M. Knežević et al., "Collective motion of active particles exhibiting non-reciprocal orientational interactions", Sci. Rep. **12**, 19437 (2022).

[149]J. Palacci et al., "Living Crystals of Light-Activated Colloidal Surfers", Science **339**, 936–940 (2013).

[150]B. M. Mognetti et al., "Living Clusters and Crystals from Low-Density Suspensions of Active Colloids", Phys. Rev. Lett. **111**, 245702 (2013).

[151]P.-C. Chen et al., "Active particles with delayed attractions form quaking crystallites(a)", EPL **142**, 67003 (2023).

[152]T. H. Tan et al., "Odd dynamics of living chiral crystals", Nature **607**, 287–293 (2022).

[153]S. Weitz et al., "Self-propelled rods exhibit a phase-separated state characterized by the presence of active stresses and the ejection of polar clusters", Phys. Rev. E **92**, 012322 (2015).

[154]M. Bär et al., "Self-Propelled Rods: Insights and Perspectives for Active Matter", Annu. Rev. Condens. Matter Phys. **11**, 441–466 (2020).

[155]L. Caprini and H. Löwen, "Flocking without Alignment Interactions in Attractive Active Brownian Particles", Phys. Rev. Lett. **130**, 148202 (2023).

[156]J. Stenhammar et al., "Activity-Induced Phase Separation and Self-Assembly in Mixtures of Active and Passive Particles", Phys. Rev. Lett. **114**, 018301 (2015).

[157]A. Wysocki et al., "Propagating interfaces in mixtures of active and passive Brownian particles", New J. Phys. **18**, 123030 (2016).

[158]O. E. Shklyaev et al., "Convective Self-Sustained Motion in Mixtures of Chemically Active and Passive Particles", Langmuir **33**, 7873–7880 (2017).

[159]R. Wittkowski et al., "Nonequilibrium dynamics of mixtures of active and passive colloidal particles", New J. Phys. **19**, 105003 (2017).

[160]D. P. Singh et al., "Non-Equilibrium Assembly of Light-Activated Colloidal Mixtures", Adv. Mater. **29**, 1701328 (2017).

[161]J. Stürmer et al., "Chemotaxis in a binary mixture of active and passive particles", J. Chem. Phys. **150**, 214901 (2019).

[162]I. Petrelli et al., "Effective temperatures in inhomogeneous passive and active bidimensional Brownian particle systems", Phys. Rev. E **102**, 012609 (2020).

[163]G. Xu et al., "Morphologies and dynamics of the interfaces between active and passive phases", Soft Matter **17**, 9607–9615 (2021).

[164]B. Hrishikesh and E. Mani, "Collective behavior of passive and active circle swimming particle mixture", Soft Matter **19**, 225–232 (2022).

[165]J. Tan et al., "Cluster formation in symmetric binary SALR mixtures", J. Chem. Phys. **154**, 074504 (2021).

[166]L. P. Dadhichi et al., "Nonmutual torques and the unimportance of motility for long-range order in two-dimensional flocks", Phys. Rev. E **101**, 052601 (2020).

[167]M. A. López-Castaño et al., "Chiral flow in a binary mixture of two-dimensional active disks", Front. Phys. **10** (2022).

[168]C. Scholz et al., "Surfactants and rotelles in active chiral fluids", Sci. Adv. **7**, eabf8998 (2021).

[169]J. Mecke and M. Ripoll, "Birotor hydrodynamic microswimmers: From single to collective behaviour(a)", EPL **142**, 27001 (2023).

[170]K. L. Kreienkamp and S. H. L. Klapp, "Clustering and flocking of repulsive chiral active particles with non-reciprocal couplings", New J. Phys. **24**, 123009 (2022).

[171]Y. Hosaka et al., "Pair dynamics of active force dipoles in an odd-viscous fluid", Eur. Phys. J. E **46**, 18 (2023).

[172]H. Kitahata and Y. Koyano, "Mathematical modeling for the synchronization of two interacting active rotors", Phys. Rev. E **107**, 064607 (2023).

[173]S. N. Weber et al., "Binary Mixtures of Particles with Different Diffusivities Demix", Phys. Rev. Lett. **116**, 058301 (2016).

[174]J. Agudo-Canalejo and R. Golestanian, "Active Phase Separation in Mixtures of Chemically Interacting Particles", Phys. Rev. Lett. **123**, 018101 (2019).

[175]T. Liu et al., "Controlled propulsion of micro/nanomotors: operational mechanisms, motion manipulation and potential biomedical applications", Chem. Soc. Rev. **51**, 10083–10119 (2022).

[176]Y. Wei et al., "An Acousto-Microrobotic Interface with Vision-Feedback Control", Adv. Mater. Technol. **n/a**, 2100470 (2021).

[177]S. Yang et al., "Controlling Cell Motion and Microscale Flow with Polarized Light Fields", Phys. Rev. Lett. **126**, 058001 (2021).

[178]R. Reyes Garza et al., "Magnetic Quincke rollers with tunable single-particle dynamics and collective states", Sci. Adv. **9**, eadh2522 (2023).

[179]F. Schmidt et al., "Light-controlled assembly of active colloidal molecules", J. Chem. Phys. **150**, 094905 (2019).

[180]M. Selmke et al., "Theory for controlling individual self-propelled micro-swimmers by photon nudging I: directed transport", Phys. Chem. Chem. Phys. **20**, 10502–10520 (2018).

[181]Y. Zheng et al., "Five in One: Multi-Engine Highly Integrated Microrobot", Small Methods **n/a**, 2300390 (2023).

[182]J. K. Mills and D. Needham, "Targeted drug delivery", Expert Opinion on Therapeutic Patents **9**, 1499–1513 (1999).

[183]R. Singh and J. W. Lillard Jr, "Nanoparticle-based targeted drug delivery", Experimental and molecular pathology **86**, 215–223 (2009).

[184]A. Al Harraq et al., "A guide to design the trajectory of active particles: From fundamentals to applications", Current Opinion in Colloid & Interface Science, 101612 (2022).

[185]B. Lin et al., "Direct measurements of constrained Brownian motion of an isolated sphere between two walls", Phys. Rev. E **62**, 3909–3919 (2000).

[186]A. Costanzo et al., "Motility-sorting of self-propelled particles in microchannels", EPL **107**, 36003 (2014).

[187]P. de Castro et al., "Active mixtures in a narrow channel: motility diversity changes cluster sizes", Soft Matter **17**, 2050–2061 (2021).

[188]P. Gulati et al., "Boundaries control active channel flows", Front. Phys. **10** (2022).

[189]T. Lei et al., "Collective behavior of chiral active particles with anisotropic interactions in a confined space", Soft Matter **19**, 1312–1329 (2023).

[190]A. Murali et al., "Geometric constraints alter the emergent dynamics of an active particle", Phys. Rev. Research **4**, 013136 (2022).

[191]V. A. Shaik et al., "Confined active matter in external fields", Soft Matter **19**, 1384–1392 (2023).

[192]M. Gassner et al., "Noisy pursuit by a self-steering active particle in confinement(a)", EPL **142**, 21002 (2023).

[193]R. Matas-Navarro et al., "Hydrodynamic suppression of phase separation in active suspensions", Phys. Rev. E **90**, 032304 (2014).

[194]J. Katuri et al., "Arrested-motility states in populations of shape-anisotropic active Janus particles", Sci. Adv. **8**, eabo3604 (2022).

[195]M. Durve et al., "Learning to flock through reinforcement", Phys. Rev. E **102**, 012601 (2020).

[196]Z. Young and H. M. La, "Consensus, cooperative learning, and flocking for multiagent predator avoidance", Int. J. Adv. Robot. Syst. **17**, 1729881420960342 (2020).

[197]M. J. Falk et al., "Learning to control active matter", Phys. Rev. Res. **3**, 033291 (2021).

[198]M. Gerhard et al., "Hunting active Brownian particles: Learning optimal behavior", Phys. Rev. E **104**, 054614 (2021).

[199]F. Borra et al., "Reinforcement learning for pursuit and evasion of microswimmers at low Reynolds number", Phys. Rev. Fluids **7**, 023103 (2022).

[200]P. A. Monderkamp et al., "Active particles using reinforcement learning to navigate in complex motility landscapes", Mach. Learn.: Sci. Technol. **3**, 045024 (2022).

[201]D. Schildknecht et al., "Reinforcement learning reveals fundamental limits on the mixing of active particles", Soft Matter **18**, 617–625 (2022).

Acknowledgements

I would like to acknowledge those who supported me during my journey as a PhD student.

First I wish to acknowledge my funding programme for granting me the CONACyT-DAAD scholarship. I am grateful to Ms. Rocío Moreno Canales from CONACyT and Mr. Juan Carlos Rendón from DAAD, who always helped me with inquiries regarding reports and other administrative issues.

I would like to express my gratitude to my supervisor Dr. Marisol Ripoll, I appreciate the guidance you gave me as a student. Thank you for helping me with the design and careful study of our projects, for all the important discussions we had, as well as meticulous revisions you did of the overall thesis.

I also want to thank Prof. Dr. Johanness Berg for accepting being the first reviser of this thesis. I appreciate as well the help of other committee members, Prof. Dr. Annette Schmidt for participating as the chairperson, and Dr. Tanwi Debnath as the minutes taker.

My sincere thanks to Prof. Dr. Gerhard Gompper, director of the group Theoretical Physics of Living Matter in Jülich Forschungszentrum, we had some helpful discussions regarding the two main parts of this thesis. Also want to thank other members of the group, including students and PIs, with whom I had the joy to talk to during lunch and coffee breaks.

I also deeply appreciate the help of other students from Marisol, Carlos Medina and Dr. Joscha Mecke, with whom I discussed technical details regarding programming, data analysis, and physics. Thanks for this short discussions we had, they were essential for the completion of this work.

I am grateful to Prof. Dr. Fernando Peruani, with whom I held some helpful discussions on active matter and learned a lot from it, we worked together on a small project proposed in an online workshop, and later we met in person in a conference in Cergy.

I also want to acknowledge Dr. Natalia Hulai, who helped me proof reading the introduction of the thesis, as well as with casual discussions that sometimes broaden my perspective and brought me new ideas.

Quiero agradacer a mis padres por la infinita ayuda que me han brindado a lo largo de mi vida, todo su apoyo y amor incondicional ha sido vital para seguir trabajando y continuar mi carrera. Agradezco también a mis hermanos por la alegría que me traen siempre.

Rodrigo Saavedra, Jülich, August 2023.

Data availability

Underlying codes employed for the generation of data shown throughout the thesis are explained in Ch. 2. Specific simulation parameters considered are explained throughout the thesis. Obtained data is archived on the Jülich Data Access (JUDAC) file system in an account under principle investigation of Dr. habil. Marisol Ripoll and can be made available upon reasonable request.

Erklärung

„Hiermit versichere ich an Eides statt, dass ich die vorliegende Dissertation selbstständig und ohne die Benutzung anderer als der angegebenen Hilfsmittel und Literatur angefertigt habe. Alle Stellen, die wörtlich oder sinngemäß aus veröffentlichten und nicht veröffentlichten Werken dem Wortlaut oder dem Sinn nach entnommen wurden, sind als solche kenntlich gemacht. Ich versichere an Eides statt, dass diese Dissertation noch keiner anderen Fakultät oder Universität zur Prüfung vorgelegen hat; dass sie - abgesehen von unten angegebenen Teilpublikationen und eingebundenen Artikeln und Manuskripten - noch nicht veröffentlicht worden ist sowie, dass ich eine Veröffentlichung der Dissertation vor Abschluss der Promotion nicht ohne Genehmigung des Promotionsausschusses vornehmen werde. Die Bestimmungen dieser Ordnung sind mir bekannt. Darüber hinaus erkläre ich hiermit, dass ich die Ordnung zur Sicherung guter wissenschaftlicher Praxis und zum Umgang mit wissenschaftlichem Fehlverhalten der Universität zu Köln gelesen und sie bei der Durchführung der Dissertation zugrundeliegenden Arbeiten und der schriftlich verfassten Dissertation beachtet habe und verpflichte mich hiermit, die dort genannten Vorgaben bei allen wissenschaftlichen Tätigkeiten zu beachten und umzusetzen. Ich versichere, dass die eingereichte elektronische Fassung der eingereichten Druckfassung vollständig entspricht."

Teilpublikationen

- *Rotating aggregates induced by misaligned perception-dependent motility* (In preparation)
- *Emergence of directed swarms from a binary mixture of colloids with perception-dependent motility* (In preparation)

Jülich (defense date) (signature)

Rodrigo Saavedra

(+55)17637648729
r.saavedra@fz-juelich.de

Research Interests

Statistical physics, soft and active matter, complex systems, computational physics

Education

November 2023 **PhD in Physics**, *University of Cologne*, Cologne, Germany
Advisor: Dr. habil. Marisol Ripoll
Dissertation: Colloids with perception-dependent motility

January 2019 **MSc in Physics**, *National Autonomous University of Mexico*, Coyoacán, Mexico
Advisor: Prof. Dr. Julio Martinell
Dissertation: Monte Carlo simulations of ions transport in plasmas with magnetic island regions

June 2016 **BSc in Physics**, *University of Baja California*, Ensenada, Mexico
Advisor: Prof. Dr. Jesús Maytorena
Dissertation: Electromagnetic toroidal multipoles

Knowledge and skills

Languages

Spanish (native), English (proficient), German (basic)

Programming languages

Bash, C++, Fortran, Julia, Python

Markup languages

TeX, HTML/CSS, Markdown, reStructuredText

Software employed

Inkscape, Jupyterlab, Imagemagick, Mathematica, Ovito, Slurm, Openssh, Vim, GNU commands, LAMMPS

Software developed

- Guiding center dynamics of fast ions in plasmas code in C++
- Brownian dynamics code in C++
- Particle configurations scripts in Python
- Data analysis scripts in Python+Ovito

Teaching experience

Teaching assistant

Vector calculus, undergraduate course at *Autonomous University of Baja California* Fall 2015
Electromagnetism I, undergraduate course at *Autonomous University of Baja California* Spring 2016
Statistical mechanics I, graduate course at *National Autonomous University of Mexico* Spring 2018
Classical mechanics, undergraduate course at *National Autonomous University of Mexico* Fall 2018
Electromagnetism II, undergraduate course at *National Autonomous University of Mexico* Spring 2019
Statistical mechanics II, graduate course at *National Autonomous University of Mexico* Spring 2019
Computational soft matter physics, graduate course at *University of Cologne* Spring 2021

Distinctions and grants

Academic Exchange Grant by Autonomous University of Baja California, Mexico 2014
Graduate fellowship supported by National Council of Science and Technology, Mexico 2016-2018
Travel Grant supported by National Council of Science and Technology, Mexico 2018
MSc with honours, Physics 2019
Graduate fellowship supported by National Council of Science and Technology, Mexico 2019-2022
Fellowship extension supported by National Council of Science and Technology, Mexico 2022-2023

List of publications

[1]R. Saavedra, G. Gompper, and M. Ripoll, "Swirling due to misaligned perception-dependent motility", (Submitted) (2023).

[2]R. Saavedra and M. Ripoll, "Emergent directed swarm from a binary mixture of particles with misaligned perception-dependet motility", (In preparation) (2023).

[3]J. Martinell, L. Carbajal, and R. Saavedra, "Fast ion transport studies in toroidal plasmas with magnetic islands", 47th EPS Conference on Plasma Physics, EPS 2021, 737–740 (2021).

[4]R. Saavedra and J. Martinell, "Monte carlo simulations of ion transport in magnetic island regions", 45th EPS Conference on Plasma Physics, EPS 2018, 1308–1311 (2018).

Congress and conferences

Poster presentations

Monte Carlo simulations of ions transport in magnetic island regions
45th EPS Conference on Plasma Physics, Prague, Czech Republic 2018

Swirling due to misaligned perception-dependent motility
DPG meeting of the Condensed Matter Section, Regensburg, Germany 2022

Binary mixture of colloids with misaligned visual perception
Active Days EUTOPIA, Cergy-Paris, France 2022

Binary mixture of colloids with misaligned visual perception
Insights into the research projects of BCGS members 2023

Talks

Monte Carlo simulations of ions transport in magnetic island regions
LXI National Congress of Physics, Puebla, Mexico 2019

Swirling due to misaligned perception-dependent motility
Active Days EUTOPIA, Cergy-Paris, France 2022